Diamond Coatings on Graphite for Plasma Facing Materials

Isaela Villalpando de la Torre, MSc

Thesis Submitted for the Degree of Doctor of Philosophy
Heriot-Watt University

School of Engineering and Physical Sciences
May 2010

Abstract

Nanocrystalline and microcrystalline diamond films have been successfully deposited on graphite substrates for the first time. The morphology of the films depended on the experimental parameters used during deposition such as: gas mixture, excitation power, pressure and deposition time, along with nucleation treatments. Experiments are reported for removing non-diamond carbon material from commercial detonation nanodiamond used for seeding nucleation.

Scanning Electron Microscopy (SEM), Raman Spectroscopy and X-ray Photoelectron Spectroscopy (XPS) techniques were used to characterise the samples. Optical Emission Spectroscopy (OES) and Mass Spectroscopy were used to analyse the species formed in the gas phase during diamond growth.

We observed that the excitation power used during deposition affects mainly the diamond crystallite size. Microcrystalline films were obtained when the excitation power was 3.0 and 3.6 kW and nanodiamond films were observed when 1.5 kW was used. The use of argon is essential for growing diamond on graphite and the methane content affects the morphology, the sp^3/sp^2 content and the crystallite size of the films. When using less than 5% of methane in the gas mixture, {100} faces are predominant even after long periods of deposition. Using 5% of methane results in a film with cauliflower-like structure. Change in the morphology caused by secondary nucleation was observed after long deposition periods of time.

To study the behaviour of our prepared samples under erosion conditions, diamond films were exposed to hydrogen plasma etching and analysed in terms of film quality (sp^3/sp^2 content) and growth/etching mechanisms.

Finally, there is also included a study about the production of carbon fibres on diamond films during hydrogen plasma exposure in the presence of silicon.

To my husband Víctor and to my parents

Acknowledgements

I am heartily thankful to my supervisor, Professor John Wilson, whose encouragement, guidance and support from start to end enabled me to finish my research project. My most sincere thanks to Professor Phillip John for his supervision and his support throughout this work.

I would like to thank Professor Duncan Hand for his help at the beginning of my project.

My special thanks to Mr. Iain Drummond who trained me in the use of vacuum systems. Many thanks to Mr. Alan Barton and Mr. Paul Allan for their valuable help in the lab and with glassware.

I am grateful to Mr. Peter Heron, Mr. Mark Stewart and Mr. Neil Ross for their technical support and useful advice.

Mrs. Marian Millar for her help with the analytical equipment.

Dr. Graham Beamson, NCESS facility at Daresbury Laboratory, for his help with XPS analysis.

I owe my deepest gratitude to my family, friends and colleagues, whose support and goodwill kept me going through this research project. I would particularly like to thank Miss Helena Lind, Dr. Lucia Romero, Dr. Amalia I. Poblador, Dr. Iwona Szkoda, Dr. Patricia Leyva, Dr. Erinc Engin, and Dr. Rachel J.E. Lees.

I want to express my gratitude to: programme Alβan, the European Union Programme of High Level Scholarships for Latin America, scholarship No. E05D056416MX; Overseas Research Students Awards Scheme (ORSAS), CONACYT and Heriot-Watt University for financial support.

Contents

List of Tables

List of Figures

Conferences and Publications

“Microwave plasma and hot-filament CVD diamond coating of fusion reactor relevant materials”, I. Villalpando, S. Porro and J.I.B. Wilson, poster presentation, **Technological Plasma Workshop**, Belfast, UK, 2007

“Microwave Plasma Enhanced CVD Diamond Growth on Graphite Substrates”, I. Villalpando, P. John, S. Porro, J.I.B. Wilson, poster presentation, **Diamond**, Sitges, Spain, 2008

“Effect of plasma composition on the resulting morphology of diamond films on graphite substrates”, I. Villalpando, P. John and J.I.B. Wilson, poster presentation, **Technological Plasma Workshop**, Glasgow, UK, 2009

“Hydrogen plasma erosion of diamond films deposited on graphite”, I. Villalpando, P. John, S. Porro and J.I.B. Wilson, poster presentation, **Hasselt Diamond Workshop**, Hasselt, Belgium, 2010

“Microwave Plasma Enhanced CVD Diamond Growth on Graphite Substrates”, I. Villalpando, P. John, S. Porro, J.I.B. Wilson, *submitted to Diamond and Related Materials*

Chapter 1

Review of diamond synthesis and characterisation techniques

1.1 Introduction

The possibility of using diamond as a plasma facing material in fusion reactors such as tokamaks has resurrected interest in growing continuous diamond films on graphite. Today tungsten and carbon-based materials are the preferred candidates for the inside of the tokamak chamber, where they have to withstand the problems of erosion and tritium retention. The well-known properties of diamond, in addition to its exceptional thermal conductivity and strength, suggest that it could be compatible with hydrogen plasmas and be capable of withstanding temperatures of thousands of degrees Celsius and high particle fluxes.

Very little is known about the growth of diamond on graphite and there is still scepticism about the possibility of the process which will be demonstrated within this document to work successfully.

The thesis contains eight chapters. In the present chapter the reader will find a general literature survey about diamond and other carbon structures, synthesis methods for the production of diamond by CVD, growth mechanisms, and fundamental theory of the analytical characterisation techniques used in the research project. In Chapter 2, there is a detailed description of Heriot-Watt 6kW CVD system and the experimental parameters used during the synthesis and characterisation of the prepared diamond films. This chapter is followed by five self contained chapters describing the results about: 1) the removal of non-carbon diamond material in a commercial detonation nanodiamond which was later used to seed graphite in order to enhance nucleation density; 2) diamond films prepared using different nucleation techniques and excitation power; 3) diamond films prepared varying methane content in the plasma and deposition time: the species observed in the gas phase are correlated with the resulting morphology; 4) hydrogen plasma etching of thick diamond films and the relation of etching and growth mechanisms; 5) hydrogen treatment of diamond films in the presence of silicon for the production of carbon fibres. Finally, general conclusions of the research work are drawn and future work is proposed.

1.2 Diamond and other carbon structures

1.2.1 Diamond

The face-centered diamond cubic structure has eight corner atoms, six face-centered atoms and four other atoms that are displaced by $1/4a$, (a is the lattice constant and is equal to 3.567 Å) of the unit cell. The space group of diamond is $\mathrm{F}d3m$-O_h, and each primitive crystalographic unit cell contains two atoms. Each atom has four sp^3 hybrid atomic orbitals that are bonded in tetrahedral geometry to four other carbon atoms with a bond length of 1.54 Å [1].

Diamond grows at different rates in various crystallographic directions, as a result of different growth conditions. The most common facets in natural and synthetic diamond are (111), (100) and (110). The crystal orientation is specially important because many mechanical, physical and chemical properties depend on it, *e.g.* abrasion, wear, oxidation, thermal conductivity and cleavage energy.

1.2.2 Graphite

The six membered, trigonally bonded carbon rings which compose the graphite structure lie in a flat plane. Using sp^2 hybrid atomic orbitals, each carbon atom exhibits three in-plane sigma bonds; the remaining electron forms π bonds using a p_z atomic orbital. Each plane is staggered from the planes above and below resulting in an ABA sequence. In-plane, nearest neighbour carbon spacing is 1.42 Å while the lattice constant in the basal plane (between repeating layers) is 6.707 Å.

1.2.3 Carbon nanotubes

Carbon nanotubes are hollow cylinders of graphitic carbon. The tubes can be considered as rolled-up graphene sheets with diameters ranging from a few nanometers up to millimeter in length. There are three different forms in which a graphene sheet can be rolled into a tube, each represented by a pair of indices (n,m) called the chiral vector. The integers n and m denote the number of unit vectors along two directions in the graphene crystal lattice. If m=0, the nanotubes are rolled in a "zigzag" structure. If n=m, the nanotubes are rolled in an "armchair" structure. Otherwise, they are rolled in a "chiral" structure.

1.2.4 Diamond nanorods

Diamond nanorods are elongated crystals few nanometers in diameter (20 nm or less) and up to 1 μm long. The orientation of the diamond nanorods is usually not uniform throughout the sample. Depending on their diameter, surface morphology and surface functional species, diamond nanorods can be semiconducting or semimetallic [2].

1.2.5 Carbon nanofibres

Carbon nanofibres are cylindrical nanostructures consisting of graphite platelets arranged in specific orientations with respect to the fibre axis. The orientations can vary between fibres because the growth depends on the substrate (metal) orientation. Carbon nanofibres vary from 5 to 100 μm in length and are between 5 and 100 nm in diameter.

They are produced from catalytic decomposition of hydrocarbon gases or carbon monoxide over selected metal particles that include iron, cobalt, nickel and some of their alloys at temperatures over the range 400-1000 °C by a process called catalytic CVD.

1.3 Low pressure diamond synthesis techniques

The techniques for the synthesis of diamond by low-pressure methods have developed rapidly. The early approaches to form diamond from the vapour phase were using thermal decomposition of carbon-containing gases [3, 4].

In 1982 Matsumoto et al. developed the hot filament technique [5] and later in 1985 the low pressure RF glow discharge [6]. The first microwave plasma CVD technique appeared in 1983 [7] and four years later Pinneo et. al. presented their DC plasma CVD equipment [8].
Other techniques such as the oxy-acetylene torch method in 1988 [9], laser conversion of amorphous carbon in 1983 [10] and C ion implantation with laser treatment in 1991 [11] were also developed to produce diamond films.

1.3.1 Microwave plasma CVD

The apparatus that Kamo et al. [7] originally described is shown in Figure 1.1 The NIRIM-type reactor is very simple. A quartz discharge tube is inserted through the broad side of a fundamental mode rectangular waveguide, appropriate for the propagation of microwaves at 2.45 GHz.

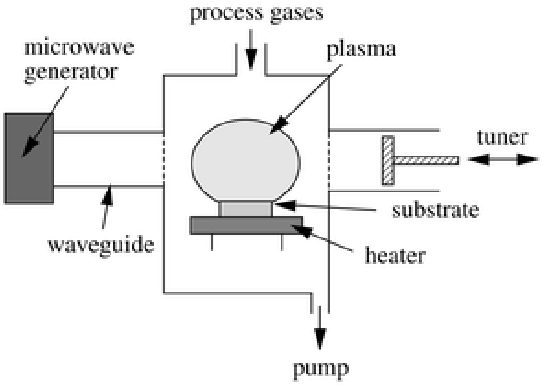

Figure 1.1: NIRIM-type reactor.

Along the propagation direction and beyond the discharge tube location, the waveguide is terminated by a short which could be adjusted to maintain the plasma location in the middle of the discharge tube. A tuning stub is placed between the microwave source and the discharge tube to ensure that all the power is absorbed in the plasma load. The substrate to be coated is introduced from the bottom of the discharge tube using a dielectric rod to prevent microwave leakage to the outside.

This design has several disadvantages such as: substrate size which is limited by the tube diameter, plasma etching of the reactor wall that can cause severe contamination of the growing film, and poor temperature control since it is determined by plasma conditions.

In the late 1980's, Bachmann and Smith [12] developed the bell jar system, a microwave reactor that would soon overcome many of the limitations of the Kamo design. In the reactor (Figure 1.2), microwaves are coupled in a water-cooled metal cavity through a dielectric window (quartz). The substrate is located on top of an inductively heated substrate stage, which allows substrate temperature control. The contamination caused by the interaction plasma-chamber walls was solved using a ball-shaped plasma that only touches the substrate surface.

Despite all other attempts, varieties of the design described by Bachmann are probably the most common in today's microwave plasma deposition units.

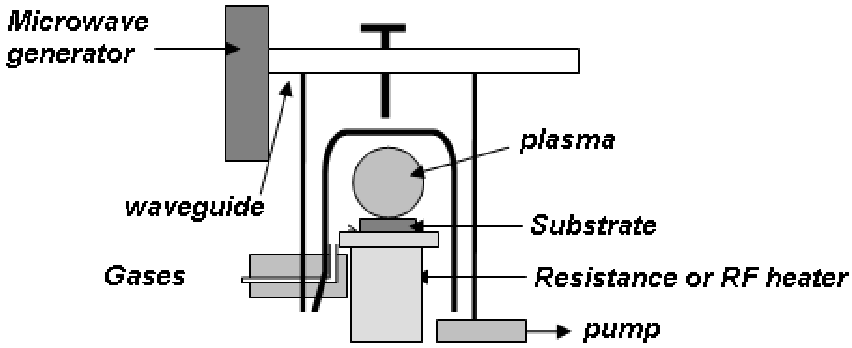

Figure 1.2: Bell Jar reactor.

1.3.2 DC Plasma CVD

In DC plasma CVD, a negative or positive DC voltage is applied to the substrate plate or to an auxiliary electrode. Intermediate electrodes may be used to guide the plasma position and alter its properties. The technique has the advantage of being able to coat large substrate areas, since deposition area depends on the electrode size. The high gas pressure and energy density used allows growth rates of 10 μm/h. The main disadvantage is that the plasma can extinguish itself if a very thick film is grown since diamond films are dielectric.

1.3.3 RF Plasma CVD

Radio frequency can be applied to create a plasma in two electrode configurations: capacitively coupled parallel plate and inductive. Plasmas can be separated into glow discharge and thermal plasmas depending on the total pressure used. Thermal RF plasmas are always inductive while glow discharge are both capacitive and inductive. Typically, RF plasma CVD employs a frequency of 13.56 MHz in very similar process conditions to the ones used in microwave plasmas. An advantage of RF plasmas is that they can be easily generated over much larger areas than microwave plasmas. The disadvantage is that the frequency of the plasma is optimal for the sputtering of dielectrics and easily produces diamond-like coatings. However various researchers have demonstrated the production of diamond films by this technique [13–15].

1.3.4 Hot Filament CVD

Hot filament CVD diamond deposition is a thermal decomposition technique where the reactants are dissociated by a refractory metal wire (tungsten, tantalum, rhenium) and heated to a temperature of around 2000 °C. The elementary principle was explained by Matsumoto et al. [5] and is shown in Figure 1.3.

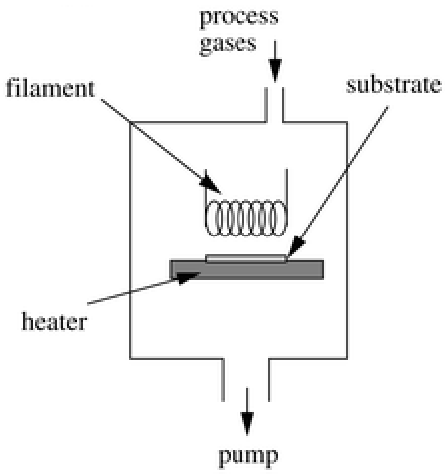

Figure 1.3: Hot filament CVD reactor.

The filament mounted near the substrate is heated by passing an electrical current through the filament. The temperature in the deposition chamber is measured by a thermocouple in contact with the substrate holder. The gas mixture diffuses onto the filament and the products form a deposit on a substrate placed below the filament at a distance of ∼2-8 mm from it. The entire process is carried out at low pressures (20-40 torr), and the deposition rate for high-quality diamond films is typically 1 μm/hr.

As with other techniques, hot-filament CVD has its disadvantages. For example the life of the precursors is occasionally not long enough to reach the substrate and produce a deposit since the material transport that takes place is via an intrinsically slow diffusion process.

Another disadvantage, and maybe the most important, is film contamination by the filament material. In fact, the concentration of metallic impurities in the film increases exponentially with increasing wire temperature. However, in the prevalent carbonaceous environment, the filament material becomes carbided and carbides have a lower vapour pressure compared to the pure metal. Consequently, it is possible to heat it to much higher temperatures without introducing any appreciable impurity into the film.

1.4 Chemical mechanisms of CVD diamond

In the CVD process the reactants, methane and hydrogen for example, enter a highly energetic region in which the gas is activated by a plasma or a hot filament (Figure 1.4). The species participating in these reactions are transported by forced flow, diffusion and convection throughout the reactor, eventually reaching the substrate. Near the substrate, species may diffuse through a stagnant flow region, called the boundary layer. On the substrate surface, various processes may occur such as adsorption, desorption, chemical reactions and surface/bulk diffusion of species [16].

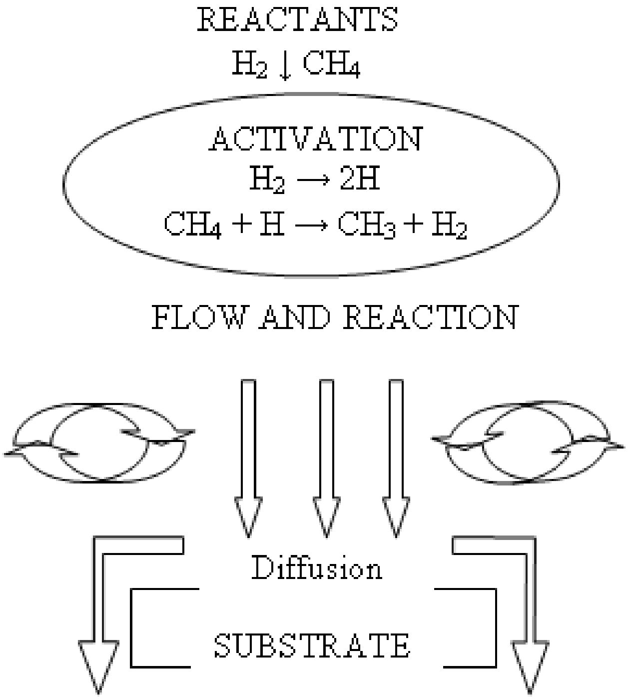

Figure 1.4: General chemical process for CVD diamond.

The growth of diamond from the vapour phase begins with nucleation, that is the initial formation of a crystal. It is followed by homoepitaxial growth, where deposition of additional carbon on the surface takes place in order to increase the bulk dimensions.

1.5 Nucleation

Many researchers agree that nucleation is a fundamental step to obtain the grain size [17], orientation [18], transparency [19, 20] and adhesion [21] desired for a specific application.

Diamond nucleation occurs as a result of the competition from nondiamond phases and the high surface energy of diamond. It has been observed that diamond nucleation occurs in various ways: 1) nucleus formation on an appropriate surface features on carbon-saturated surfaces; 2) gas phase nucleation; 3) growth on diamond fragments or other sp^3 carbon residue deposited by scratching, or 4) growth on diamond or other seeds deposited by alternative methods, for example, evaporation, sputtering or deposition in a reactor using a carbon-rich feed gas mixture.

Furthermore, there are many parameters that can influence the nucleation at the initial stages of growth: substrate material and temperature, filament temperature or plasma power, feed gas composition (carbon and atomic hydrogen supersaturations), flow rate and substrate pre-treatment prior to growth.

1.5.1 Nucleation on Unscratched Substrates

Nucleation on many non-diamond substrates occurs at steps, ledges, screw dislocations and other defects where the surface energy is high and unsaturated bonds are present [22]. Defects have been produced by: acids and lithography etching [23, 24], ion implantation [25, 26], wear tracks produced by a diamond or sapphire stylus [27], and substrate damage by bending [24].

Various degrees of diamond nucleation enhancement have been achieved by depositing interfacial layers of BN, SiC, a-C:H, diamond-like carbon (DLC), or amorphous sp^3 bonded carbon onto substrates prior to diamond growth [28–31].

It has been seen that biased hot-filament and microwave plasma electron-assisted CVD have produced denser nucleation and faster growth than conventional reactors [32], depending on the size and magnitude of the bias.

Matsumoto [33] suggested that molecules with similar structure to diamond, such as sp^3 bonded hydrocarbon cage compounds, could work as nuclei for diamond growth. These molecules possess 6-membered carbon rings and can produce single crystal diamond or twinned crystals.

1.5.2 Scratching and Seeding

To enhance nucleation in diamond deposition, most substrates are usually scratched or seeded with diamond powder, SiC or cubic boron nitride (c-BN) [34].

Scratching the substrate transfers some diamond fragments, and may produce residues of sp^3 bonded carbon material from a substrate-diamond grit reaction. Alternatively, scratching produces substrate damage that creates chemically reactive sites such as ledges, pits and mosaic faces.

Heavy scratching of the substrate surface with diamond grit enhances the nucleation density by up to roughly seven orders of magnitude. The nucleation density is proportional to the scratching time that can vary from a few minutes to hours; for short scratching times the results are large isolated crystals; by increasing the scratching time more and smaller crystals are produced.

The grit size of the diamond used for scratching also influences the nucleation density: for hand scratching the most effective grit size is 1/4 μm, and the best for scratching in an ultrasonic bath is 40-50 μm grit in suspension [35]. The larger size needed for effective ultrasonic treatment compared to manual scratching may be due to the need for more massive crystals to efficiently induce scratching damage or transfer fragments to the substrate.

Seeding the substrate can also be achieved by sprinkling the substrate with dry powder, dipping, spraying, spin-coating, electrostatic development and by electrophoresis. These methods have been proved effective by several research groups [36, 37].

1.6 Diamond Growth

Chemical vapour deposition involves a gas phase chemical reaction occurring above a solid substrate, which causes deposition onto the surface. In the case of diamond growth there are many species which play important roles in the gaseous and surface chemistry.

1.6.1 Atomic hydrogen

Atomic hydrogen is the most critical determinant of diamond film quality and the growth rate. It is involved in the formation of carbon-containing radical species and the production of H-C bonds on the growing diamond surface, preventing it from reconstructing to a graphite-like structure. Atomic hydrogen also etches the film surface, taking away both diamond and graphite. Under typical CVD conditions, the rate of diamond growth exceeds its etch rate which does not happen for other carbon structures, and only diamond film remains.

In hot-filament systems, atomic hydrogen is produced heterogeneously by thermal decomposition of H_2 on the filament surface. In plasma-enhanced systems such as microwave, RF or DC arc jet reactors, H is produced homogeneously in the plasma by collisions with free electrons or heavy particles (M) as is shown in the following reactions:

$$H_2 + e^- \Longrightarrow H + H + e^- \tag{1.1}$$

$$H_2 + M \Longleftrightarrow H + H + M \tag{1.2}$$

Hydrogen atom loss mechanisms in the reactor are pressure dependent. At low pressures (20 Torr) homogeneous recombination of H is a relatively slow proccess, and the

H loss mechanism ocurrs primarly by collisions with reactor walls and on the diamond surface.

The basic role of hydrogen is for the stabilisation of the surface, for the creation of new surface sites and for the insertion of adsorbed hydrocarbon species into the diamond lattice. Also to form reactive hydrocarbon radicals such as CH_3. These roles are widely accepted and general trends in deposition behavior can be explained satisfactorily using them.

1.6.2 Hydrocarbon chemistry

Usually carbon is introduced into the reactor as methane (CH_4) or acetylene (C_2H_2), however both are found at the substrate regardless of the initial reactant [38]. The reaction for acetylene formation at low pressures (20 Torr) and using a mixture of 0.5% CH_4 in H_2 is the following:

$$2CH_4 \iff C_2H_2 + 3H_2 \tag{1.3}$$

The reaction is endothermic (406 kJ/mol), but the change in standard-state entropy $\triangle S^0$ is positive (272 J/mol/K), due to the translational entropy of the 3 H_2 molecules produced. Since the equilibrium state is the one which minimizes the Gibbs free energy (G = H - TS), at low temperature this reaction proceeds to the left to minimize the enthalpy H, while at high temperature maximizing the entropy is more important and it proceeds to the right. Thus, for the above experimental conditions the dominant hydrocarbon is methane below about 1500 K, while above this temperature it is acetylene. Typical reactors contain both high and low temperature regions; in most cases these regions are only millimetres apart and rapid diffusion results in a mixed gas composition containing both methane and acetylene.

Methane and acetylene account for the majority of the gas-phase carbon but other species such as the methyl radical (CH_3), ethylene (C_2H_4), C_2 and atomic carbon (C) are present at much lower levels.

At highly activated environments (high H/H_2 ratio) and high temperatures (above 1000 K) the most abundant species is atomic carbon by the following reaction with m=1 [39]:

$$CH_m + H \iff CH_{m-1} + H_2 \tag{1.4}$$

where m=1, 2, 3 or 4. At low activated environments and below 1000 K, the predominant species is CH_3.

Species with three or more carbon atoms are generally believed to be unimportant.

1.6.3 Effects of oxygen addition

Several studies have reported enhanced growth rates or quality due to the addition of oxygen, or oxygen-containing compounds [40, 41]. The primary effect of oxygen is to oxidize some or all of the hydrocarbon to form CO, and increase the H level as is shown in the next reaction:

$$C_2H_2 + O_2 \iff 2CO + H_2 \tag{1.5}$$

The reactants will oxidize to CO as well as non-diamond carbon structures in the surface, improving the film quality.

1.6.4 Effects of noble gas addition

With the addition of argon it is possible to increase the electron density of the plasma and to modify the diamond film morphology. Shih et al. [42] were the first to observe that by diluting the gas precursors H_2 and CH_4 in noble gases Ar or He during CVD diamond growth, the formation of larger crystals can be inhibited, giving rise to nanocrystalline films without degradation of the film quality. This effect has been observed by Zhou et al. and Makris et al. [44, 71]. More recently however, Tzeng and Liu have demonstrated that by argon addition it is possible to produce not only nanocrystalline diamond but also microcrystalline diamond [45].

1.6.5 Growth mechanisms

The first publication about the diamond growth mechanism [46] indicated CH_3^+ as the diamond growing species; however this mechanism is incompatible with HF-CVD since the CH_3^+ concentration is insufficient and the substrate surface is uncharged under HF-CVD conditions.

Later, Chu et al. [47] proposed that the methyl radical is the dominant growth precursor under HF-CVD conditions for all (111), (100), and (110) facets but at high temperatures, CH_4 and C_2H_2 decompose into various products and it is not possible to distinguish the original source.

A growth mechanism involving only neutral CH_3 was proposed by Harris [48] for the diamond (100) surface. The mechanism suggests the addition of one methyl group to the central opposing-hydrogen site in the molecule of bicyclo-nonane (A); this addition will result in the creation of the adamantane molecule (B) (see Figure 1.5).

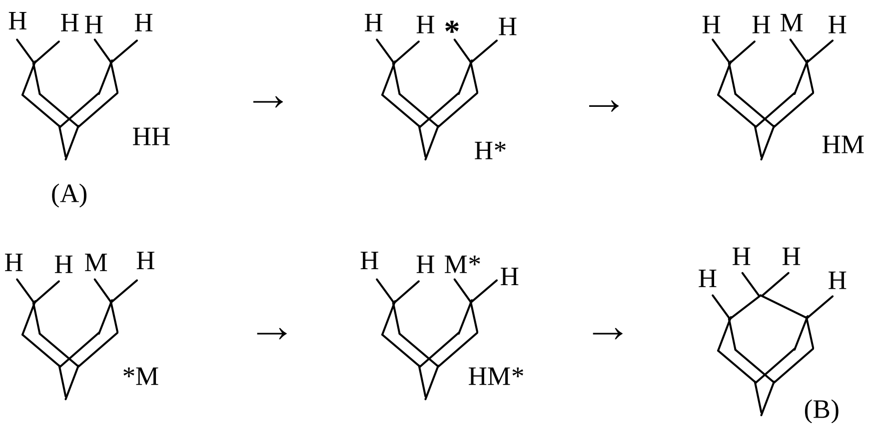

Figure 1.5: Model clusters from the mechanism proposed by Harris. The upper-left cluster is bicyclononane (A), and the lower right is adamantane (B). The asterisk denotes a radical site, M* represents a surface bonded $-CH_2$ radical and M represents a methyl group.

Frenklach et al. [49] proposed that acetylene, which is present in greater quantities than CH_3 under typical HF-CVD conditions, is the primary growth precursor on diamond (111) and other low index surfaces.

Some reports [50, 51], suggest that the C_2 dimer is involved in the growth of nanocrystalline diamond and not CH_3 or C_2H_2, but recent experimental results [52] in our research group concluded that nanocrystalline diamond is formed independently of the presence of C_2.

Diamond growth reaction kinetics involve the density of non-hydrogenated diamond surface sites C_d^*, and is controlled by two reactions which are driven by atomic hydrogen [53, 54]:

$$C_dH + H \longrightarrow C_d^* + H_2 \tag{1.6}$$

$$C_d^* + H \longrightarrow C_dH \tag{1.7}$$

In thermodynamic equilibrium of equations (1.6) and (1.7) the density C_d^* is independent of the hydrogen concentration and only a function of the substrate temperature. In the presence of hydrocarbon molecules in the gas phase the following reactions describe the growth of diamond:

$$C_d^* + C_XH_Y \longleftrightarrow C_dA \tag{1.8}$$

$$C_dA + nH \longrightarrow C_d^* + products \tag{1.9}$$

$$C_dA + H \longrightarrow C_dH + H_2 \tag{1.10}$$

Equation (1.8) describes the adsorption and thermal desorption of hydrocarbon molecules. The surface adsorbate C_dA can be etched and removed again (equation 1.9) or it can be incorporated into the diamond lattice (equation 1.10). Both processes require the assistance of atomic hydrogen.

Finally, defect formation, *i.e.* incorporation of sp^2 bonded structures, competes with the growth of sp^3 diamond. For this case Spear and Frenklach [55] specified the following reaction:

$$HC_d - C_d^* \longleftrightarrow C_{gr} = C_{gr} + H \tag{1.11}$$

where C_{gr} denotes a sp^2-hybridized carbon site.

Hydrogen desorbs and neighbouring surface radicals reconstruct to form graphitic structures. In the reverse direction hydrogen removes the double bonds.

The initial hydrocarbon concentration plays an important role in the kinetics of diamond growth, being responsible for two different growth regimes. One is a precursor where growth is limited at low $[CH_{4,feed}]$ concentration and the other is a regime where growth is limited by the number of available surface sites at high $[CH_{4,feed}]$ concentration.

In the precursor limited regime the growth law shows unambiguous $[CH_{4,feed}]^{1/2}$ behaviour. The proposed equation for diamond growth including the saturation due to the limited number of surface sites is [56]:

$$\nu_{gr} = A[CH_{4,feed}]^{1/2}[H]/[B[CH_{4,feed}]^{1/2} + D[H]] \tag{1.12}$$

with A, B, and D being numerical constants and ν_{gr} is the growth rate. At higher temperatures (1200 °C) and low pressures the significantly higher density of surface radical sites C_d^* favours the formation of sp^2 bonded structures. At high pressure and temperature diamond growth is facilitated.

The high partial pressure of atomic hydrogen is furthermore responsible for the etching at low methane concentrations. The observed shift in the growth rate curve suggests that etching is a process parallel to and independent of the growth. It can be described by an additional reaction:

$$C_dH_X + H \longrightarrow CH_{x+1(gas)} \tag{1.13}$$

The etching rate is a function of the hydrogen partial pressure and proportional to the density of hydrogenated surface sites which is roughly identical to the total density of surface sites.

The modeling calculations of May et al. [57] showed that even in hydrogen-poor $CH_4/H_2/Ar$ (1:2:97) plasmas, there are still more abundant $\mathrm{CH_3}$ and $\mathrm{CH_2}$ radicals than $\mathrm{C_2}$. And so they insisted that $\mathrm{CH_{x(x=0-3)}}$ radicals still play major roles in nanocrystalline diamond growth just as in microcrystalline diamond growth [57, 58].

1.6.6 Growth mechanism of diamond (111)

After carrying out in-situ HREELS (High Resolution Electron Energy Loss Spectroscopy) measurements [59], a two-stage mechanism has been proposed for diamond formation on the (111) surface. In the first stage, the activation of a surface carbon by H abstraction, adsorption and catenation of $\mathrm{CH_3}$ at the active site results in kernel formation. In the second stage, the (111) surface grows along the (011) direction with acetylene only, as had been suggested by Frenklach[49].

1.6.7 Growth mechanism on (100) surface

On (100) surfaces only one carbon is required to form two bonds to the surface. The (100) faces of CVD diamond often appear atomically smooth and have low defect density.

Garrison, Dawnkaski, Srivastava and Brenneret [60] ("GDSB") proposed a low-barrier mechanism as shown in Figure 1.6. The dimer is opened by abstraction of one surface hydrogen, then addition of $\mathrm{CH_3}$, abstraction of one methyl hydrogen, followed by a β-scission reaction leading to a methylidene intermediate and a radical site. This intermediate then reacts rapidly with the adjacent radical, creating a bridging methylene group and propagating the radical site.

More recently, Dawnkaski et al. [61] suggested that hydrogen-free dimer sites (which are predicted to form highly strained, reactive π-bonds) may also be an important site type where $\mathrm{CH_3}$ may chemisorb. In this case, an H migration would lead to the fourth structure in Figure 1.6.

The GDSB mechanism is now believed to be a principal means for opening and inserting carbon into dimer bonds, and has been incorporated as a submechanism into more extensive mechanisms.

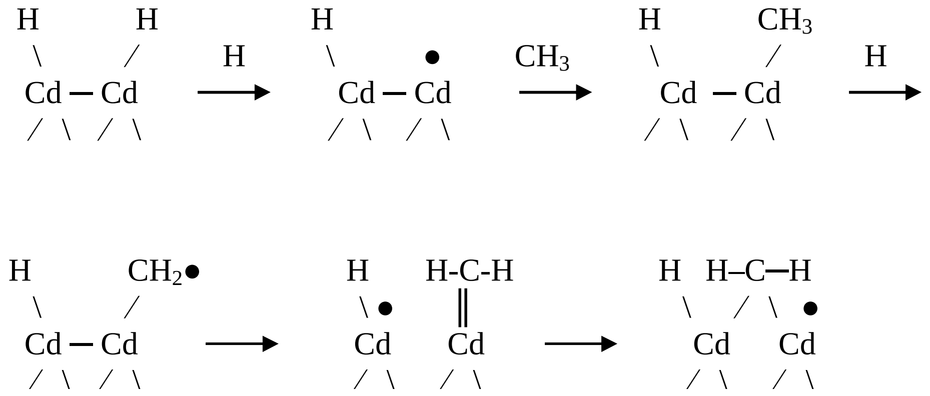

Figure 1.6: The GDSB mechanism for dimer opening and carbon insertion, Cd indicates a carbon dimer.

1.6.8 Growth mechanism on (110) surface

On the flat (110) surface two carbons must be added to form a stable structure. For this reason, like (111), it has received less attention theoretically than the (100) surface for methyl addition.

1.7 Graphitisation of Diamond

Diamond is normally kinetically stable against graphitisation, but under certain conditions diamond films and diamond clusters can spontaneously delaminate into graphite or concentric fullerenes, respectively.

Graphitisation is a surface phenomenon; it has been studied in ultra high vacuum observing that reaction begins at 1500 °C. The activation energy is 730 ± 50 kJmol^{-1} for (110) surfaces: this corresponds closely to the energy required to break two C-C bonds. The activation energy is 1060 ± 80 kJmol^{-1} for (111) surfaces, corresponding to the energy required to break three C-C bonds. It has been suggested that the process is autocatalytic, since graphitisation starts at discrete nuclei and spreads progressively across the surface [62].

The graphitisation process can be catalysed by oxygen and by iron, cobalt, cerium and nickel [63, 64]. There are other factors that can induce graphitisation such as ion-beam bombardment [65], high concentration of doping atoms [66], surface sputtering [67], and high pressure [68].

1.8 Nanodiamond and ultrananocrystalline diamond

Ultrananocrystalline diamond (UNCD) thin films are made of diamond crystallites with diameters less than 10 nm and have little or no graphitic impurities at grain boundaries. The physical properties of UNCD resemble those of diamond and diamond-like carbon (DLC) due to sp^3 bonds. The surface morphology is extremely smooth, which is similar to that of DLC but in contrast to that of polycrystalline diamond, they are thermally stable up to at least 600 °C.

UNCD films have great potential for use in electronics, MEMS or as biochemical sensors, since they combine many of the superb properties of diamond with a smoothness on the nm scale.

Nanodiamond films have diamond particle size considerably less than one micron. They have high grain boundary density, high sp^2 carbon content and a smooth surface morphology for material integration. Nanodiamond films are grown with a very high initial nucleation density and its grain size and hence roughness increase with film thickness. There is little or no re-nucleation and above a thickness of around 1 μm, the film becomes microcrystalline depending experimental parameters and initial nucleation density.

1.9 Characterisation techniques

There are many characterisation techniques to analyse *in-situ* diamond growth and the resulting films but in this chapter only the techniques that are relevant to this research project are considered. A short description of the techniques, basic principles and a literature review about diamond films analysed using these techniques follows.

1.9.1 Optical Emission Spectroscopy

Optical emission spectroscopy (OES) is a non-invasive probe to investigate atoms, ions and molecules decaying radiatively within a plasma. It can provide infomation about properties, such as (excited state) species densities, electron-atom, atom-atom and ion-atom collisional effects, energy distribution of species, etc.

Studies of OES in diamond deposition have been key in the understanding of the growing mechanism. Radiative species such as C_2, CH_x, C_3, H and H_2 have been widely detected in the plasma and related to the growing rate, preferred orientation and diamond quality of the resulting films.

The common bands in OE spectra from methane plasmas excited at 25 kHz are: CH(431.4 nm), H(486.1 nm) and H_2 (463.4 nm). They result from dissociative excitation of the CH_4 molecule under electron impact. At 13.56 MHz the H_β emission appears to result from both dissociative excitation from CH_4 and electron impact excitation of H atoms present in the bulk of the discharge [69].

An extra band that appears in mixtures of CH_4/H_2 and $CH_4/H_2/Ar$ at 2.46 GHz is the C_2 Swan band between 340-785 nm. The C_2 Swan band corresponds to the transition d $^3\Pi_g \longleftrightarrow$ a $^3\Pi_u$ and the intensity of this band has been directly related to the absolute C_2 concentration in plasmas [70].

The C_2 species is very important in diamond growth. It has been proposed as the growth species during deposition of nanocystalline diamond [43, 71, 72]. However later reports indicate that C_2 is not necessarily the key growth species [52, 73]. The C_2 species have also been correlated with the bad quality of the diamond films. Balestrino et. al. [74] found a correlation between the quality of the obtained diamond films and the presence of the CH species, in the absence of the C_2 emission band. Another report showed that maxima in the ratios of the CH:C_2, CH:C_3 and H:C_2 emission intensities are all found to correlate with process conditions for good quality diamond [75].

The crystal orientation can also be influenced by modifying the radical's concentration. Zhou et al. [76] have prepared diamond films with (111) dominant crystalline surfaces when increasing the intensity ratio of CH/H_β and decreasing the intensity ratio of C_2/H_β.

Balestrino et al. [74] found a correlation between optimum diamond growth rate (and quality) and the ratio of the emission intensities from CH(431 nm) and C_2 (505-517 nm), and suggested this is a practical way to optimise growth conditions for unfamiliar gas mixtures. Later, Mollart and Lewis [77] found that the ratio of the H_α (656 nm) and C_2 emission peaks intensities varied with gas composition, but this ratio had only a weak correlation with the diamond deposition orientation.

The production of soot causes a rising background in the OES spectra at longer wavelengths (>500 nm). This background was attributed to black body emission from soot particles in thermal equilibrium with the gases in the plasma region [78].

1.9.2 Mass Spectroscopy

Mass spectroscopy is a complementary technique to OES, it is used to make *in situ* analysis of the gas phase composition during CVD deposition. It has high sensitivity for stable and highly reactive species (such as radicals) from the plasma region. However, the technique is intrusive and the collected sample may change inside the sampling tube preventing the intended species from being detected.

Mass spectroscopy has been very useful in understanding the diamond growth mechanism and the species involved in the process. A mass spectrum of $CH_4/H_2/Ar$

microwave generated plasma will present species such as H (m/e = 1), CH (m/e = 13), CH_4(m/e = 16), C_2H_2(m/e = 26), C_2H_4 (m/e=28) and Ar (m/e=40). The peaks around m/e=50 will correspond to 4-carbon species such as C_4H_2 (m/e=50) and C_4H_3 (m/e=51).

It has been seen that the gas-phase composition is independent of the nature of the hydrocarbon source species if the microwave power level is above $\approx$ 700 W. Below this power level, the measured composition was dependent on the nature of the hydrocarbon source used [79].

It has also been observed that with low methane concentrations and low temperatures there is a linear dependence of the C_2H_x signals on $[CH_{4,feed}]$. In contrast, the CH_3 signals scaled with $[CH_{4,feed}]^{1/2}$ which means that $[CH_3] \propto [C_2H_x]^{1/2} \propto [CH_{4,feed}]^{1/2}$. As a consequence there is a linear relationship v_{gr} vs. $[CH_3]$, suggesting CH_3 the dominant growth species [80]. If the reaction is carried out at high temperatures there is a linear scaling of the growth velocity with the acetylene concentration. This suggests that acetylene is the dominant growth species. These results are in accordance with those previously reported by Harris et al. [81]. They used MS and calculations based on a chemical kinetics model to show that the diamond growth comes mainly from reaction of acetylene (C_2H_2), ethylene (C_2H_4), methane (CH_4) or methyl radical (CH_3).

There is also a relation between the hydrogen concentration in the $CH_4/Ar/H_2$ gas mixture and the quantity of CH and CH_2 radicals detected in MS. The less hydrogen in the mixture the more CH and CH_2 species in the reaction [82].

The addition of other species to the reaction gas has been also analysed by MS. H_2S addition for example reduces the concentration of the relevant CH_x growth species [83]. When CCl_4 is added to the mixture it is completely dissociated, with the halogen atoms entirely converted into HCl and the carbon atoms divided among hydrocarbons and CO [84].

1.9.3 Infrared Spectroscopy

Infrared (IR) absorption is one of the most important non-destructive techniques for the characterisation of diamond. Formal studies of natural and synthetic diamond using IR have been carried out since 1930 [85]. Well documented reports on IR diamond spectra can be found in [86, 87].

IR spectroscopy has been used to obtain information on hydrogen content, carbon bonding environments and bulk impurities. A typical IR spectrum from diamond is presented in Figure 1.7. The absorptions in the two-phonon region between 1400 and 2666 cm^{-1} are due to pure diamond (Figure 1.8). Three intense bands at 1900–2000 cm^{-1} are the characteristic diamond footprint but there are twenty one absorptions lying in this range which were described in detail by Klein et al. [88] .

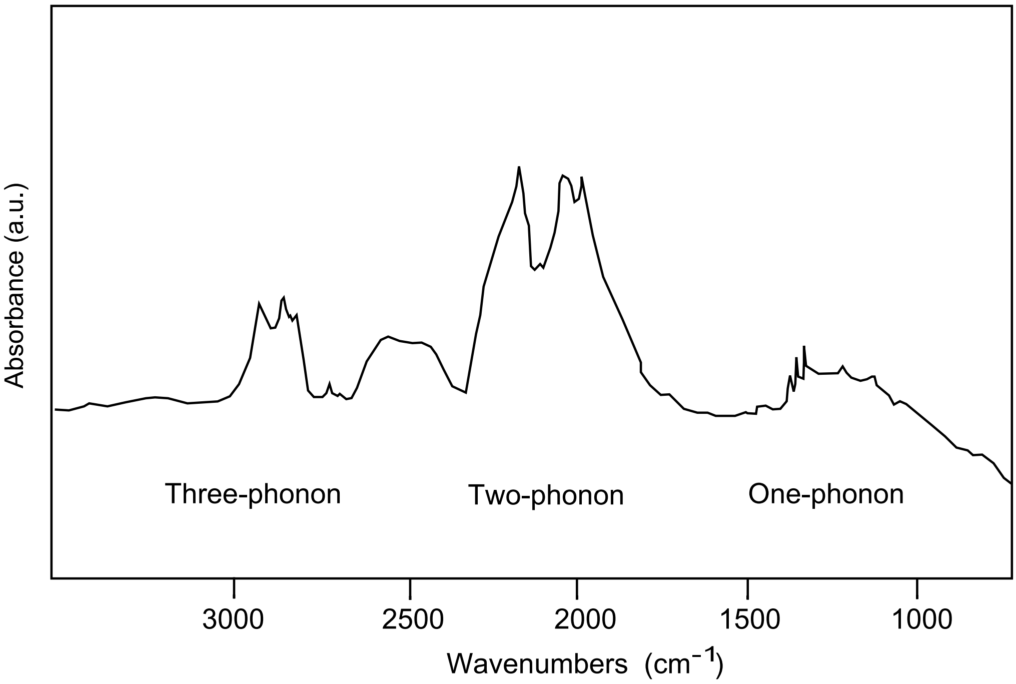

Figure 1.7: IR absorption spectrum of a typical CVD diamond sample [89].

For natural and HPHT single crystal diamond the absorption coefficient in the two-phonon region is constant and the IR absorbance is proportional to the thickness of the samples. Such a relationship between IR absorbance and sample thickness does not apply to polycrystalline or nanocrystalline CVD diamond films where the grain size is an important factor [90].

Three-phonon absorption and the CH stretch region lie at 2750-3300 cm^{-1} showing hydrogen bonded to carbon and other atoms present as impurities, such as nitrogen or oxygen. One or more hydrogen atoms bonded to a single carbon atom shift the frequency of the stretch vibration so it is possible to distinguish between sp^2-bonded carbon, which presents bands at 2850 and 2920 cm^{-1}, and sp^3-bonded carbon with absorptions at 2880 and 2960 cm^{-1}. Lines at 2820 and 2833 cm^{-1} are related to carbon-hydrogen bonds in an N-CH$_3$ and O-CH$_3$ group respectively. The CH stretch absorption is particularly prevalent in CVD diamond [87, 89, 91].

The one-phonon absorption between 1000 and 1400 cm^{-1} (8-12 μm wavelength region) shows carbon bond vibrations modified by impurities in the diamond such as nitrogen [92] and oxygen, and/or defect centres [93]. One example is the absorption at 1282 cm^{-1} which is proportional to the nitrogen concentration. The absorption bands in the one-phonon region are grouped into sets A and B, the A-centre is a defect of trigonal symmetry caused by a pair of substitutional nitrogen atoms and the

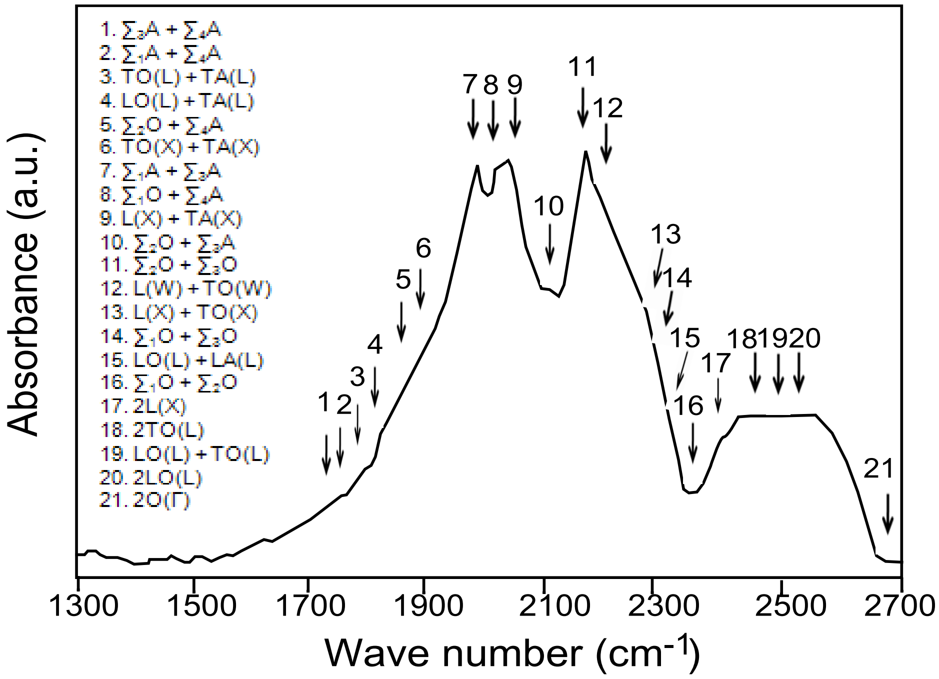

Figure 1.8: IR absorption spectrum in the two phonon region of a good quality CVD diamond [88].

B-centre is an aggregated form of nitrogen. Table 1.1 lists the absorptions observed below 1800 cm^{-1} in CVD samples [89].

Table 1.1: IR absorptions observed below 1800 cm^{-1}.

Frequency (cm^{-1})	Functional group
1740	C=O, stretch
1610	C=C, stretch, isolated
1500s	C=C, aromatic stretch
1450	O-CH_3, N-CH_3, deformation sp^3 CH_2, scissor
1375	N-CH, scissor, sp^3 CH_3, deformation
1350	substitutional N
1332	disallowed one-phonon mode
1250	C-N nitrogen-vacancy pair
1220	C-N, stretch
1130-1150	O-CH_3, N-CH_3, rock substitutional N
1030	O-CH_3, deformation

1.9.4 Raman Spectroscopy

Like IR, Raman spectroscopy has also been a useful non-destructive technique in the characterisation of diamond films. It can distinguish between different forms of carbon and it has been used as a measure of quality and purity of the films [94–96]. But it has also been used to measure the stress and temperature of the sample and to detect crystalline defects such as vacancies and split-interstitials caused by dopants in the diamond films [97].

Cubic carbon, diamond, has a single triply degenerate first order phonon with symmetry T_2g that is Raman active only. The first order band, produced using 514.5 nm argon ion laser radiation, appears as a single sharp line at 1332 cm^{-1} with typical line width of 2 cm^{-1} (see Figure 1.9).

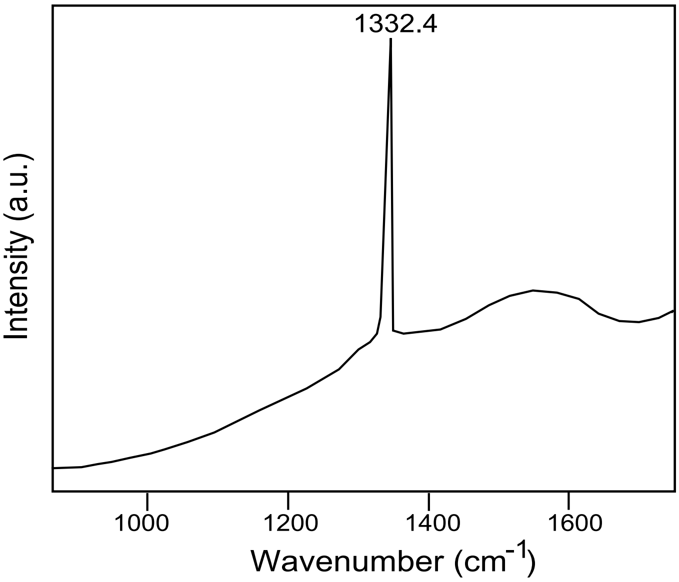

Figure 1.9: Raman Spectrum of (100) faceted diamond film on silicon [98].

Graphite, on the other hand, has a first-order E_2g optical mode at 1583 cm^{-1}, designated as the G band, and a second order G* peak at 3250 cm^{-1}. A new band is observed at 1370 cm^{-1} when Raman scattered light is collected from a sample with well-crystallized but small particles: it is named the D band and it is also assigned to a first order phonon. A second order spectrum shows the D* mode at 2710 - 2724 cm^{-1}, corresponding to an overtone of the D mode [99]. It is shown in Figure 1.10.

Other bands that are commonly present in diamond film Raman spectra are from other forms of solid carbon such as charcoal, coke, glassy carbon and diamond-like carbon that have very broad bands containing several overlapping components lying between the two graphite bands.

Many parameters can affect the position, width and intensity of Raman lines, as for example small shifts in the wavenumber (∼4-13 cm^{-1} either positive or negative) due to the stress built into deposited films that are dependent on the substrate material. Hard substrates such as alumina or carbides will give bigger shifts caused by the lattice or thermal expansion mismatch between the substrate and the diamond film. Line width has been related to the degree of structural order (or disorder in sp^3

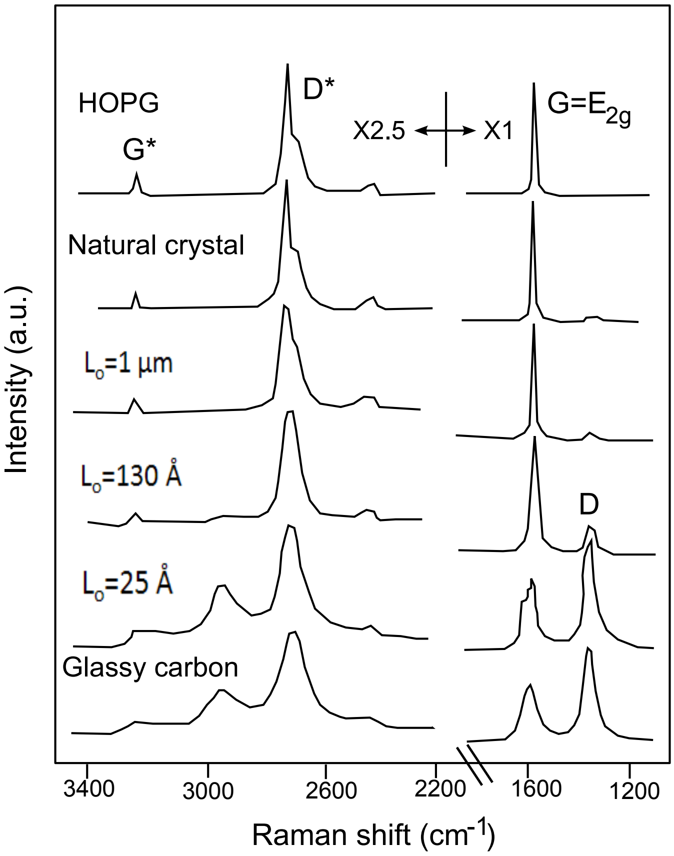

Figure 1.10: First and second order Raman spectra of several forms of graphite L_0 = domain size [100].

bonding environment) but also to the grain size and to sample temperature. The intensity of the diamond Raman line increases linearly with thickness of the diamond film. Similarly, other effects such as isotope (^{13}C) concentration, temperature [101], crystalline defects and the excitation photon energy are responsible for shifts in the position of the bands. In UV Raman this last effect is used to enhance the Raman signal.

Another important fact that must be taken into account when analysing diamond films with graphitic phases is the wavelength-dependent Raman scattering efficiency, which for sp^2 bonded carbon may be 50 times greater than sp^3 bonded carbon. This means that the technique is very good in determining small quantities of non-diamond in diamond films but for some samples the strong signal from graphitic phases may hide the weak signal from diamond.

1.9.5 X-ray Photoelectron Spectroscopy

XPS is a surface-sensitive (first atomic layers, 5-50 Å), non-destructive technique in which a sample is irradiated with low energy X-rays (usually K_α emission from aluminium or magnesium sources) which are absorbed to produce electrons ejected from the inner atomic shells. The binding energy can be determined which allows identification of the atoms and their chemical state.

XPS analysis of diamond films has been used for different purposes but especially to determine their elemental and phase purity (diamond/graphite content) and to study the interaction with species attached to the surface (e.g. hydrogen, oxygen and nitrogen). It has also been used to study the nucleation process and the interface between the substrate and the film in the early stages of deposition, thus providing information about the growth mechanism in different environments [102, 103]. Additionally, sample cleaning effects have been observed, such as surface graphitization or oxidation caused by ion bombardment or acid treatments [104].

The XPS signal is usually averaged over a large area ($\sim$20 mm^2), making nucleation difficult to study, and it is not very sensitive to minority species below about 0.5% of the surface atoms. Signals from the valence band that might distinguish local carbon bonding (sp^2 vs. sp^3) are weak [16] and carbon core levels are insensitive to minor changes in local bonding configurations. Sometimes it is necessary to coat the surface with gold because of sample charging effects, or to use a charge compensation gun.

The binding energy of diamond in an XPS spectrum is from the carbon 1s electrons and is usually found at 284.4 eV while for graphite the C1s peak is at 284.68 eV. As the binding energy of core electrons in diamond, graphite or amorphous carbon shifts less than 1 eV, it is difficult to distinguish among them if the XPS system does not have sufficient resolution. On the other hand, these carbon phases are easily identified from carbon compounds such as carbonates and carbides (Figure 1.11). This is an advantage in cases where carbon oxides (C1s $>$ 285.5 eV) are present as contaminants and/or the carbide is the first layer formed in diamond deposition, for example on silicon where SiC is present (C1s = 283.4 eV). For species such as hydrocarbons (C-H bonding), the C1s peak is very close to that of a pure carbon phase and cannot be resolved experimentally; in this case curve fitting is used to deconvolute the data.

The valence band XPS spectra (more commonly obtained with ultraviolet illumination as UPS) can reveal noticeable differences between diamond and graphite or amorphous carbon, but the photoelectron intensities are so low that accurate measurements can be difficult. McFeely et al. [106] studied the valence bands in diamond, graphite and glassy carbon and observed that all samples display the same gross structure (Figure 1.12). The main features in all spectra are: i) a broad intense peak between 16 and 21 eV; ii) a narrower, less intense peak at about 10 to 15 eV; and iii) a very broad peak extending from 10 to 13 eV to the cut-off energy.

Other characteristic bands also used to determine the sp^2/sp^3 content are the plasmon peaks adjacent to the C1s peak. The typical loss peaks are visible at ±23.5, and ±34

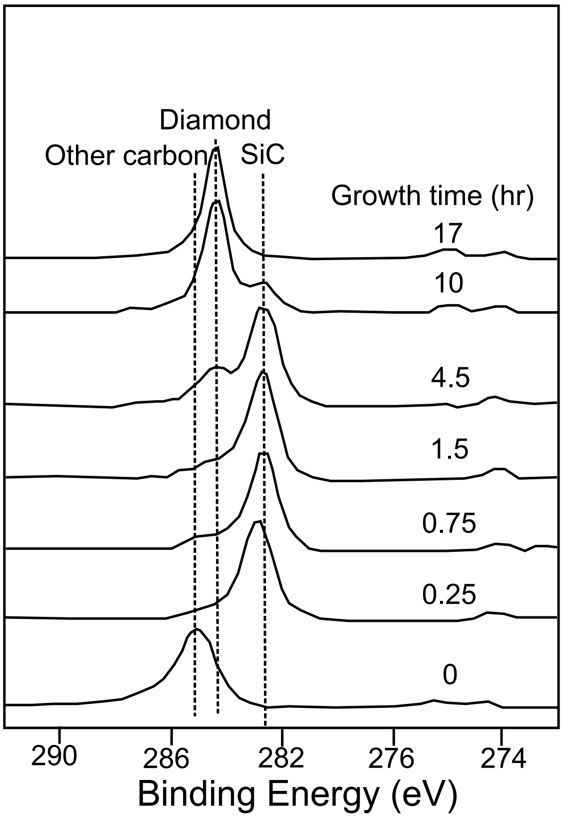

Figure 1.11: XPS spectra of the C1s region for different growth times. Spectrum at t=0 shows carbon contamination typical for Si cleaned with methanol prior deposition. Spectra (b) to (g) show the formation of a carbide layer followed by diamond growth [105].

eV from the C 1s photoelectron peak. The peak at 23.5 eV is due to surface plasmon loss. The peak around 34 eV is due to bulk plasmon and does not appear in the spectrum for graphite. An extra peak characteristic of the graphite spectrum at ±12 eV due to the collective π-electron excitation is also visible in this region.

1.9.6 Scanning Electron Microscopy

This is the most widely utilized technique to characterise the surface morphology of epitaxial and polycrystalline diamond films. It has been shown that depending on the experimental conditions, CVD diamond films can be grown with a variety of surface morphologies. For example, diamond films grown on silicon substrates by MPCVD for several hours from a mixture of CH_4/H_2[107], present square (100) faceted polycrystalline diamond (Figure 1.13a). Alternatively by adjusting the deposition conditions, the same mixture of CH_4/H_2 can produce a highly faceted polycrystalline morphology, often with triangular (111) facets as shown on Figure 1.13b. On the other hand if the experimental conditions are not adequate for these crystalline habits, the morphology becomes cauliflower-like which is commonly related to an increase of sp^2 bonds

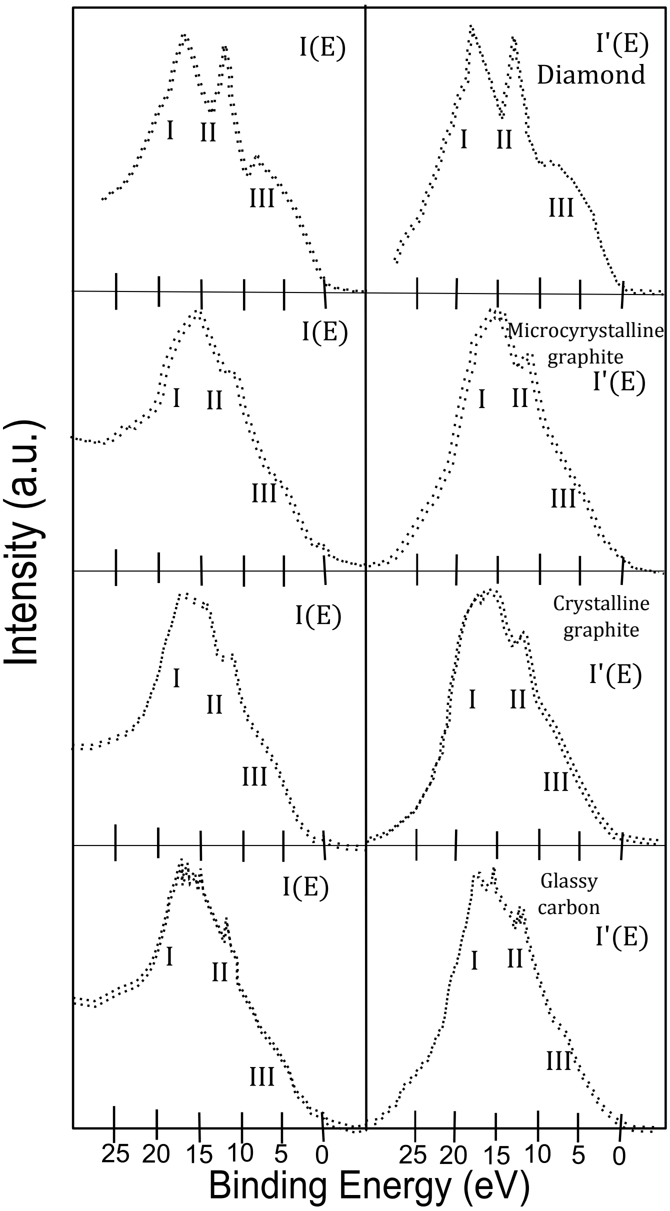

Figure 1.12: Valence-band XPS spectra, before (left) and after (right) correction for inelastic losses, of diamond, microcrystalline graphite, crystalline graphite, and glassy carbon [106].

(Figure 1.14). Early in the technology of CVD diamond, Pickrell et al. [108] used SEM to study the sectioned interfaces between microcrystalline diamond and silicon, and between diamond and silicon oxide. They showed columnar growth developing in thicker films on silicon, with the smaller crystallites growing out below the upper surface at the expense of the larger crystallites. In contrast, samples deposited on silicon oxide had an interlayer containing graphitic carbon and silicon carbide which presented poor adherence (Figures 1.15 and 1.16).

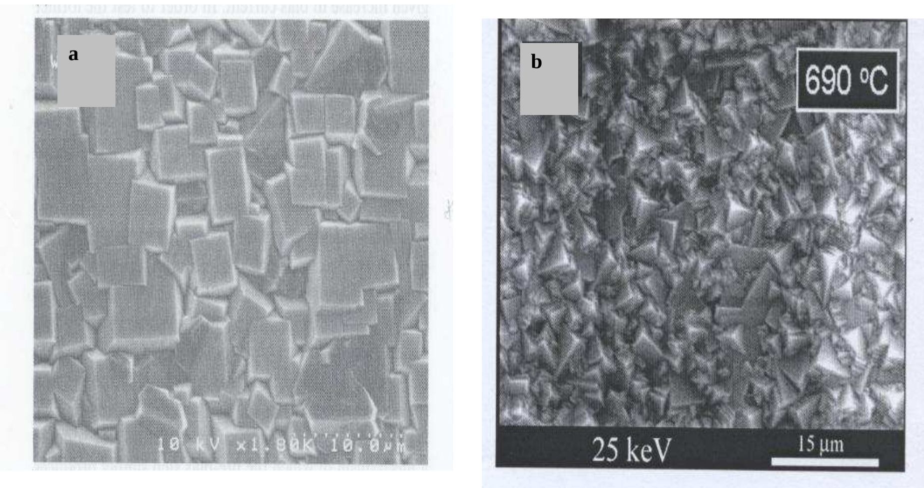

Figure 1.13: SEM micrographs (a) Back scattered electrons image from a diamond film (100)-orientated; (b) Secondary electron image from a diamond film with triangular (111) facets [107].

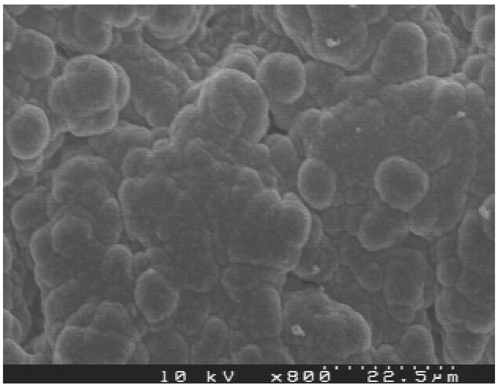

Figure 1.14: SEM micrograph showing a cauliflower-like morphology diamond film.

1.9.7 Transmission Electron Microscopy

TEM has been used extensively to characterise defects in CVD diamond, including planar defects such as twins and stacking faults (see Figure 1.17), line defects such as dislocations, and second phase inclusions that in diamond are mainly graphite. The defects can be distributed either uniformly in the grains, only at the grain boundaries, or in bands within the grains. Defects increase when methane concentration increases during the deposition and the grain size becomes smaller. Ma et al. [110] have reported that it is possible to alter the density of defects by altering the charged species during the deposition using biasing conditions. TEM has also revealed that crystalline defects can affect the final surface morphology [111]. An example is (111)-faceted films which show twinning and stacking fault features on the (111) planes.

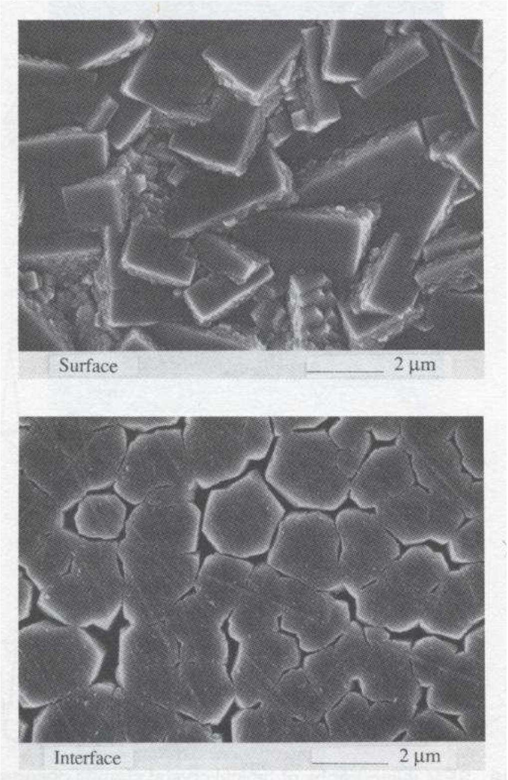

Figure 1.15: SEM micrographs of the interfaces and their corresponding surfaces for diamond films grown on a Si substrates [108].

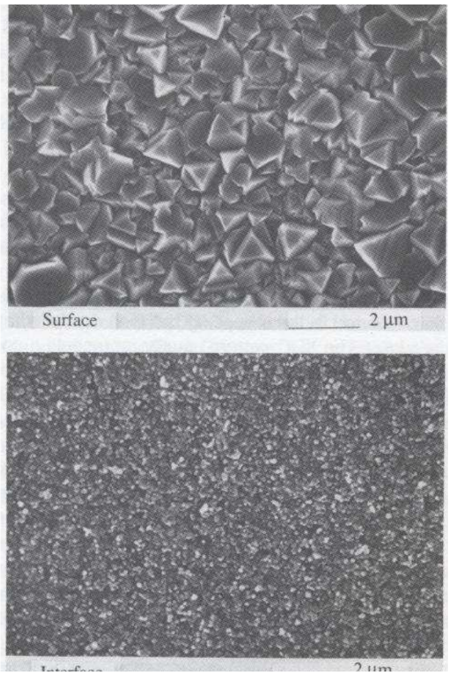

Figure 1.16: SEM micrographs of the interfaces and their corresponding surfaces for diamond films grown on a SiO_2 substrates [108].

The crystals in (100)-oriented films are planar-defect free, and films with cauliflower morphology present only small defective crystals. The growth rate is much faster on the (111) surfaces than on the (100) surfaces, possibly because defects on the (111) surfaces promote nucleation and growth [112]. Graphitic inclusions in diamond films have also been studied. For films deposited using 2% methane, graphite crystallites are formed along the (111) plane or close to it. For films deposited with an even higher methane concentration, the graphite crystallites are randomly distributed in the diamond matrix with no preferential orientation.

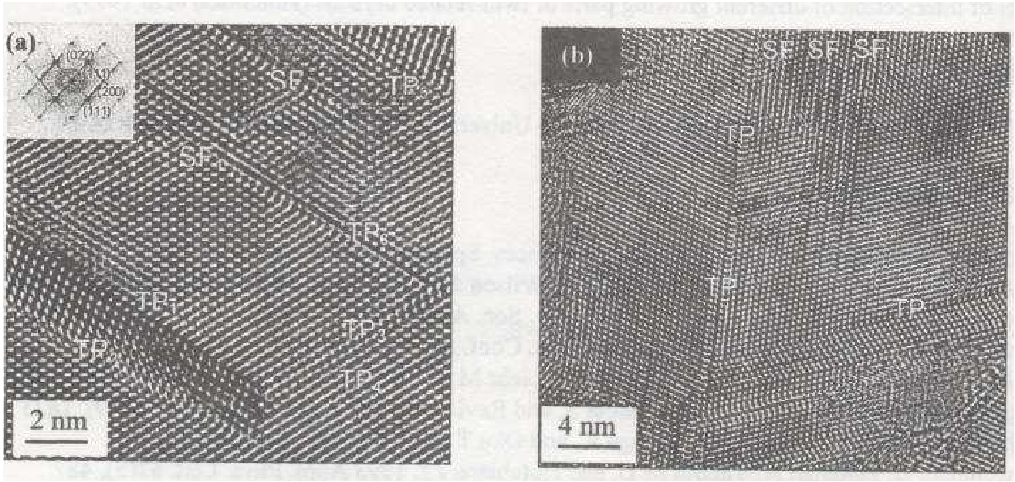

Figure 1.17: Lattice images taken from a diamond specimen with cauliflower-like growth features. (a) A lattice image showing lamellar twins, (b) a lattice image showing stacking faults [109].

In summary, great efforts have been made in the development of synthetic diamond and its characterisation techniques, however most of the synthetic diamond has been grown on silicon substrates and very little is known about the growth on other substrates, especially on graphite. In the following chapters the work done to establish experimental growth conditions of CVD diamond on graphite and its behaviour under hydrogen plasma etching will be presented.

Chapter 2

Synthesis and characterisation of diamond films

This chapter is dedicated to describing the general experimental details for diamond deposition and the parameters used in the different analytical techniques. The specific conditions for each experiment together with the results and discussion will be found in the following chapters. Here are also included the methods and software used for the analysis of the data obtained from the characterisation techniques.

2.1 6 kW Microwave Plasma Enhanced CVD System

The 6 kW microwave plasma enhanced CVD reactor in the Diamond Group is a home-built system [52] consisting of a stainless-steel chamber with four CF 250 ports on each side, one of them connected via a gate valve to a load lock chamber (see Figure 2.1).

The plasma is formed in a quartz cylinder with a microwave-shielding mesh (not shown on the figure for clarity) that is mounted on top of the main chamber. The microwave power is guided by the waveguide to a coaxial blade applicator (DILAB Ltd.). The power applicator has 20 blades distributed evenly around an aluminium plate. This design permits the creation of a plasma in the centre of the chamber which is larger than those produced for conventional MW power applicators.

The microwave power supply and magnetron (Muegge model MW-GPERE 3327-5K-02) has a frequency of 2.46 GHz, 6 kW max. The waveguide is equipped with three tuning stubs and a tuning plunger for optimal mode matching into the microwave cavity.

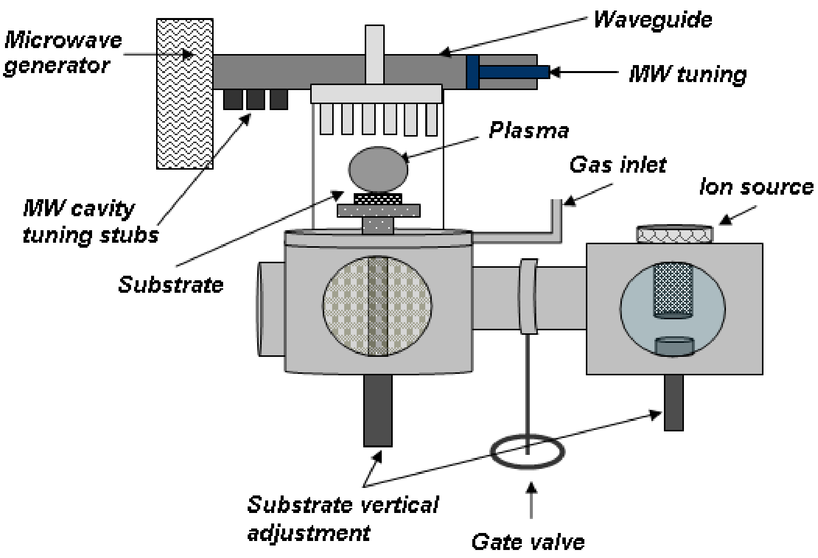

Figure 2.1: Schematic diagram of our 6 kW Microwave Plasma CVD Reactor.

The two chambers are evacuated using a two-stage E2M40 HV rotary pump and a turbomolecular pump (EXC 300 controlled EXT 501/160 CF, Edwards). The pressure is measured using Pirani (APG-M-NW16 AL, Edwards) and Barocel (600 capacitance manometer, Edwards) gauges.

The flow of the hydrogen and methane gases is controlled by Ultraflow Massflow controllers (with flow rates 0-100 sccm, Vacuum General), argon gas is controlled by a Tylan FC2901 mass flow controller (Millipore with flow rate 0-1 sclm) and the substrate temperature is measured in the reactor using a two-colour optical pyrometer.

The load lock chamber is equipped with an end-Hall ion source (3.0-1500-100 Ion Source, Ion Tech, INC), which permits either pre-deposition or post-deposition treatment of the sample.

A photograph of the equipment is shown in Figure 2.2. In the course of this research project some modifications were done to equipment in order to have a better control of the experimental parameters and improve the vacuum in the chamber. The results of these changes allowed us to grow diamond at higher microwave power without having reflection power or extra plasmas in the chamber. Here are the most important changes for future reference. In order to improve the pressure in the system a plain quartz cylinder was used instead of a multiport quartz tube and the gate valve was replaced. The most effective microwave delivery was achieved by rebuilding the waveguide short-circuit termination and installing a cooling fan in front of the three stub tuner which prevented overheating of the stubs that then caused power leakage.

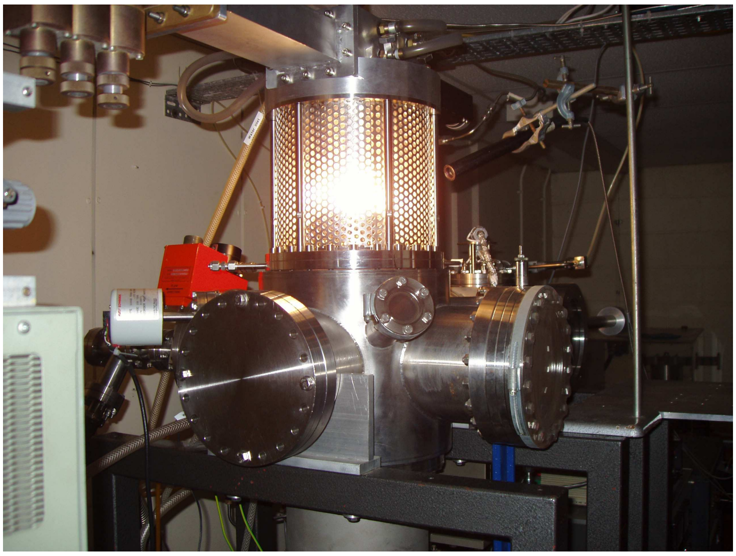

Figure 2.2: Heriot-Watt 6 kW Microwave Plasma CVD Reactor.

2.2 Experimental conditions during diamond growth

The typical experimental procedure for diamond deposition begins by introducing air to the isolated main chamber, in order to be able to open the load flange. The two chambers are usually kept under vacuum to maintain their cleanliness. The gate valve allows them to be isolated during the sample load/unload and deposition. The substrate, (graphite or silicon piece) is introduced into the main chamber, the load flange closed and the throttle valve opened slowly until the pressure is below $9\text{x}10^{-1}$ torr. The gate valve is then opened to allow the evacuation through the turbomolecular pump, at this stage the rotary pump is working as a backing pump. When the pressure is around $4\text{x}10^{-7}$ torr the chamber is ready to be filled with the reaction gas.

The throttle valve is used to maintain the pressure constant during experiments, allowing a steady flow of gases. The plasma is then struck by turning on the magnetron and adjusting the tuners to get the minimum reflection power. The correct way to do this is by unscrewing the three tuners and screwing in the closest to the magnetron until the minimum reflection power, then the same for the tuner in the middle, followed by the farthest from the magnetron. The procedure is repeated until 0% of reflection power is achieved.

When deposition is over, the methane flow is stopped and the power gradually decreased (2.5% power per minute) until completely off. When the plasma is off the hydrogen and argon flow are stopped and the chamber evacuated, first with the rotary pump and then with the turbo pump to achieve a high vacuum. Samples are allowed to cool down and then taken out from the main chamber.

The chamber cooling systems (water pipes and fans) necessary in all the experiments are left on for at least half an hour after finishing deposition in order to allow the system to cool down.

2.3 Characterisation Techniques

2.3.1 Optical Emission Spectroscopy

Optical emission measurements were taken from the plasma using a Monolite 6800 optical spectrum analyser. The light was collected using a fibre optic cable that was 10 cm from the chamber mesh and pointing at the middle of the plasma where the light intensity was higher. Scans were made from 200 to 900 nm and 1000 scans were averaged. The detector and grating responses were calibrated using a tungsten lamp that is known to be a near black-body emitter.

Calibration was done measuring the emission from the tungsten lamp and comparing it with the theoretical black body emission curve which is described by the following equation:

$$R(\lambda) = \frac{2\pi c^2 h}{\lambda^5} \cdot \frac{1}{e^{\frac{hc}{\lambda k T}} - 1} \tag{2.1}$$

where c is the speed of light (3 $\times 10^8$ ms^{-1}), h is Planck's constant (6.626 $\times 10^{-34}$ Js), T is the temperature of the black body (1568.15 K), k is Boltzmann's constant (1.38 $\times 10^{-23}$ JK^{-1}) and λ is the wavelength (200 - 900 nm).

Then the real optical emission spectrum is:

$$\text{Real spectrum} = \text{c}(\lambda) \ \cdot \ \text{measured spectrum}(\lambda) \tag{2.2}$$

therefore

$$\text{c}(\lambda) = \frac{\text{black body curve}}{\text{measured spectrum}} \tag{2.3}$$

where c(λ) is the calibration constant, which can be used to correct the experimental data. Figure 2.3 shows the black body curve, the measured spectrum and the calibration constant.

Optical emission spectroscopy was also used to determine the electron temperature (τ_{ex}) in the plasma. Considering that within a plasma, hydrogen atom's transitions to

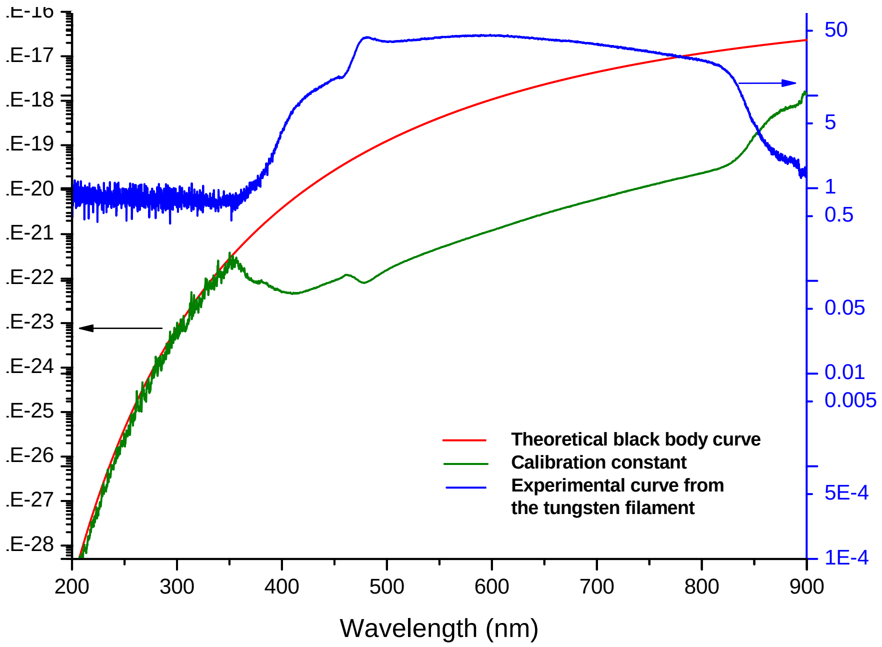

Figure 2.3: OES calibration curve.

a higher energy state are driven by collisions with electrons, we can use the ratio of the emission lines from H_β $(4 \rightarrow 2)$ and H_α $(3 \rightarrow 2)$ to calculate the electron temperature assuming that it depends on a Maxwell-Boltzmann distribution.

τ_{ex} can be deduced with the following equation:

$$\frac{\mathrm{H}_\alpha}{\mathrm{H}_\beta} = \frac{\lambda_{H\beta} A_{H\alpha} \vartheta_{H\alpha}}{\lambda_{H\alpha} A_{H\beta} \vartheta_{H\beta}} exp(\frac{\varepsilon_{H\beta} - \varepsilon_{H\alpha}}{k\tau_{ex}}) \qquad (2.4)$$

Where $\lambda_{H\beta}$ and $\lambda_{H\alpha}$ are the H_β and H_α wavelengths, respectively. A_α and A_β are transition probabilities, $\vartheta_{H\beta}$ and $\vartheta_{H\alpha}$ are statistical weights, $\varepsilon_{H\alpha}$ and $\varepsilon_{H\beta}$ are excitation energies, k is the Boltzmann constant, τ_{ex} is the electron temperature. The values used are shown in the table 2.1.

Table 2.1: Values used in equation 2.4.

Constant	**Value**
$\lambda_{H\beta}$	486 nm
$\lambda_{H\alpha}$	656.3 nm
A_α	6.47 x 10^7 s^{-1}
A_β	2.06 x 10^7 s^{-1}
$\vartheta_{H\beta} = \vartheta_{H\alpha}$	6
$\varepsilon_{H\alpha}$	12.0875 eV
$\varepsilon_{H\beta}$	12.7485 eV
κ_β	8.617 x 10^{-5} eVK^{-1}

2.3.2 Mass Spectroscopy

Mass spectroscopy analysis was done using a HAL 7RC (2U) from Hiden Analytical Ltd. with Quadrupole Mass Spectrometer controller. Gas samples were extracted from the reactor through the CF 250 port in the front of the chamber via a 2.2 m long, heated capillary with an inner diameter of 2.16 mm. The sampling pressure was in the range of $2 - 2.2$ x 10^{-5} torr in the first stage of the two-stage pumping system which consists of turbomolecular and dry rotary pumps. The gas was analysed with a quadrupole mass spectrometer (HAL 7RC 2U). The data was acquired using the Bar Mode in the range of 1 to 200 amu.

2.3.3 Infrared Spectroscopy

FT-IR analyses were done using a Bruker IFS 66v/S spectrometer equipped with a nitrogen-purged IR microscope (aperture $\geq$50 μm) with a resolution of 1 cm^{-1}. Every sample was studied at several points in order to assess its homogeneity. Spectra were obtained at room temperature over a frequency range of 900-3500 cm^{-1}. For nanodiamond powder samples, KBr pellets of 13 mm containing the sample were made.

2.3.4 Raman Spectroscopy

Raman spectra (inVia Raman microscope, Renishaw Ltd) were recorded using the 514.5 nm line of an argon ion laser through a 50x objective lens forming a spot size of 1.25 μm on the sample. The data was acquired using 50% power intensity from 200 to 2000 cm^{-1} Raman shift giving 10 seconds of exposure time and taking 3 accumulations in each analysis. The results were fitted using Gaussian profiles in OriginLab© Data Analysis and Graphing Software.

2.3.5 X-ray Photoelectron Spectroscopy

XPS measurements, using Al K_α(hv=1486.7 eV) X-radiation, were carried out in a Scienta ESCA300 spectrometer at the National Centre for Electron Spectroscopy and Surface Analysis (NCESS) UK. Deconvolution of XPS peaks was performed using XPSPeak41 software.

2.3.6 Scanning Electron Microscopy

SEM analyses were performed in a Hitachi 2700 SEM, operated at 10 keV electron energy and with a secondary electron emission detector. Low magnification SEM micrographs were analysed using a simple Matlab algorithm that counted the pixels corresponding to the diamond film. That is, the colour of each pixel in an SEM micrograph is represented by a number with values in the range of 0 to 255. Black pixels correspond to the minimum number 0 and white pixels to the maximum number 255 in grayscale. If the contrast of the micrographs is correctly adjusted the differences between the black graphite substrate and the ligh grey diamond film is clearly seen and can therefore be counted.

The algorithm used is the following:

```
clear all;
x = 0;
I=imread('C:\directory\subdirectory\filename.bmp');
for i=1:m;
for j=1:n;
if I(i,j)>=a;
x=x+1;
end;
x
```

for a `n` x `m` matrix, `'I'` can go from 0 to 255, and `a` is the minimum number in the black and white scale to be counted.

Chapter 3

Removal of non-diamond material in nanocrystalline diamond produced by detonation synthesis

3.1 Introduction

Detonation nanodiamond (DN) was discovered by Titov et al. in 1963 [113] in the former Soviet Union under classified research work. Not much happened in the next forty years until Ôsawa and collaborators [114] were able to isolate the small diamond particles. Today, there is a lot of interest in nanodiamond because of its extraordinary properties and its commercial applications, including: seeding for CVD diamond films and larger crystals growth [115], reinforcing components for transparent and engineering plastics, metals, alloys, glasses and ceramics [116], additive in cooling fluids [117], optical enhancement component for reflective polymer films, wear-resistive lubricants [118], electroplating baths [119], fine polishing, flat-panel displays, fluorescent cell-imaging and cell-therapy [120], drug delivery, stable catalyst support and chemically resistant chromatographic materials.

DN has a narrow (∼1-10 nm) particle size distribution, peaking at ∼5 nm [121] and it has hydrogen atoms terminating the carbon surface.

DN is synthesised by explosion reaction which is a technique based on the detonation transformation of carbon-containing explosives. The product is a mixture of nanodiamond particles, micrographite, carbon black, metal oxides and other impurities coming from the detonation chamber or the explosives used.

To purify the products most manufacturers employ wet chemistry which involves the use of acid boiling at high pressure, high temperature conditions for several days. The procedure removes metals that came from the reaction chamber and part of the non-diamond compounds but it does not provide enough purity, leaving black or dark-gray colour non-diamond particles. Alternative dry chemistry approaches are also used: these include catalyst-assisted oxidation [122], oxidation using boric anhydride as an inhibitor of diamond oxidation [123] and ozone-enriched air oxidation [124]. All of them use toxic and aggressive substances and in most of the cases supplementary catalysts are required.

Another approach has been the annealing of DN in oxygen atmosphere which can remove most carbon contaminations [125], but the procedure has to be done in very controlled conditions because it can also remove diamond.

The use of DN is limited not only because of the impurities and the difficulties to remove metals and non-diamond material but also, because nanodiamond particles are inside the core of the detonation soot[126] where amorphous carbons and diamond particles are likely to be bound to each other by chemical bonds (Figure 3.1). This problem has been solved using a combination of ultrasonic treatment and zirconia bead-milling, which destroys agglutinated structures and produces an aqueous suspension of isolated, $\sim$ 5 nm size DN particles usually called ultradispersed diamond (UDD) or monodispersed single nanodiamond (DSND)[127, 128]. However the graphitic fragments and zirconia particles from collision of microbeads remain in the resulting colloid due to their small size.

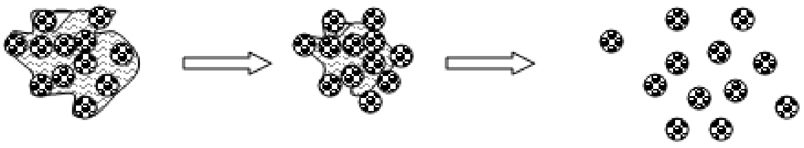

Figure 3.1: Representation of how the agglutinates are destroyed by acid treatment and bead milling.

After the complicated cleaning process DN has to be handled carefully because its surface is unstable and quickly absorbs water and atmospheric hydrocarbons after exposure to ambient conditions [129]. It can be easily transformed into graphite by shock, like bead-milling, and it can be oxidized by air to form oxygen-containing functional groups such as non-diamond C-C, C=C, C-H_x, C-O and C=O species which have been widely detected by X-ray and neutron diffraction.

This chapter presents the results obtained from the purification of commercial detonation nanodiamond. The resulting powders were used in following experiments for the pretreatment of graphite substrates. The methodology consisted of 1) the removal of metals using hydrochloric acid solution; 2) the oxidation of non-diamond phases by using strong oxidising agents and 3) the removal of oxide groups and hydrogenation of the nanodiamond surface by heating the sample in a hydrogen atmosphere. The hydrogen treatment is important to saturate surface dangling bonds and to avoid the chemisorption of other species which could form functional groups [130]. The experiments were designed considering the work previously done on nanodiamond surfaces in our research group but also based on procedures reported as good cleaning methods [128, 130, 131]. Although we were aware that breaking the agglutinated particles without the bead-milling process is extremely difficult we were able to improve the quality of DN suffieciently to use it in our next experiments. The characterisation during the different cleaning steps was done by preparing pellets that were analysed by FTIR.

3.2 Experimental

In order to remove the metallic impurities from commercial detonation nanodiamond (Alit Co., Ukraine) ∼0.5 grams of the powder were mixed with 100 ml of a solution prepared using 18% hydrochloric acid (HCl, AnalaR*, 37%) in deionised water. The solution containing ND was heated to around 80 °C for two hrs using a hot plate with magnetic stirring. Then it was let to cool down and rinsed with deionised water at least 4 times. After decantation the resulting powder was mixed with 100 ml of one of the acid mixtures shown in Table 3.1 in order to oxidise non-diamond compounds and functional groups in the DN surface. These four acid mixtures were prepared using: 1) perchloric acid ($HClO_4$, Sigma Aldrich, 70%) and nitric acid (HNO_3, AnalaR*, 69%) in six to one concentration (6:1); 2) HNO_3 and sulphuric acid (H_2SO_4, R.P. Normapur AR*, 95%) in two to one concentration (2:1); 3) $HClO_4$ and H_2SO_4 in six to one concentration (6:1); 4) HNO_3, $HClO_4$ and H_2SO_4 in four to three to one concentration (4:3:1). The solutions containing the ND were refluxed (see Figure 3.2 for experimental setup) at 180 °C with magnetic stirring for 4 hours until the colour of the suspension changed from black to light brown. Additionally, a solution containing DN and the first acid mixture mentioned before was treated using an ultrasonic bath (Bandelin Sonorex Digital 10P) for two hours at 50 °C, then refluxed for four hours. After the reflux the powders were rinsed three times with deionised water and dried in *vacuo*. In order to remove the oxidised species and to hydrogenate the dangling bonds the samples were put inside a tubular furnace with a hydrogen atmosphere and treated at 800 °C for 4 hours.

To analyse the powders by FTIR before, during and after the cleaning process, pellets of 1 gr using 0.99 gr KBr and 0.01 gr of DN were made. The FTIR spectrometer and the experimental parameters used are described in Chapter 2.

Table 3.1: Experimental conditions for the nanodiamond oxidation treatment.

Acid Mixtures	Time on hot plate (hours)
$HClO_4$ / HNO_3 (6:1)	4 2 (in ultrasonic bath), 4 (on hot plate)
HNO_3 / H_2SO_4 (2:1)	4
$HClO_4$ / H_2SO_4 (6:1)	4
HNO_3 / $HClO_4$ / H_2SO_4 (4:3:1)	4

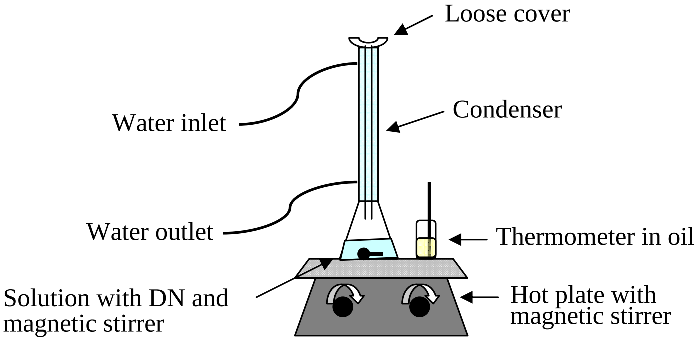

Figure 3.2: Experimental setup for oxidation treatment in fumehood.

3.3 Results

Figure 3.3 shows the FTIR spectra obtained after the oxidation treatment with the different acid mixtures and for the untreated powder. The spectra can be divided in five regions: 1) 3700-3100 cm^{-1} corresponding to OH, NH and CH vibrations; 2) 3000-2700 cm^{-1} vibrations from CH_3- and CH_2-; 3) 1800-1500 cm^{-1} C=O and N=O vibrations; 4) 1400-1000 cm^{-1} C-O-C and CH vibrations; 5) 850-550 cm^{-1} NO_3 and NCO vibrations. As a reference, in Table 3.2 are the main functional groups commonly found in nanodiamond synthesised by detonation. Figure 3.4 shows the FTIR spectra after the hydrogenation treatment for all samples and untreated nanodiamond. It is clear that after hydrogenation most of the groups containing oxygen disappear and only bands from nitrogen impurities and vibrations belonging to C-H groups remained.

The samples were weighed before and after the cleaning procedure to calculate the reaction yield. Unfortunately, even after a second decantation, some of the powder

Table 3.2: Main functional groups found in nanodiamond synthesised by detonation technique [130, 132–134].

Functional Group	Absorbance frequency (cm^{-1})	Vibration type
NH_2 in amines	3550-3330	Asymmetric stretch
	3450-3250	Symmetric stretch
OH solids	3300	Stretching of O-H bonds
	1043	
Sulfonamides $C\text{-}SO_2\text{-}N$	3330-3250	Asymmetric stretch NH_2
	1380-1310	Asymmetric stretch
	1180-1140	Symmetric stretch
	910-900	Stretching of $S\text{-}N\text{-}(H_2)$
Aliphatic CH	3000-2700	Stretching of C-H
	1475-1450	Asymmetric deformation
	1383-1377	Symmetric deformation
$(R\text{-}O\text{-})CH_3$	2992-2955	Asymmetric stretch
	2897-2867	Symmetric stretch
Aliphatic $\text{-}N\text{-}CH_3$	2805-2780	Symmetric stretch
Carbonyl (C=O)	1900-1550	Asymmetric stretch
$O\text{-}NO_2$	1660-1625	Asymmetric stretch
	1285-1270	Symmetric stretch
	870-840	N-O stretch
	760-745	Out of plane deformation
	710-690	NO_2 deformation
Organic nitrates (N=O)	1660-1450	
Nitro N=O	1556-1545	Asymmetric stretch
	1390-1355	Symmetric stretch
	835-820	
Aliphatic ethers C-O-C	1100-1085	Asymmetric stretch
Aliphatic amines C-N	Primary amine 1090-1068	Asymmetric stretch C-C-N
	Secondary amine 1146-1132	Asymmetric stretch C-N-C
SO_4^{2-}	1125-1080	Asymmetric stretch SO_4
	1270-1220	
Primary alcohol $CH_2\text{-}OH$	1075-1000	Stretching of C-O bonds
C-Cl	830-570	
Amide	630-550	

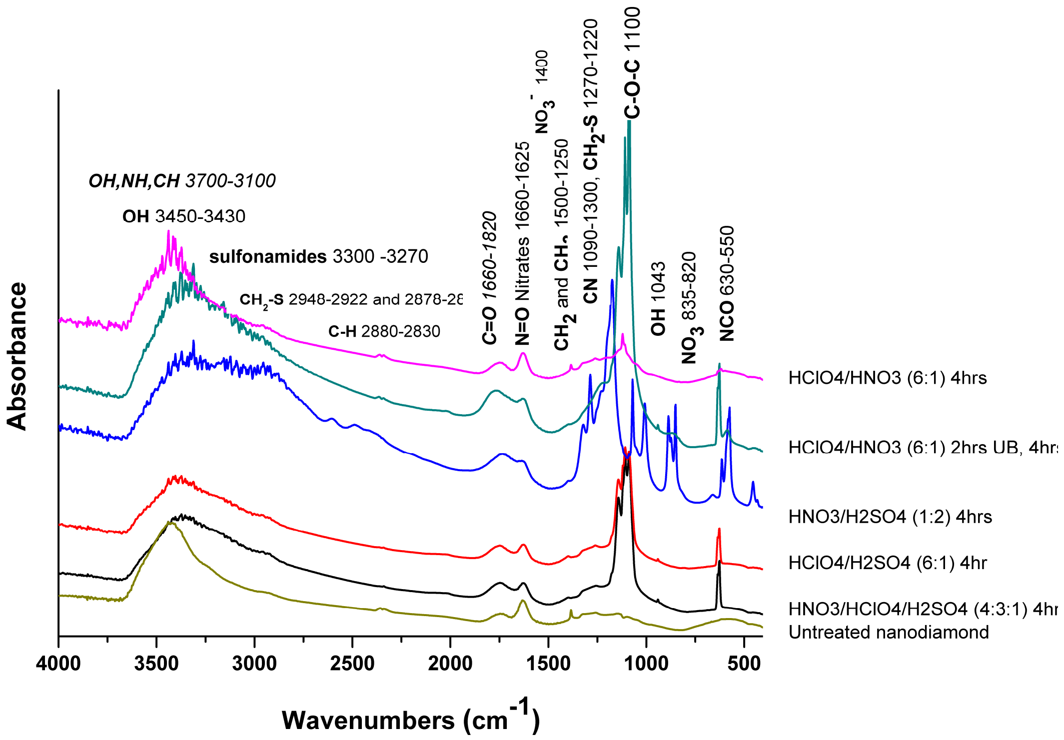

Figure 3.3: FTIR spectra of all samples obtained after oxidation treatment.

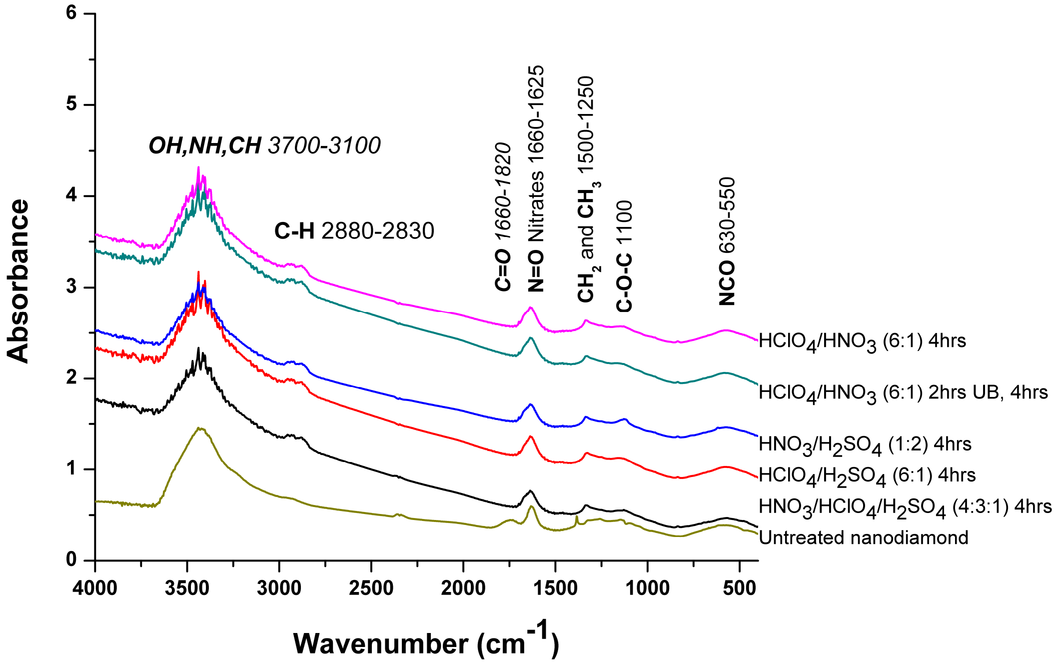

Figure 3.4: FTIR spectra of all samples obtained after hydrogenation treatment.

remains in the water used to wash the solutions (especially the very small particles), making it impossible to obtain a correct reaction yield. However, an approximation can be done from the calculated yields. The two samples with the highest mass loss were the DN treated with the mixture of HNO_3/H_2SO_4 (1:2) and the sample treated with the mixture of $HClO_4/H_2SO_4$ (6:1) that lost 33% and 31% respectively, of their original weight after hydrogenation. For the rest of the samples the weight lost is less than 17%. This means that HNO_3/H_2SO_4 (1:2) and $HClO_4/H_2SO_4$ (6:1) mixtures give the highest reaction yields since they can remove more impurities during the process.

SEM analysis after hydrogenation showed that there are still many agglomerates in the samples presenting particle sizes between a few microns and more than a hundred microns (see Figure 3.5).

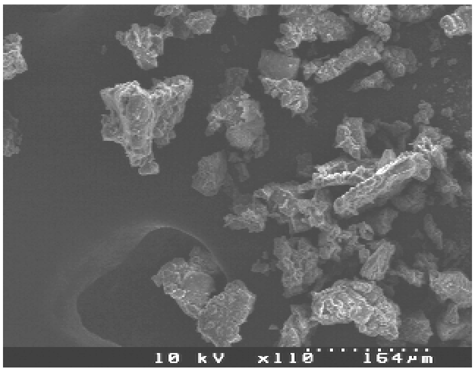

Figure 3.5: Soot containing nanodiamond powder after the cleaning process.

3.4 Discussion

The FTIR results from the oxidised powders showed that the oxide species produced during the reaction depend on the mixture of acid used, thus mixtures containing perchloric acid produce more carbonyl groups at 1140 and 1100 cm^{-1} (Figure 3.3). With the mixture containing only sulfuric and nitric acids the amides are formed instead, including bonded ν_{NH} between 3360 and 3320 cm^{-1}, combination band σ_{N-H} and ν_{CH} at 1305-1200 cm^{-1}, and the doublet 617 and 517 cm^{-1}, respectively.

The spectra shown in Figure 3.3 also contain vibrations at 3558, 3434 and 3245 cm^{-1}, assigned to OH stretching from adsorbed water. It had been reported that the intensity of this band decreases after heating the sample at 140 °C for 5 hours [130].

The band at $\sim$1630 cm^{-1} also appears in all the samples even after hydrogenation treatment. It is assigned to the amide group bonded in the bulk phase and in the surface. The presence of nitrogen groups in the diamond lattice is not surprising since DN production involves the use of nitrogen containing explosives.

It is also interesting how the ketonic carbonyl group at 1772 cm^{-1} and the amide group at 1630 cm^{-1} appear in all the samples but in different proportions. But it is even more interesting to compare the sample that had the ultrasonic bath treatment ($HClO_4/HNO_3$ mixture) with the sample that only had the oxidative reflux. The sample ultrasonically treated not only has a stronger 1772 cm^{-1} band but also huge differences in the intensities of the carbonyl groups at 1140 and 1100 cm^{-1}. Probably the ultrasonic bath helps to deagglomerate some of the big particles as has been reported by Xu et al. [135], however the intensity of our ultrasonic bath is not enough to separate the nanodiamond from the rest of the non-diamond particles.

Figure 3.4 shows the spectra of the powders after hydrogen treatment at 800 °C. The samples all look the same which indicates that the oxygenated species in the surface all reduce under the same conditions.

The spectra also show the increasing of the band intensities in C-H stretching region at 2952, 2922 and 2878 cm^{-1} which are assigned to ν_{asCH_3}, ν_{asCH_2} and $\nu_{\text{sCH}_2} + \nu_{\text{C-H}}$ respectively, suggesting the formation of surface hydrocarbon species.

Finally, one of the main changes in the hydrogenated sample's spectra is the absence of the C=O band near 1750 cm^{-1} that indicates the reduction of surface carbonyl groups to hydrocarbon species.

The increase of the time during the reflux with the acids (up to 42 hours [131]) and the use of other oxidase agents such as NaOH solution in water [136] may increase the amount of converted groups. However it seems that so far the only way to disintegrate the commercial nanodiamond agglutinates is to subject them to wet milling with zirconia micro-beads followed by a powerful sonication treatment [137].

3.5 Conclusions

The three step procedure carried out in this work (removing metal impurities, oxidising non-diamond material and reducing DN surface) reduced in part the non-diamond material but if a better quality DN is required, the use of other techniques such as ball milling and powerful sonication would be necessary.

FTIR spectra of DN showed that the different oxidising mixtures used produced different oxide species with amides and carbonyl groups being the most important. FTIR spectra after hydrogen treatment showed that most of the oxygen containing groups were reduced under the same conditions and only bands from hydrocarbons, hydroxyl from water and nitrogen-bound groups were detected.

Chapter 4

Study of nucleation treatments and microwave excitation power for CVD diamond films on graphite

During many years the experiments have demonstrated that growing diamond on graphite is very difficult, primarily because hydrogen etches graphite much faster than diamond under typical diamond growth CVD conditions [1].

There is very little information about the growth of diamond on graphite. The first reports date from the beginning of the 90's when Belton et al. [138] reported that diamond nucleation on platinum proceeded through the formation of graphitic carbon, which subsequently converted to hydrocarbon structures and then to diamond. Angus and co-workers [139–141] published a series of seminal papers on the hydrogenation of graphite. They suggested that hydrogenation occurs preferentially at the edges of graphite planes, transforming the unsaturated rings into their fully saturated analogues. In low pressure diamond growth environments the saturated rings result in diamond nucleation or even conversion to diamond as is shown in Figure 4.1.

Nucleation and epitaxial growth of diamond on different graphite planes has also been studied [142–144]. There is a consensus that nucleation is more facile at the prism or edge plane and is poor on the basal plane. There are also reports [145] concerning the enhancement of diamond nucleation on graphite by pre-coating of the surface with chromium, nickel or titanium. Graphitic carbon films have been used on silicon substrates [146] for equivalent purposes.

This chapter contains the results of the CVD diamond films grown on graphite substrates that were pretreated using different nucleation techniques. The experiments were done in two sets. The objective of the first set was to study how the conventional treatments to enhance diamond nucleation on silicon affect the growth on graphite.

The second set was thought with the intention to study how the morphology of the films is affected by substrate heat treatment before deposition. Heating the substrates in air or in nitrogen should oxidise or nitrogenate their surface.

The presence of oxygen or nitrogen during diamond deposition can influence the growth by changing the gas phase or by affecting the adsorption-desorption processes on the surface. When oxygen is present, both processes occur at the same time and it has been demonstrated that the changes produced by oxygen in the gas phase are closely related to the deposition rate [147]. Nitrogen influences diamond growth rates by changing absorption-desorption on the surface [148] or by impurity-induced step bunching [149].

It has also been proposed [75] that in the oxygen-containing plasmas, the O, O_2 and OH species can do some of the functions of the H atoms such as the etching of non-diamond carbon and the removal of unsaturated hydrocarbons in the gas phase.

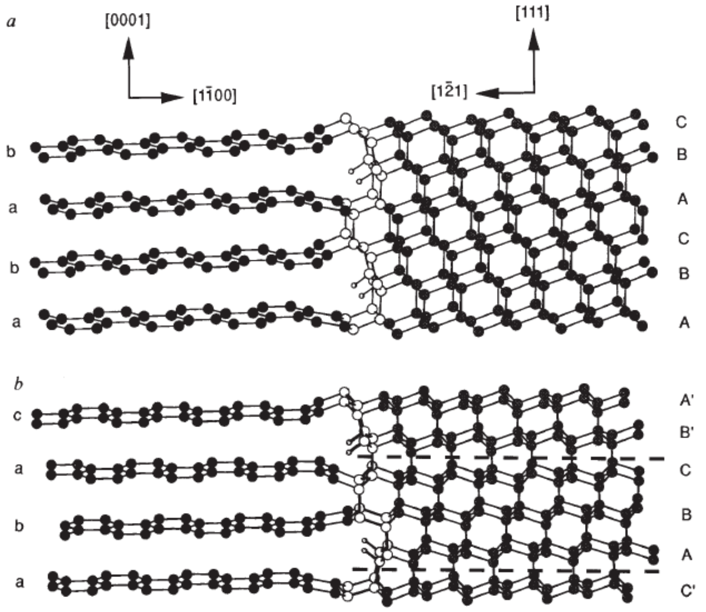

Figure 4.1: Side view of the relaxed structural models of the diamond nucleus on the [1$\bar{1}$00] prism plane of graphite: a) cubic diamond on perfect hexagonal graphite; b) twinned diamond nucleus adjoining a graphite stacking fault. Twin boundaries in diamond are presented by the dashed lines, hydrogen by the small open circles. The atoms shown as the larger open circles indicate the initial nucleus formed at the interface by tying together the graphite with tetrahedrally bonded carbon [139].

4.1 Experimental

Diamond films were grown in a stainless steel and quartz 6 kW microwave PECVD system (described in Chapter 2) having a base pressure of ~5 x 10^{-7} torr. During deposition, a mixture of 5% CH_4, 15% H_2 and 80% Ar was excited with 1.5, 3 or 3.6 kW power, with a pressure of 100 ± 2 torr for deposition times of 2 hours. These experimental parameters were chosen based on previous results obtained in our research group. The substrates were plasma heated and the temperature was measured in the range between 850 and 1100 °C using a two-colour optical pyrometer.

The substrates used for the experiments were 20 x 20 x 3 mm^3 graphite pieces (Ringsdorff Werke GmbH, Bonn, Germany). They were cleaned with methanol in an ultrasonic bath before the nucleation process.

Twenty three samples were prepared using different nucleation techniques and one control sample was grown on a pristine graphite substrate (see Tables 4.1 and 4.2). In some experiments the samples were sonically treated (Bandelin Sonorex Digital 10P ultrasonic bath, with variable power) for 30 min with a maximum power of 120 W_{eff}. The suspensions used were 3% solid in methanol, (solid = diamond (1 μm natural diamond, de Beers)), nanodiamond (previously cleaned as described in Chapter 3), or a mixture of diamond + titanium (100 mesh, 99.7% Sigma-Aldrich)). After the ultrasonic treatment the samples were rinsed in methanol and dried in vacuo or in oven. For the oven-dried samples, a box oven in atmospheric conditions or a tubular oven with nitrogen flow was used.

Table 4.1: Experimental conditions for graphite samples prepared using different nucleation pretreatments. Deposition condions for all the samples were 100 torr, 2 hours using a mixture of 5%CH_4/15%H_2/Ar.

Sample number	**Pretreatment**	**Deposition Power (kW)**
n9	Pristine graphite	1.5
n1	Silicon interlayer	1.5
n2	Manually scratched with diamond	1.5
n4	Scratched with nanodiamond	1.5
n5	Scratched with diamond + Titanium	1.5
n3	Scratched with diamond	1.5
n18	Scratched with diamond	3
n21	Scratched with diamond	3.6
n6	Plasma etching	1.5
n7	Ion bombardment	1.5
n8	Wear tracks	1.5

A layer of approximately 0.2 μm hydrogenated amorphous silicon was deposited for

Table 4.2: Experimental conditions for samples prepared using different nucleation pretreatments and heated in oven. Deposition condions for all the samples were 100 torr, 2 hours using a mixture of 5%CH_4/15%H_2/Ar.

Sample number	**Pretreatment**	**Heating in**	**Time**	**Temperature (°C)**	**Deposition Power (kW)**
n10	Silicon interlayer	air	2 days	200	3
n11	Scratched with diamond + Titanium	air	2 days	200	3
n12	Plasma etching	air	2 days	200	3
n13	No pre-treatment	air	2 days	200	3
n14	Scratched with diamond	air	18 hours	200	3
n15	Scratched with diamond	air	2 days	200	3
n16	Scratched with diamond	air	4 days	200	3
n17	Scratched with diamond	air	6 days	200	3
n19	Scratched with diamond	air	2 days	200	1.5
n20	Scratched with diamond	air	2 days	200	3.6
n22	Scratched with diamond	air	4 hours	400	3
n23	Scratched with diamond	nitrogen	4 hours	800	3
n24	Plasma etching	nitrogen	4 hours	800	3

10 minutes on two graphite substrates at 200 °C using a 1 kW microwave PECVD system with a mixture of 20% SiH_4/H_2 at 0.75 torr. One of these samples was treated after deposition in a box oven in atmospheric conditions for 2 days at 200 °C.

Manual scratching was carried out for 2 min using a slurry prepared with methanol and diamond powder. A pristine graphite substrate was etched in hydrogen plasma (1.5 kW) for 15 min. Two more graphite substrates were heated in air or in nitrogen and then etched in hydrogen plasma under the same conditions. Ion bombardment was accomplished with Ar at 1 kV for 15 min at a base pressure of 1.5 x 10^{-4} torr using a 3.0-1500-100 Ion Source (Ion Tech, INC). Scratching to produce wear-tracks was made with a diamond stylus leaving a square pattern of 1 mm distance between marks.

The resulting films were analysed by Scanning Electron Microscopy (SEM), Raman Spectroscopy, X-ray Photoelectron Spectroscopy (XPS) and Optical Emission Spectroscopy (OES) using the conditions described in Chapter 2.

4.2 Results

4.2.1 SEM analysis

Figure 4.2 shows a SEM micrograph of the control sample n9 presenting a cauliflower-like structure.

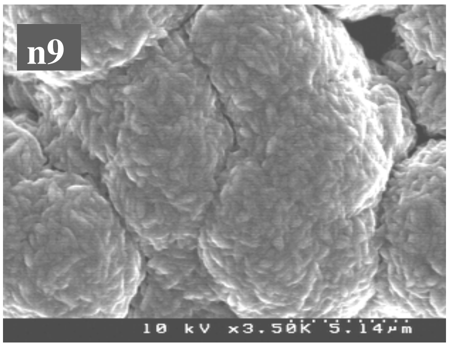

Figure 4.2: SEM micrograph from sample n9 presenting cauliflower-like structure.

Figure 4.3 shows SEM micrographs of samples n1, n2, n4 and n5. Sample n1 has a prickly shape, observable in profile at the surface of the larger features. This deposit consists of an array of individual diamond nanorod-like structures, similar to those recently reported by Shang et al. [150]. Sample n2 which was manually scratched has similar morphology to sample n1 with fine structure on the surface of the larger protuberances. A simple ultrasonic treatment with nanodiamond (sample n4) produces the frequently observed smooth "cauliflower-like" morphology that has resulted from growth on residual nanodiamond seeds. Sample n5 (scratched with diamond + Ti) consists of diamond crystals with submicron sizes and some visible {100} facets.

Figure 4.4 shows the SEM micrographs of samples n3, n21 and n18 corresponding to samples scratched with diamond and deposited using 1.5, 3.6 and 3 kW, respectively. Sample n3 has similar morphology of samples n1 and n2. Sample n21 shows micro-crystals with {100} and {111} faces. Finaly, sample n18, (a) has circular crystals, and (b) square crystals in the [100] orientation. We can also see in the grain frontiers smaller crystals in different orientations.

Figure 4.5 shows the SEM micrographs for the samples n6 to n8. Samples n6 and n7, have similar cauliflower-like morphology as samples n2 and n3, and this structure even exists on the untreated control sample n9 (in Figure 4.2). Sample n8 (scratched by diamond stylus), also presents cauliflower-like structure. The growth is mainly outside the tracks unlike previous observations on silicon substrates [151].

Figure 4.6 shows samples n10 to n13 which correspond to samples with different pretreatments and heated in air before deposition. Sample n10 has a silicon interlayer

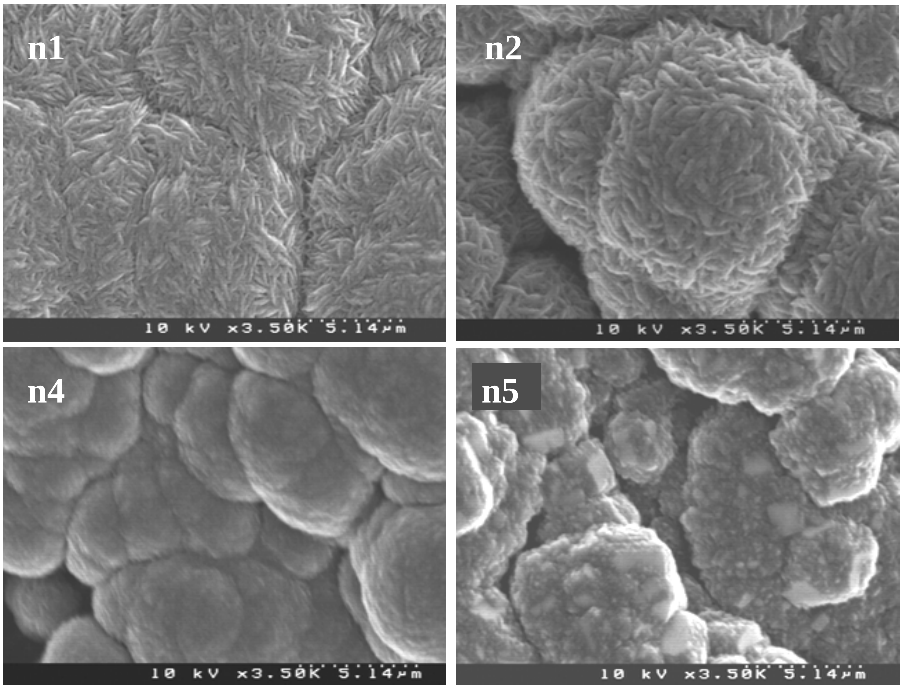

Figure 4.3: SEM micrographs from samples n1 to n4. Sample n1 shows nanorod-like structure; sample n2 shows fine structures on the surface of a larger protuberances, sample n4 shows cauliflower-like structure and sample n5 shows crystals with {100} facets.

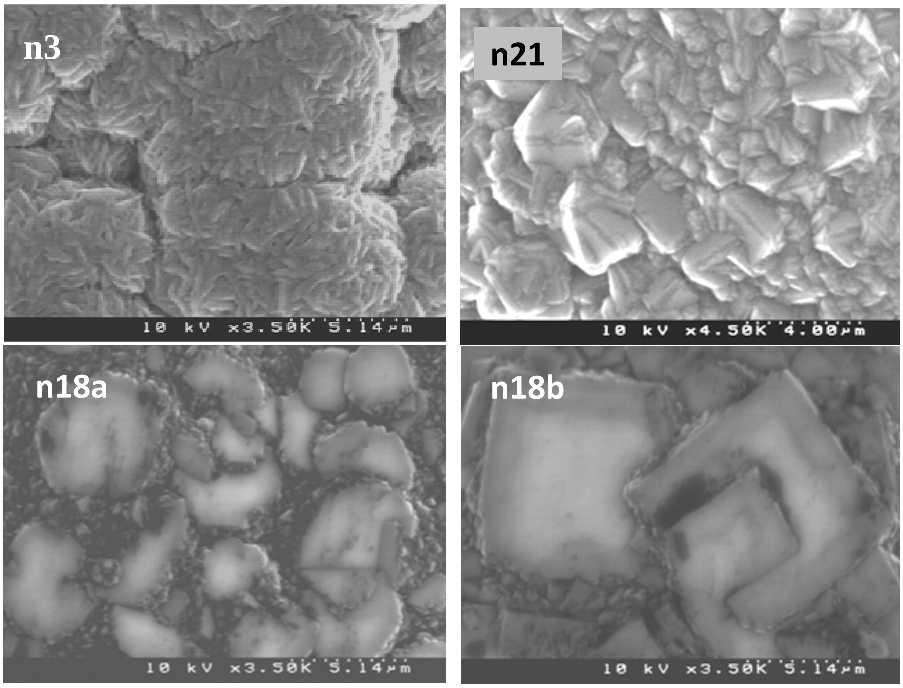

Figure 4.4: SEM micrographs from samples n3, n21 and n18 showing: (n3) fine structures on the surface of a larger protuberances, (n21) microcrystals with {100} and {111} faces and (n18a) circular crystals, (n18b) square crystals.

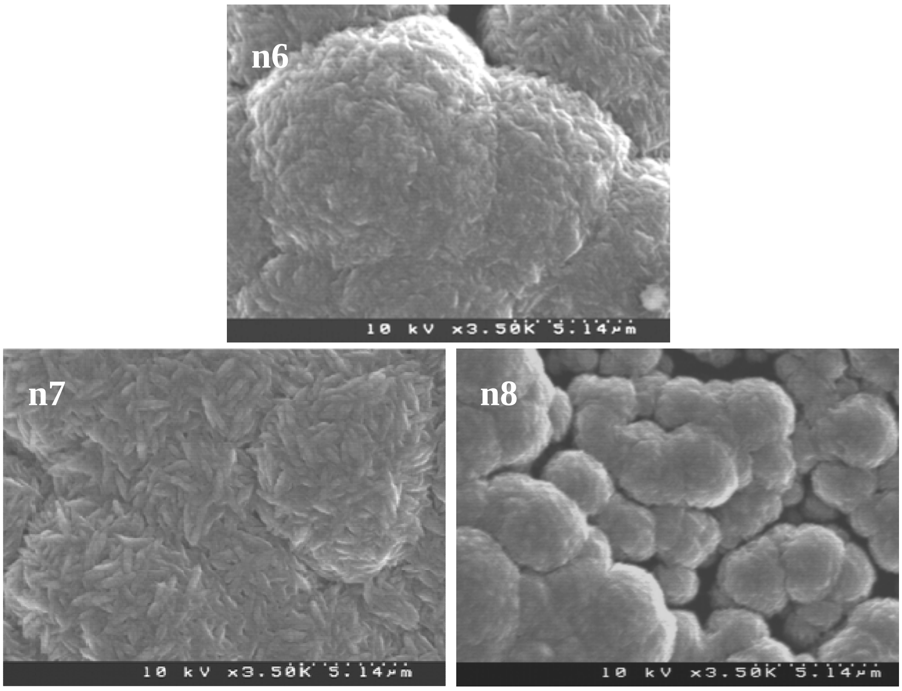

Figure 4.5: SEM micrographs from samples n6 to n8. Samples n6 and n7 show amorphous-like structure and sample n8 shows cauliflower-like structure.

as did sample n1 but the morphology is completely different. The sample n10 surface is rougher and has rounded particles in a wide range of sizes (hundreds of nm to $\sim$1 μm). Sample n11 shows similar morphology to sample n10 but with more uniform particle size. Samples n12 and n13 correspond to plasma etching and no pretreatment respectively: both have the nanorod-like structure, similar to sample n1.

Figure 4.7 shows samples n14 to n17, all of them were scratched with diamond and heated separately in air for 18 hours, 2, 4, and 6 days, respectively. The morphologies vary from nanorod-like (sample n14 and n17) to triangular microcrystals (sample n15) and rounded particles (sample n16).

Figure 4.8 shows the resulting films from the samples n19 and n20 that were sonically scratched with diamond and deposited using 1.5 and 3.6 kW power, respectively. The morphology of the sample n19 is very similar to the sample n3. Sample n20 has a shell-like structure with big crystals growing perpendicular to the picture plane.

Finally, Figure 4.9 shows the result from samples n22 to n24. Sample n22 was heated in air at 400 °C, followed by diamond deposition and it shows a surface made by small particles agglomerated in one direction to form bigger rod-like particles. Samples n23 and n24 were heated in nitrogen and they show a nanorod-like morphology and amorphous-like structure, respectively.

Table 4.3 contains a summary of the percentage of surface covered during deposition. These results were obtained using the Matlab algorithm described in chapter 2, page

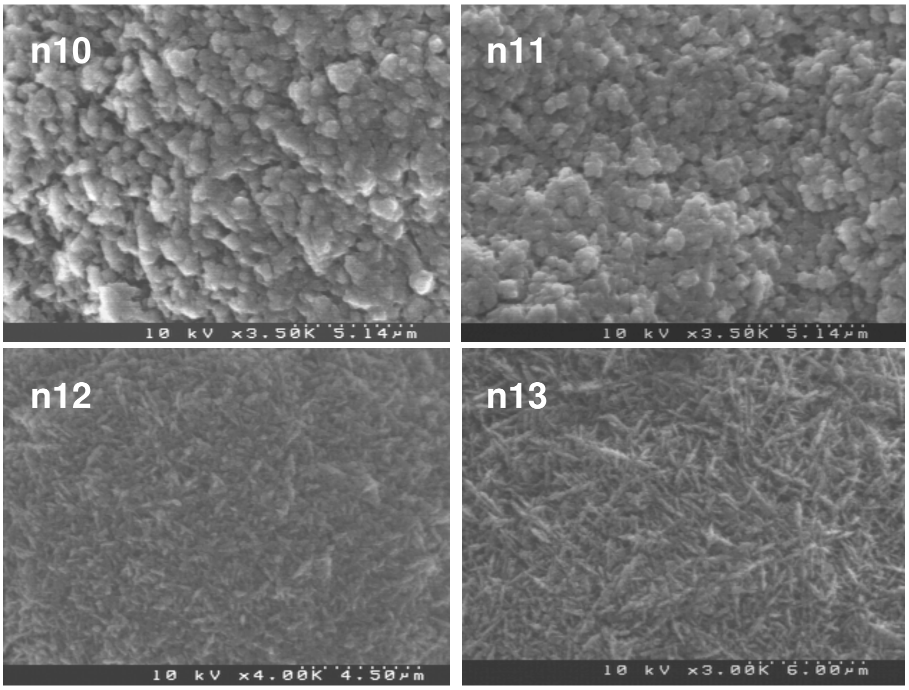

Figure 4.6: SEM micrographs from samples n10 to n13. Samples n10 and n11 show rounded crystals; samples n12 and n13 show nanorod-like structure.

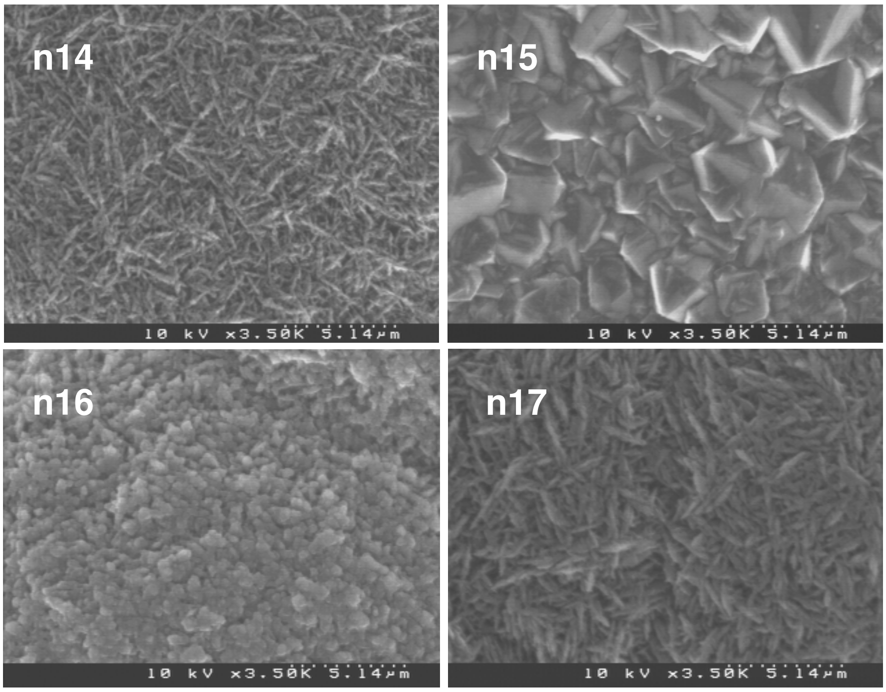

Figure 4.7: SEM micrographs from samples n14 to n17. Sample n14 and n17 show nanorod-like structure; sample n15 shows triangular microcrystals and sample n16 shows rounded crystals.

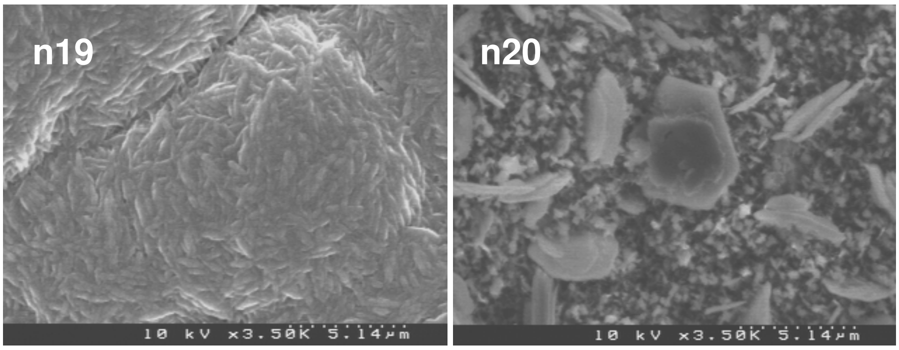

Figure 4.8: SEM micrograph from samples n19 and n20 showing fine structure on the surface of a larger protuberances and shell-like structure, respectively.

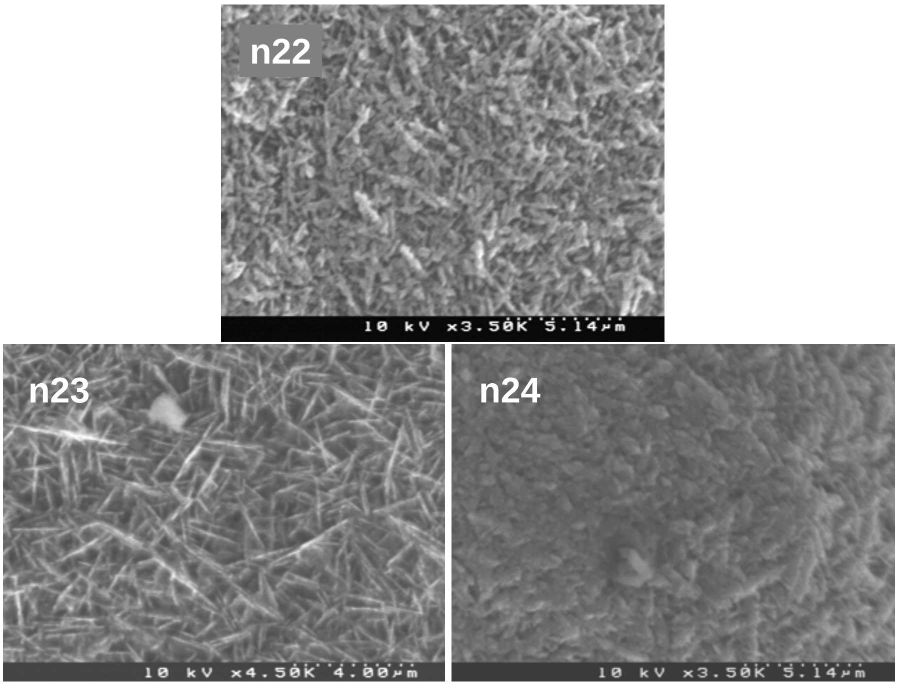

Figure 4.9: SEM micrograph from samples n22 to n24 showing: (n22) rod-like particles, (n23) nanorod-like morphology and (n24) amorphous-like structure.

Table 4.3: % surface covered by the film.

Sample	**% Surface covered**	**Sample**	**% Surface covered**
n9 Pristine substrate	67 ±0.5	n11 Scratched with diamond + Titanium	99 ±0.5
n1 Silicon interlayer	92 ±0.5	n12 Plasma etching	68 ±0.5
n2 Manually scratched with diamond	55 ±0.5	n13 No pre-treatment	99 ±0.5
n4 Scratched with nanodiamond	46 ±0.5	n14 Scratched with diamond	93 ±0.5
n5 Scratched with diamond + Titanium	69 ±0.5	n15 Scratched with diamond	96 ±0.5
n3 Scratched with diamond	78 ±0.5	n16 Scratched with diamond	99 ±0.5
n18 Scratched with diamond	97 ±0.5	n17 Scratched with diamond	99 ±0.5
n21 Scratched with diamond	87 ±0.5	n19 Scratched with diamond	99 ±0.5
n6 Plasma etching	92 ±0.5	n20 Scratched with diamond	93 ±0.5
n7 Ion bombardment	56 ±0.5	n22 Scratched with diamond	99 ±0.5
n8 Wear tracks	24 ±0.5	n23 Scratched with diamond	99 ±0.5
n10 Silicon interlayer	82 ±0.5	n24 Plasma etching	78 ±0.5

35. The values clearly vary depending on the nucleation pretreatment, some of the pretreatments increased considerably the diamond nucleation and promoted the production of an uniform film, on the other hand pretreatments such as ion bombardment and wear tracks decreased the nucleation compared with the control sample n9. In all cases the heating treatment (air or nitrogen) enhanced the nucleation density.

4.2.2 Raman Spectroscopy

Figure 4.10 shows the Raman spectra for the samples n1 to n5. They have a characteristic Raman spectrum of nanocrystalline diamond [152–155] which usually presents bands at: 1) ~1342 cm^{-1} and ~1584 cm^{-1} due to the D and G bands from graphite; 2) a peak at 1135 cm^{-1} which has been attributed to nanocrystalline diamond in some publications [156, 157] and transpolyacetylene [158] in others; 3) a peak at 1477 cm^{-1}, which is a companion mode of the 1135 cm^{-1} peak, but it has also been attributed to sp^3 bonding; 4) the band at 2699 cm^{-1} that is an overtone of the D band. The diamond peak at around 1332 cm^{-1} is only seen in sample n5, probably because it has bigger crystals. Usually the diamond peak is not observed from nanocrystalline diamond films because it is obscured by the overlapping D peak.

Figure 4.11 shows Raman spectra for non-scratched samples n6 to n9. Samples n6

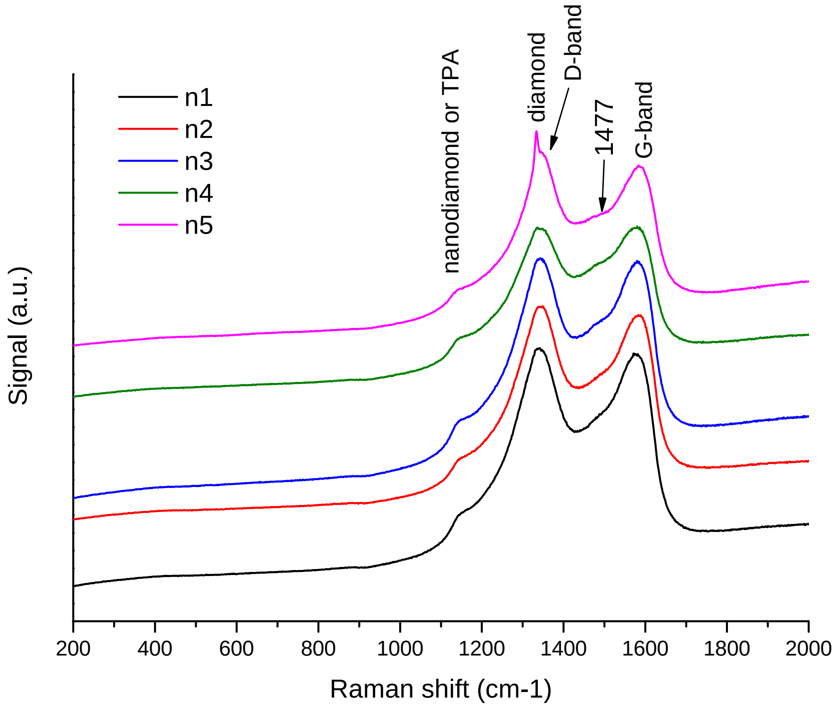

Figure 4.10: Raman spectra from scratched samples n1 to n5.

and n9 have the bands for nanodiamond mentioned before and samples n7 and n8 present only peaks from graphite.

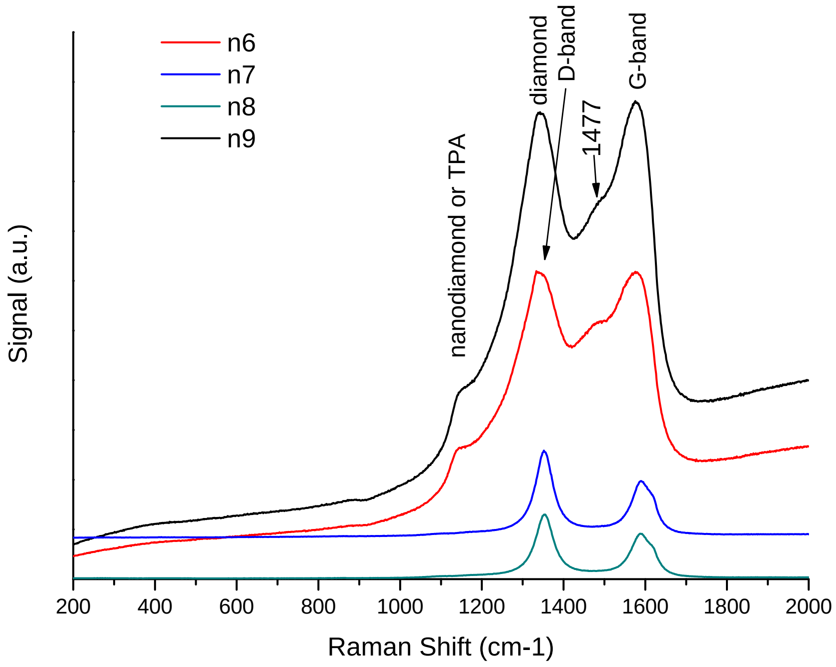

Figure 4.11: Raman spectra from the non-scratched samples n6 to n9.

Figures 4.12 and 4.13 contain the spectra of samples n10 to n24. In most of these samples the peak from diamond at ∼1332 cm^{-1} is visible, however contributions from the bands at 1135 and 1477 cm^{-1} are also observed in these samples.

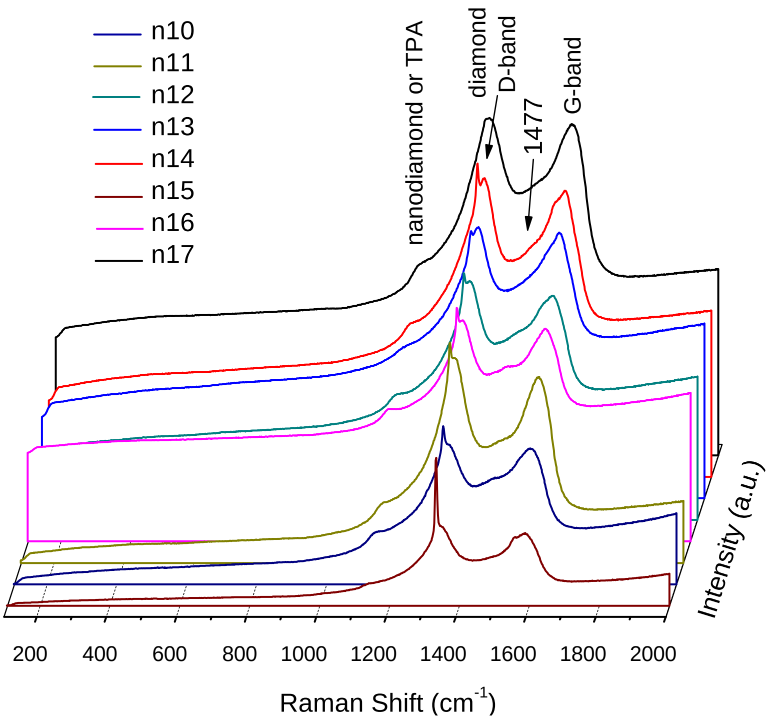

Figure 4.12: Raman spectra from samples n10 to n17. The spectra have the characteristic nanodiamond bands.

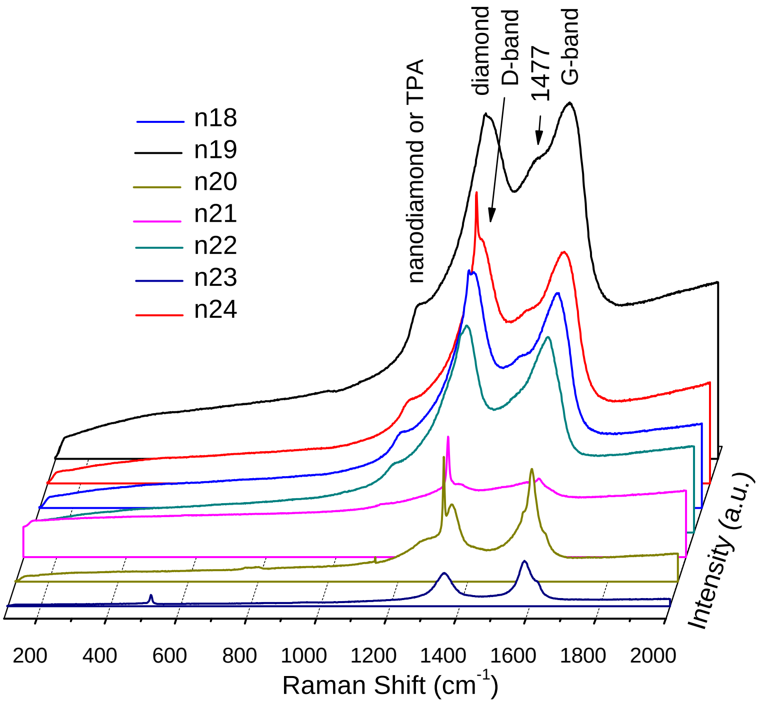

Figure 4.13: Raman spectra from samples n18 to n24. The spectra have the diamond peak at 1332 cm^{-1} but also contributions from graphite.

Table 4.4 contains the results from deconvolution of spectra with contributions from diamond and graphite bands. Full width at half maximum (FWHM) of peaks co-

Table 4.4: Parameters from deconvoluted Raman spectra.

	Diamond (sp^3)		**Graphite (sp^2)**		
Sample	**Peak** (cm^{-1})	**FWHM** (cm^{-1})	**Peak** (cm^{-1})	**FWHM** (cm^{-1})	**sp^3/sp^2**
n5	1333 ±0.6	7.4 ±1.2	1588 ±0.7	63 ±2	0.04 ±0.008
n10	1334 ±0.8	7.6 ±2.0	1574 ±2.0	109 ±4	0.02 ±0.005
n11	1333 ±0.5	6.2 ±1.1	1589 ±0.6	74 ±2	0.02 ±0.004
n12	1333 ±0.9	6.2 ±2.1	1576 ±2.1	103 ±4	0.01 ±0.004
n13	1332 ±0.2	6.2 ±0.5	1587 ±1.7	70 ±2	0.01 ±0.001
n14	1332 ±0.6	5.1 ±1.4	1574 ±3.4	91 ±4	0.02 ±0.003
n15	1333 ±0.1	5.7 ±0.2	1587 ±1.6	85 ±5	0.12 ±0.020
n16	1333 ±0.4	5.9 ±0.8	1590 ±0.8	74 ±3	0.03 ±0.006
n17	1334 ±2.0	7.8 ±2.0	1582 ±3.9	80 ±3	0.002 ±0.001
n18	1333 ±1.4	5.9 ±2.3	1582 ±1.5	84 ±2	0.006 ±0.004
n19	1334 ±0.9	9.6 ±2.0	1586 ±0.2	68 ±1	0.004 ±0.002
n20	1331 ±0.1	4.4 ±0.2	1584 ±0.3	15 ±1	0.54 ±0.070
n21	1320 ±0.02	6.7 ±0.04	1573 ±0.8	81 ±5	0.37 ±0.090
n22	1331 ±3.0	5.2 ±1.5	1578 ±2.0	85 ±3	0.002 ±0.003
n24	1333 ±0.2	5.2 ±0.5	1583 ±0.6	64 ±2	0.05 ±0.005

rresponding to diamond varies with different samples. The narrowest diamond line (FWHM 4.4 cm^{-1}) is from the sample n20 that was produced using 3.6 kW excitation power. It is known that the diamond peak width depends on the growth conditions for CVD diamond films, and can vary from rather broad (13 cm^{-1}) to widths comparable with natural diamond (2 cm^{-1}).

Finally, Figure 4.14 shows a deconvoluted spectrum from sample n15 which is typical of samples containing diamond and graphite peaks. The spectrum contains seven Gaussian curves from graphite, diamond, transpolyacetylene and/or disordered diamond.

4.2.3 X-ray Photoelectron Spectroscopy

XPS analysis was carried out on samples n1 to n9. As an example, Figure 4.15 shows a deconvoluted XPS spectrum from sample n5 that is typical of all samples. Table 4.5 contains the components of each spectrum in % area that were obtained by deconvolution of C1s band using XPSPeak41 software. Most of the samples contain five peaks corresponding to: carbon sp^3 at ∼284.4 eV; carbon sp^2 appearing at ∼285 eV; carbon bonded with oxygen (COH, COC, COOH, COOR) showing at ∼286 and

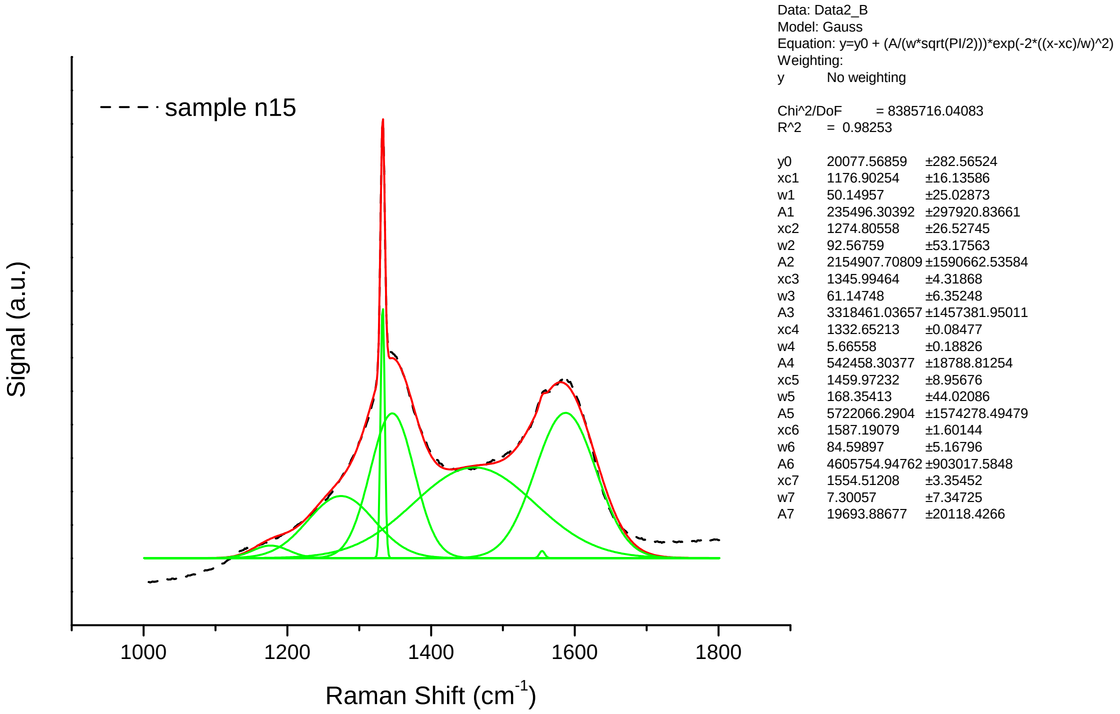

```
Data: Data2_B
Model: Gauss
Equation: y=y0 + (A/(w*sqrt(PI/2)))*exp(-2*((x-xc)/w)^2)
Weighting:
y          No weighting

Chi^2/DoF        = 8385716.04083
R^2      =  0.98253

y0       20077.56859    ±282.56524
xc1      1176.90254     ±16.13586
w1       50.14957       ±25.02873
A1       235496.30392   ±297920.83661
xc2      1274.80558     ±26.52745
w2       92.56759       ±53.17563
A2       2154907.70809 ±1590662.53584
xc3      1345.99464     ±4.31868
w3       61.14748       ±6.35248
A3       3318461.03657 ±1457381.95011
xc4      1332.65213     ±0.08477
w4       5.66558        ±0.18826
A4       542458.30377   ±18788.81254
xc5      1459.97232     ±8.95676
w5       168.35413      ±44.02086
A5       5722066.2904   ±1574278.49479
xc6      1587.19079     ±1.60144
w6       84.59897       ±5.16796
A6       4605754.94762 ±903017.5848
xc7      1554.51208     ±3.35452
w7       7.30057        ±7.34725
A7       19693.88677    ±20118.4266
```

Figure 4.14: Typical fitted Raman spectrum.

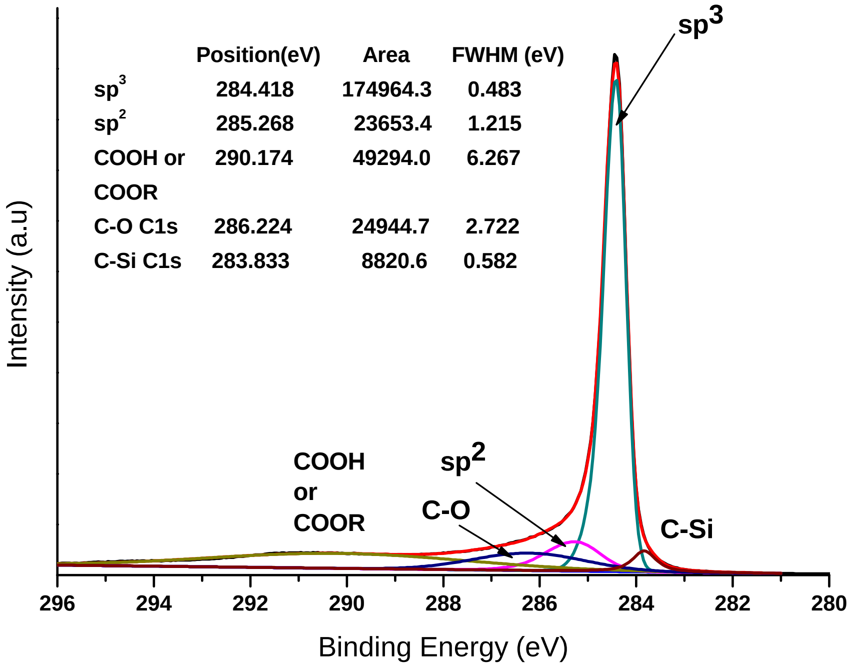

	Position(eV)	Area	FWHM (eV)
sp^3	284.418	174964.3	0.483
sp^2	285.268	23653.4	1.215
COOH or COOR	290.174	49294.0	6.267
C-O C1s	286.224	24944.7	2.722
C-Si C1s	283.833	8820.6	0.582

Figure 4.15: Typical XPS spectrum, corresponding to sample n5.

~290 eV and unexpectedly silicon carbide (SiC) showing at ~283.8 eV. In all cases the carbon sp^3 peak is the highest component [159–161].

Table 4.5: Peaks %area of deconvoluted XPS C1s spectra from samples n1 to n9.

Sample	**sp^3 (%)**	**sp^2 (%)**	**Alcohol or ether(%)**	**Carboxylic acid or ester (%)**	**SiC (%)**	**sp^3/sp^2**
n1 Silicon interlayer	69.6	29.3	−−	−−	1.1	2.4
n2 Manually scratched	60.5	21.1	11.6	5.4	1.3	2.8
n3 Scratched with diamond	76.3	16.5	−−	5.1	2.1	4.6
n4 Scratched with nanodiamond	56.8	15.2	11.3	15.8	0.9	3.7
n5 Scratched with diamond + Titanium	62.1	8.4	8.9	17.5	3.1	7.4
n6 Plasma etching	58.2	31.1	8.8	1.9	−−	1.8
n7 Ion bombardment	58.3	10.4	17.1	13.0	1.2	5.6
n8 Wear tracks	54.2	11.1	17.0	16.1	1.6	4.9
n9 Pristine substrate	83.4	9.3	5.9	−−	1.5	8.9

The following results were obtain after the thesis completion but are included to leave a record and more information about the prepared diamond films. Figure 4.16 shows sp^3/sp^2 ratio for samples n10 to n24. We can appreciate that the nucleation pretreatment in samples n10 to n13 has an effect on the quality of the film, and that sample n10 has the highest sp^3/sp^2 ratio. Sample n14 to n17 were heated during different periods of time and we can see that sample n17 that was heated for 6 days shows the highest sp^3/sp^2 ratio. Higher microwave power in sample n20 decreased the quality of the film compared with sample n19 but the contrary effect resulted in sample n21. Plasma etching pretreatment of sample n24 increased the quality of the film compared with sample n23.

Figure 4.17 shows oxygen content for samples n10 to n24. Sample n20 contains considerably more oxygen than the rest of the samples. A possible reason can be due to the morphology of the film and the fact that the substrate surface is not completely covered.

Figure 4.18 shows sp^3/sp^2 ratio for samples tc5 to etc8. It is clear that sp^3/sp^2 ratio increases after hydrogen treatment, which is due to preferential etching of non-diamond carbon.

Figure 4.19 shows oxygen content for samples tc5 to etc8. Oxygen content decreases after hydrogen treatment, suggesting that surfaces are oxygenated after deposition, even if the samples are left with hydrogen flow for a short time after completing the

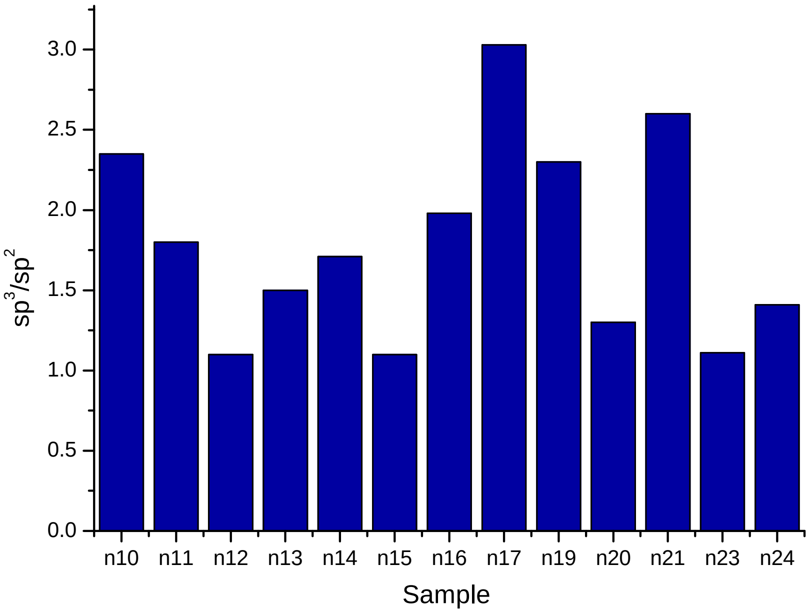

Figure 4.16: Graph showing sp^3/sp^2 ratio for samples n10 to n24.

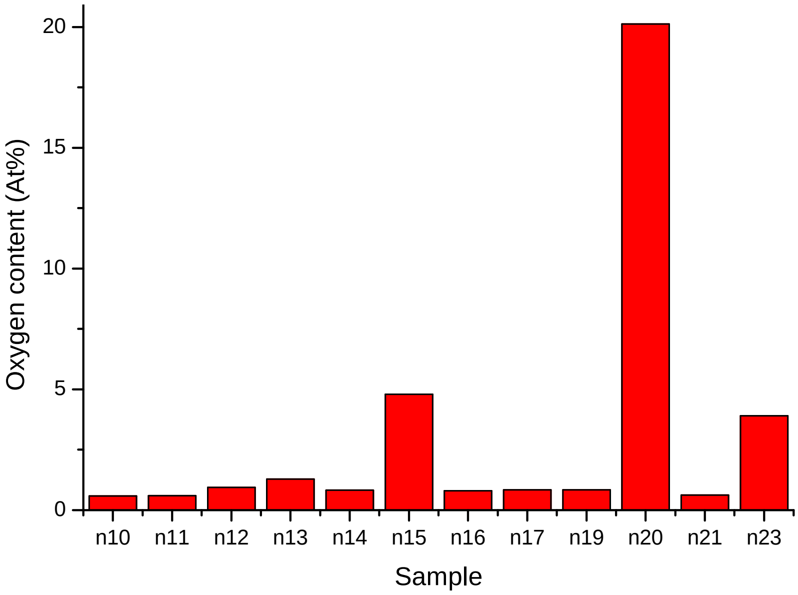

Figure 4.17: Graph showing oxygen content for samples n10 to n24.

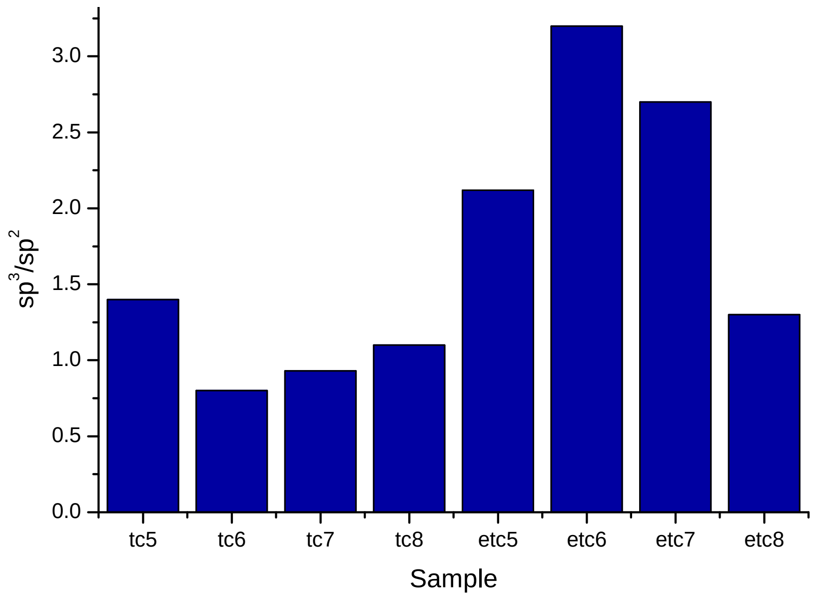

Figure 4.18: Graph showing sp^3/sp^2 ratio for samples tc5 to etc8.

deposition.

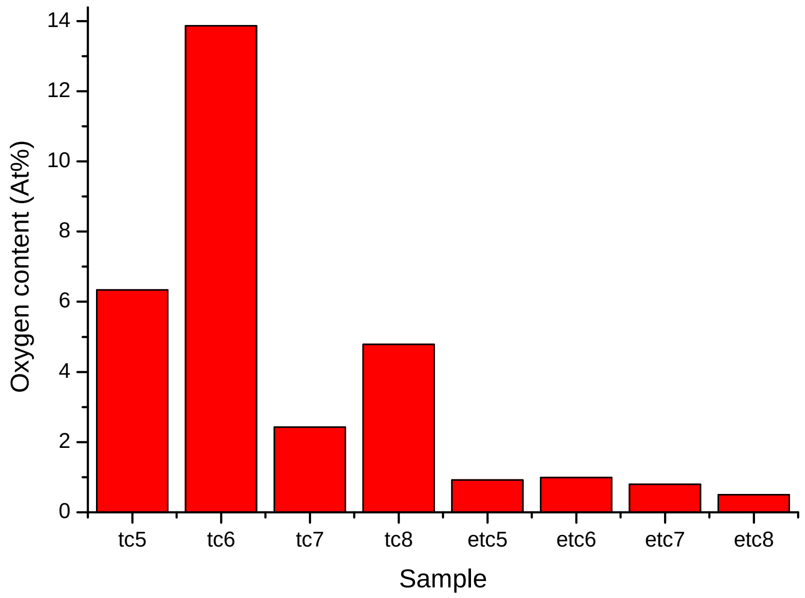

Figure 4.19: Graph showing oxygen content for samples tc5 to etc8.

Figure 4.20 shows the deconvolution of C1s region in sample tc6. This is a typical example of deconvolution of C1s region. Sample tc6 shows contributions from diamond (sp^3), graphite (sp^2), and carbon singly and doubly bonded to oxygen.

Figure 4.21 shows the deconvolution of C1s region in sample etc6. After hydrogen etching the deconvoluted C1s spectrum shows higher contributions of diamond, and less graphite and carbon bonded to oxygen.

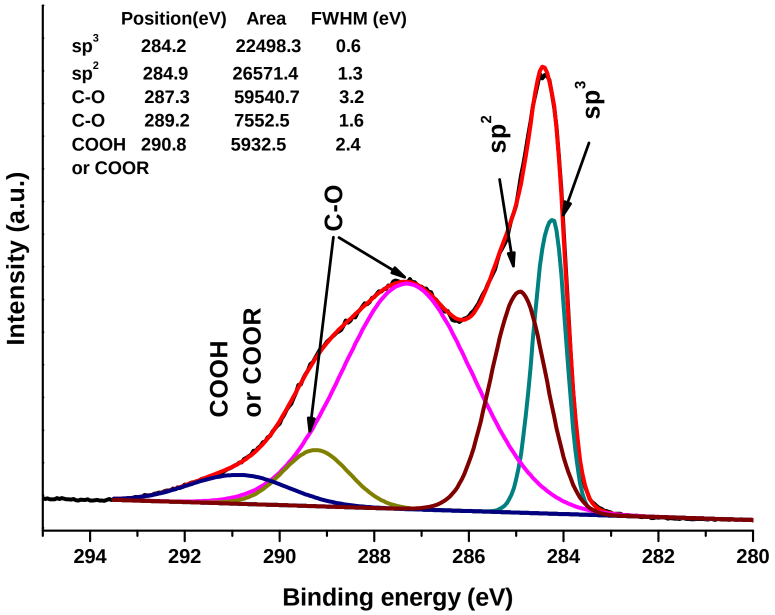

Figure 4.20: Deconvolution of C1s region in sample tc6.

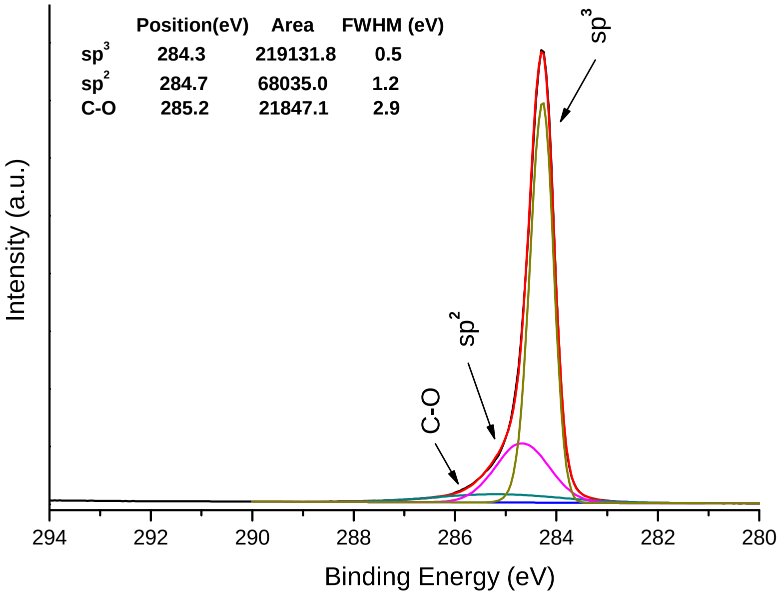

Figure 4.21: Deconvolution of C1s region in sample etc6.

4.2.4 Plasma analysis during deposition by Optical Emission Spectroscopy

Optical Emission Spectroscopy has been used to analyse the radiative species present in the plasma during deposition. Figure 4.22 shows the emission spectra for the samples n10 to n13, which are typical examples of the emission bands present in all samples. These bands are 388, 418, 430 and 776 nm from CH species; 471 and 516 nm are from C_2 Swan band; 656.5, 485 and 436 nm correspond to H_α, H_β and H_γ, respectively [162]. The spectra shown in this figure were taken after 10 min of deposition, when the intensities of the CH bands at 388 and 430 are usually higher due to the etching of the substrate, and they decrease with time. The change in the emission line intensity is important because it is directly related to the concentration of the species in the plasma. If the concentrations of the species change the chemistry during deposition may also change.

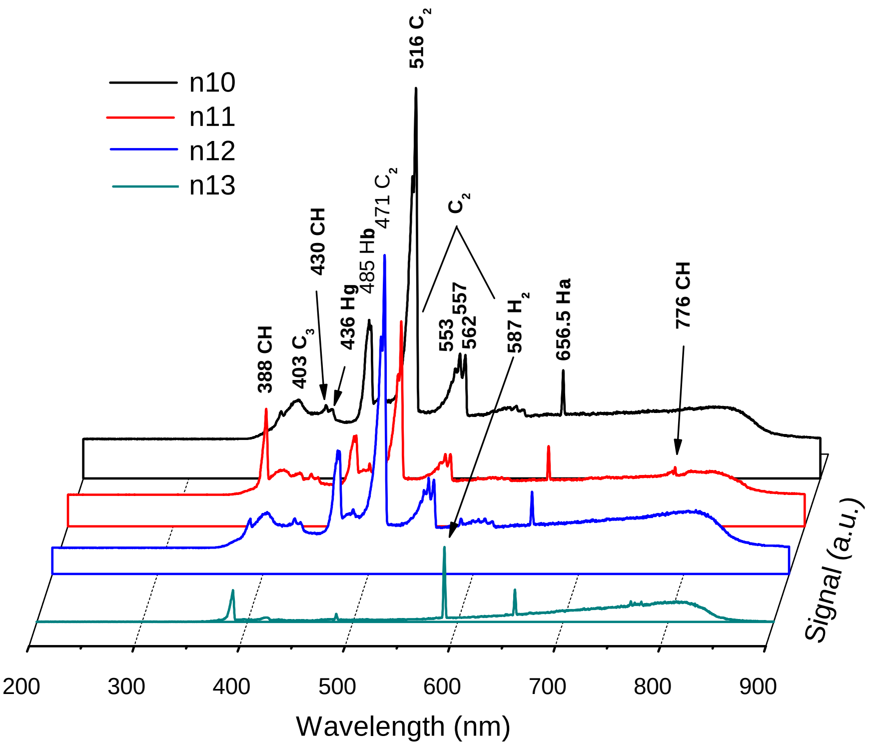

Figure 4.22: OE spectra after 10 min deposition.

Table 4.6 contains the ratios of the emission lines H_α/H_β (which is necesary to calculate the electron temperature (T_e))and CH/C_2 for all samples after 10 and 60 min deposition. The intensities were corrected for the detector sensitivity using the calibration constant obtained by the equation 2.1 described in Chapter 2. Table 4.6 also contains the respective electron plasma temperatures (T_e), obtained using the equation 2.4.

Table 4.6: OES data from the corrected spectra.

	10 min deposition			**60 min deposition**		
Sample	$\mathbf{H_\alpha/H_\beta}$	$\mathbf{CH/C_2}$	$\mathbf{T_e}$ (Kelvin)	$\mathbf{H_\alpha/H_\beta}$	$\mathbf{CH/C_2}$	$\mathbf{T_e}$ (Kelvin)
n1	48±8	0.03	2535±436	71±12	0.02	2247±390
n2	42±7	0.04	2657±457	62±11	0.03	2338±400
n3	40±7	0.46	2686±462	62±11	0.14	2336±400
n4	34±6	0.17	2854±490	43±7	0.20	2627±450
n5	33±6	0.23	2902±499	37±6	0.52	2766±470
n6	128±22	0.55	1914±329	65±11	0.23	2300±390
n7	42±7	0.10	2646±455	49±8	0.15	2518±430
n8	42±7	0.12	2645±455	50±8	0.10	2507±430
n9	46±8	0.10	2574±442	46±8	0.10	2567±440
n10	39±7	0.16	2718±467	47±8	0.11	2552±440
n11	37±6	0.05	2779±477	147±25	0.01	1851±320
n12	319±55	4.92	1558±267	58±10	0.63	2385±410
n13	40±7	0.08	2709±465	40±7	0.17	2686±460
n14	61±10	0.05	2351±404	120±21	0.01	1944±330
n15	39±7	0.17	2720±467	47±8	0.11	2560±440
n16	40±7	0.11	2689±462	54±9	0.09	2434±420
n17	39±7	0.13	2718±467	41±7	0.17	2669±460
n18	71±12	1.01	2243±385	38±12	0.37	2754±470
n19	41±7	0.36	2678±460	142±24	0.02	1865±320
n20	37±6	0.14	2763±475	41±7	0.16	2680±460
n21	64±11	0.07	2309±397	71±12	0.035	2244±390
n22	42±7	0.04	2661±457	67±12	0.36	2278±390
n23	50±9	0.05	2501±430	88±15	0.03	2114±360
n24	192±33	0.90	1738±299	124±21	0.01	1927±330

4.3 Discussion

For silicon substrates, scratching pretreatments are usually more effective than the non-scratching ones, but for graphite substrates we can see that there is not a big difference. For example film morphologies of samples n2 (manually scratched with diamond), n3 (scratched with diamond), n6 (Plasma etching) and n7 (Ion bombardment) are very similar and the surface covered (Table 4.3) is even higher in sample n6 which received a plasma etching. This suggests that most of the diamond nuclei are formed on graphite and fewer on diamond seeds. This can also be seen on samples n2 and n7 which have even less area covered by diamond growth (∼55%) than the pristine sample (∼67%). Both of these samples are initialy covered by loose particles, these being diamond seeds and graphite etched by the ion beam. We believe that during diamond deposition, a graphite surface is hydrogenated forming nuclei or/and substrate etching. When etching is too high there is no diamond deposition. The substrate etching also introduces extra carbon into the plasma that may increase diamond nucleation. This is seen in sample n6 that has more surface covered compared with the pristine sample.

Samples n4 (scratched with nanodiamond) and n8 (wear tracks) had even less surface covered than the pristine sample and both of them presented cauliflower like structure. When producing the wear track in sample n8 the surface under the marks was flattened, which prevented diamond nucleation in these areas. In the case of sample n4, we have seen in previous experiments that the nanodiamond solution leaves a thin layer on the substrate surface. This happens because the colloid contains not only nanodiamond particles but also non-diamond particles that closely interact with each other [121]. Diamond nucleation on this layer was slower than on pristine graphite possibly because hydrogen etched this thin layer faster than prinstine graphite or because the non-diamond particles inhibited diamond growth. Silicon interlayer pretreatment on sample n1 increased diamond nucleation (92.3% surface covered) and the morphology of the film was different from the rest of the samples. Nuclei may have formed directly on the amorphous silicon. Sample n5 (scratched with diamond + Titanium) showed some large crystals (∼2μm) that may have formed due to low nucleation density in this sample: sometimes the species in the plasma attach to a growing surface, instead of forming new nuclei, producing big crystals.

Changes to the excitation power changed considerably the morphology of the films, for example samples n3, n18 and n21 (all of them scratched with diamond). They were pretreated under the same conditions but deposited using 1.5, 3 and 3.6 kW of power. The resulted morphologies went from amorphous-like (n3) to microcrystalline with {100} faces (n18), to microcrystalline with {111} faces (n21). When samples were heated in air after the scratching treatment, for example samples n19, n15, n20, and deposited using 1.5, 3 and 3.6 kW of power, we obtained different morphologies than these previously seen in samples deposited at 3 and 3.6 kW power (see Figures 4.8(n20) and 4.9(n21)). This suggests that the surfaces were modified during the heating treatment and it affected the nucleation process independently of the excitation power used during deposition, as long as the power was high (≥3 kW). We can also notice that the microcrystalline films are the ones deposited at 3 and 3.6 kW, indicating that the size of the crystals and ratio of sp^3/sp^2 are related to the power and not to the heating treatment.

Another factor that affected the morphology of the resulting films is the heating time as was seen in samples n14 to n17 (scratched with diamond) that were heated in air for 18 hours, 2, 4 and 6 days. Heating treatments promoted oxygen absorption as was seen by XPS analysis of a sample ultrasonically scratched and heated in air for 2 days (Figure 4.23). A pristine graphite substrate had ∼1.2 %at of oxygen, after heating the value increased to ∼14.5%at. As the heating time increased, the area of the surface covered also increased, for example, samples n14, n15 and n16 in Table 4.3, and then the surface covered decreased for samples heated for 6 days (sample n17). That could be due to surface erosion after prolongated heating periods. The change in the heating temperature also affected the final morphology (sample n22) and the surface coverage.

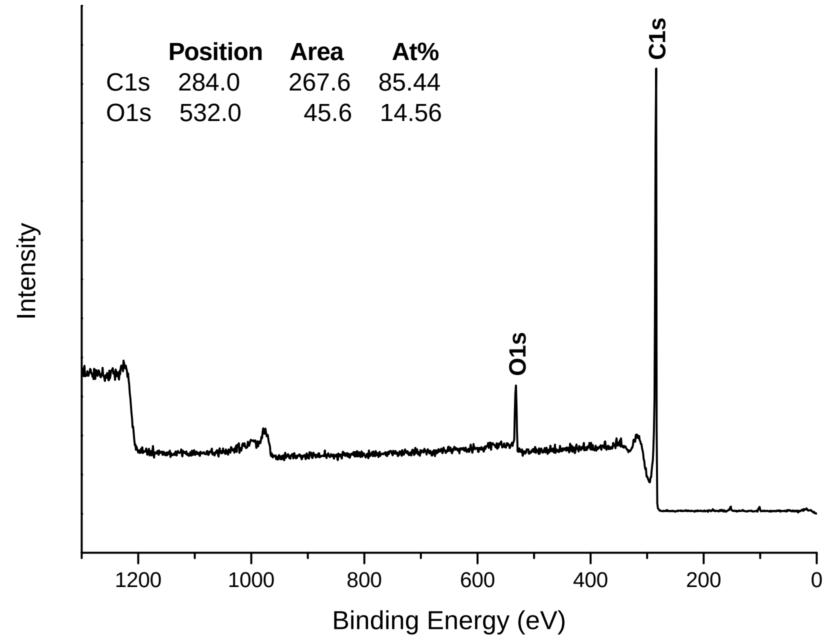

Figure 4.23: XPS analysis of a sample scratched with diamond and heated for 2 days in air at 200 °C.

The heating treatment in general increased the percentage of surface covered, see for example samples n9 (pristine graphite) vs n13 (graphite heated for 2 days) and n3 (scratched with diamond) vs n19(scratched with diamond and heated for 2 days). However, when hydrogen plasma etching was included after heating (sample n12), the surface coverage was lower than the sample without heating (n6). It may be that the oxygenated surface reacted faster with hydrogen producing the surface erosion. It was seen in optical emission analysis that after 10 min deposition CH species in this sample were increased (Table 4.6). On the other hand, if the sample was heated in nitrogen (sample n24) and then treated with hydrogen plasma the surface covered was higher than the sample heated in air (n12) but lower than the sample without heating (n6). This suggested that the functional groups absorbed on the surface reacted in different ways with hydrogen, otherwise samples n12 and n24 would have the same surface coverage, although they did have similar film morphology. Sample n23 which was heated in nitrogen but scratched with diamond had a completely different morphology than the rest of the samples and one of the greatest surface coverage.

In the case of samples n10 (silicon interlayer) and n11 (scratched with diamond + Titanium), both had different morphology than their analogous samples n1 and n5: this could have happened mainly because of the change in power. However the increase in surface coverage of sample n11 compared with sample n5 may be due to the heating treatment.

The quality of the films is also influenced by nucleation pretreatments and deposition power. The samples that were produced at 3.6 kW had the highest sp^3/sp^2 value (n20 and n21) followed by sample n15 that was produced at 3 kW power (see Table 4.4). We could also notice that the diamond peak position changed in each sample, which could be due to pressure in the films as had been reported by Sharma et al. [163]. They stated that it is possible to interpret the small wave number shifts as internal stresses in the films produced by thermal expansion between diamond film and substrate caused as the system is cooled to room temperature. The negative shifts are interpreted as films in tension and the positive shifts as films in compression. The G peak position also shifts to higher frequencies as a result of the higher sp^2 content [164]. This behaviour has been related to a critical value where the transition of the diamond to graphite begins to take place [165, 166].

Other features in Raman spectra that are worth mentioning are: 1) the diamond line intensity (Figures 4.12 and 4.13) which is known to decrease with the deterioration in crystal structure [153, 154], and 2) the presence of the broad bands at about 1500-1540 and 1325-1355 cm^{-1}, that are typical of faceted crystals with growth dislocations. When these crystals become more rounded and even ball-like, a third broad band can be seen at 1470 cm^{-1}.

XPS analysis is more sensitive to the surface than Raman so it was expected that the diamond signal would be higher since little contribution from the substrate is added to the spectra. Deconvolution of sample spectra (Table 4.5) showed that most of the films contained oxygen-carbon compounds in their surfaces and silicon carbide. The sample with the highest sp^3 content was the one deposited on a pristine substrate. This suggests that pretreatments may introduce impurities that can form defective diamond phases and dangling bonds which rapidly form oxides in contact with air. It is also interesting that the sample with the silicon interlayer did not have oxygenated carbon groups in the surface or at least not detected by the XPS. This is unexpected, knowing that silicon reacts easily with air to form silicon oxide and that the initial surface would be high in oxygen. However, this film had more saturated carbon bonds (sp^3/sp^2 content) that could be more stable when exposed to air. The presence of silicon carbide is also interesting: it is a common contaminant in all the samples except sample n6 (plasma etching). It is possible that the silicon is transferred from the quartz chamber, (for latest XPS results and more information about silicon contamination in diamond films, see Appendix A).

Optical emission spectroscopy showed mainly emission from C_2 and CH. The intensity of these emission peaks is directly related to the absolute concentration of the species in the plasma [167]. But even if C_2 peaks were intense it has been demonstrated here that this is not a major diamond growth species [52]. The analyses showed that the CH/C_2 ratio was higher at the beginning of deposition in almost all the samples, which could be due to graphite etching, see for example sample n12 in Table 4.6. The electron temperature (T_e) remained almost constant during deposition. It seems that there is no relation between T_e and the excitation power used during depositions, or between T_e and CH/C_2 ratio except for low ratios (see Figure 4.24). However, even if we were using the same gas mixture for all the samples, the electron temperature varies from one to another. We believe that the electron temperature depends on the species/chemistry in the plasma which varies for each sample due to the differences in erosion rate that depend on film quality and substrate coverage.

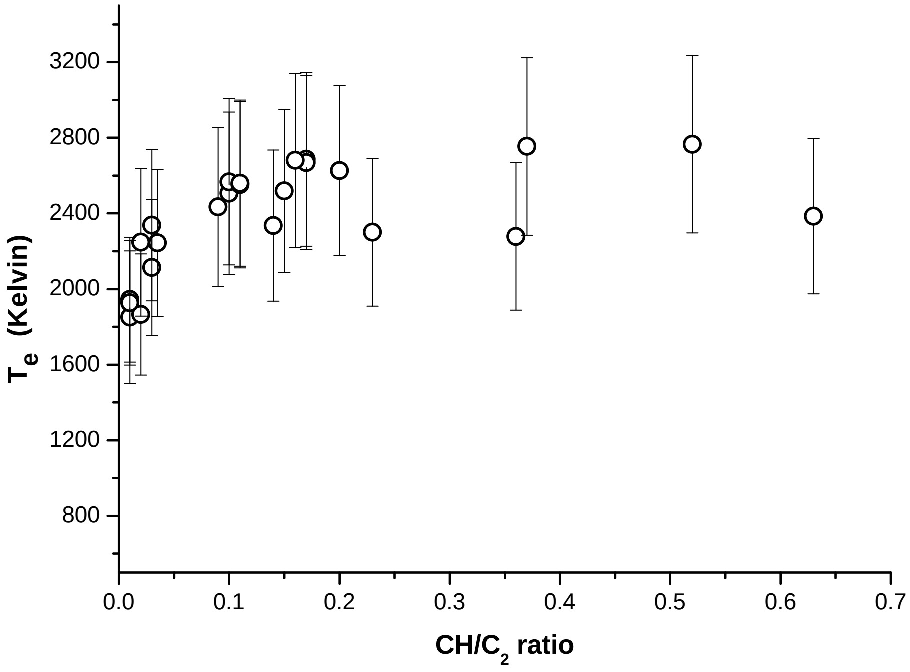

Figure 4.24: Optical emission T_e versus CH/C_2 ratio.

4.4 Conclusions

Nanocrystalline and Microcrystalline diamond films were deposited on graphite substrates that were treated using different techniques before deposition. We found that most of the pretreatments carried out, including heating in air and nitrogen, not only enhanced diamond nucleation density but also influenced the final morphology of the films. Nucleation pretreatments by manual scratching with diamond, scratching with nanodiamond, and ion bombardment decreased the nucleation density compared with the deposit on pristine graphite.

The excitation power used during deposition had a big effect on the diamond crystallite size. Microcrystalline films were obtained when the excitation power was 3.0 and 3.6 kW and nanodiamond films were observed when 1.5 kW was used, independently of the pretreatment. However, it seems that the film morphology at higher powers is completely dependent on substrate pretreatment.

Heating the substrates after nucleation pretreatments increased nucleation density in most of the cases. Heating the substrate before hydrogen plasma etching (sample n12) does reduce nuclei formation compared with the sample that was only heated and then coated (n13). In general, hydrogen plasma etching is a good pretreatment for graphite substrates because it avoids the use of diamond seeds or other materials that can introduce impurities during pretreatment.

If a microcrystalline diamond film on graphite substrate is desired, the best pretreatment is to sonically scratch the substrate with diamond, heat in air for 2 days at 200 °C and use 3.0 or 3.6 kW excitation power during deposition. This results in a greater area covered and a high diamond quality (sp^3/sp^2).

Finally, the morphology of diamond films prepared by microwave CVD is a consequence of several factors including nucleation pretreatment and excitation power. This has to be taken into account when choosing experimental conditions for the desired final texture.

Chapter 5

Effect of gas composition on the resulting morphology of CVD diamond films

5.1 Introduction

During microwave CVD diamond growth there are several experimental parameters that affect the resulting films. These are mainly the temperature, pressure, microwave power and gas composition.

Since the beginning of synthetic diamond production by CVD many gas mixtures have been used: the most common contain carbon-hydrogen and carbon-hydrogen-oxygen but mixtures of carbon-hydrogen with halogens and with noble gases have been used for specific applications.

In 1991 Bachmann and coworkers [168] produced a C-H-O diagram with the information available at that time and some experimental results obtained by them. The diagram contains three regions, 1) successful diamond growth, 2) non-diamond carbon growth and 3) no growth, these are shown in Figure 5.1.

The diamond domain has a lens-like shape which is situated close to the CO-H_2 tie-line. In the diagram, non-diamond carbon can grow at 0% hydrogen and no carbon deposits are produced at high oxygen fractions. Although under specific conditions several experiments have contradicted the C-O-H diagram [72, 170–172] this is still a good reference when choosing starting conditions.

The correct mixture of gases not only allows the growth of diamond on a specific substrate, but using an appropriate carbon content can give full control of the resulting film morphology. Kobashi et al. [173, 174] reported that the dominant morphology of polycrystalline diamond films on Si deposited by MPECVD showed triangular {111}

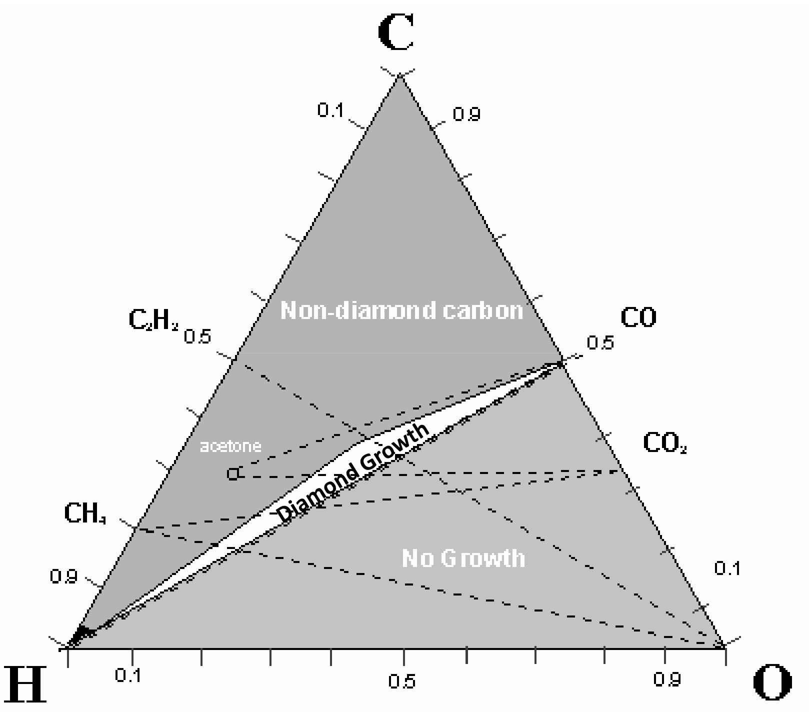

Figure 5.1: Bachmann diagram [169].

facets when the growth used $CH_4/H_2 < 0.4\%$. Square {100} facets were dominant when a gas mixture of $0.5\% < CH_4/H_2 < 1.2\%$ was used. Microcrystallites with no clear faceting are found for CH_4/H_2 ratios above 1.5%. It is known as well that increasing the CH_4/H_2 ratio, decreases the quality of the deposited diamond.

Homoepitaxial diamond films are also affected by changes in CH_4 concentration. Brinza et al. [175] observed that using 4% CH_4 the [100] orientation was predominant. Using 6 or 7.2% CH_4 the {110} faces appeared and the {113} faces became larger.

For nanocrystalline diamond films the increase of CH_4 concentration increases the stress in the film, as well as defect concentration and non-diamond phases (TPA and graphite) [152, 165].

The control of the film's morphology is important because it is strongly related to electronic and optical properties, thermal conductivity, strength, fracture toughness and residual stresses.

In this chapter we present the results obtained from the deposition of diamond on graphite using different $CH_4/H_2/Ar$ ratios. The main objectives of these experiments were:

1) to find the appropriate gas mixture for growing microcrystalline diamond on graphite;

2) to prove that by varying the methane and argon concentrations we can control the morphology of the film;

3) to study the changes in the morphology after prolonged deposition periods.

Table 5.1: Experimental conditions for samples c1 to c8 deposited using different gas mixtures.

	First 30 min	**Remaining 90 min of deposition**				
Sample	**5%CH_4/15%H_2/Ar**	**%CH_4**	**%H_2**	**%Ar**	**Pressure (torr)**	**Power (kW)**
c1	No	2.5	97.5	—	60	1.8
c2	No	5	95	—	60	1.8
c3	Yes	1	99	—	100	3.0
c4	Yes	3	97	—	100	3.0
c5	Yes	0.5	15	84.5	100	3.0
c6	Yes	1	15	84	100	3.0
c7	Yes	3	15	82	100	3.0
c8	Yes	5	15	80	100	3.0

To achieve this, we considered the use of high microwave power which allows increasing the methane concentration without compromising the quality of the film and the use of high methane concentration in the first 30 min of deposition to increase the nucleation density.

5.2 Experimental

Graphite substrates were pre-treated using ultrasonic scratching with diamond and methanol slurry for 30 min (as described in Chapter 4, this pretreatment gives optimum nucleation conditions). Then the samples were heated at 200 °C in a box oven at atmospheric conditions for two days and loaded in the growth chamber. Different mixtures of CH_4/H_2/Ar were used, as listed in Table 5.1. For samples c1 and c2 the microwave power used was 1.8 kW and for the rest of the samples 3 kW was used. Deposition time was two hours for all the samples and the chamber pressure was kept at 100 torr during the experiment except where noted.

Sample characterisation used Raman Spectroscopy, SEM, Mass Spectroscopy and Optical Emission Spectroscopy, with the experimental parameters described in Chapter 2.

Samples c5 to c8 were loaded into the chamber for a second and third deposition for periods of 4 hours each using the same experimental conditions as in previous experiments and detailed in Table 5.1 (100 torr, 3 kW power and methane concentration varying from 0.5 to 5%). We will call these samples tc5, tc6, tc7 and tc8.

5.3 Results

5.3.1 SEM analysis

During SEM analysis we found that samples c1 and c2 were badly etched after CVD conditions and no evidence of diamond growth was seen. As an example Figure 5.2(a) shows sample c1 and 5.2(b) sample c2, where some diamond seeds from the nucleation treatment can be seen on top of the etched graphite surface.

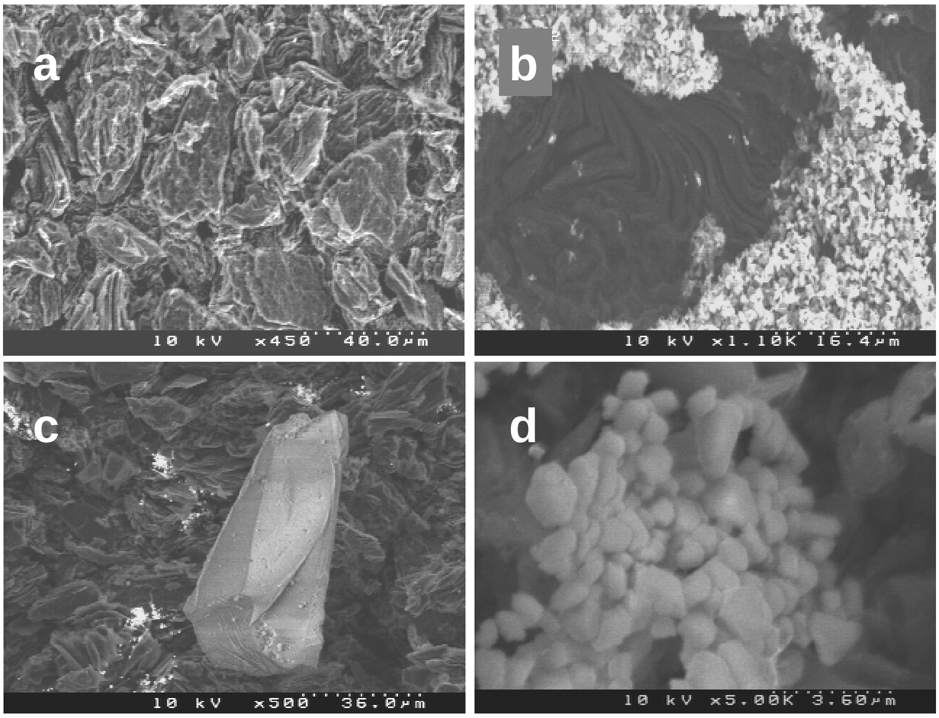

Figure 5.2: SEM micrograph from samples c1 to c4 treated with methane/hydrogen mixture. (a) correspond to sample c1 (2.5%CH_4/H_2), (b) sample c2 (5%CH_4/H_2), (c) sample c3 (1%CH_4/H_2) and (d) sample c4 (3%CH_4/H_2).

Figure 5.2(c) shows a micrograph from sample c3 having a large crystal (72 μm long) without any particular shape. During deposition, sample c4 had slow diamond growth mainly on the diamond seeds. In Figure 5.2(d) we can still see the seed shapes but {100} planes can also be distinguished.

Figure 5.3(e) and (f) show micrographs taken from different areas of sample c5, (e) is from the centre of the sample and presents some rectangular crystals of approximately 4.5 x 1.5 μm. Figure 5.3(f) shows the surface close to the edge of the graphite substrate where square crystals of ~2.4 μm with {100} faces can be found.

Micrographs in Figure 5.3(g) and (h) correspond to the centre and near the edge of sample c6, respectively. This sample also has crystals with {100} faces of ~1 μm side.

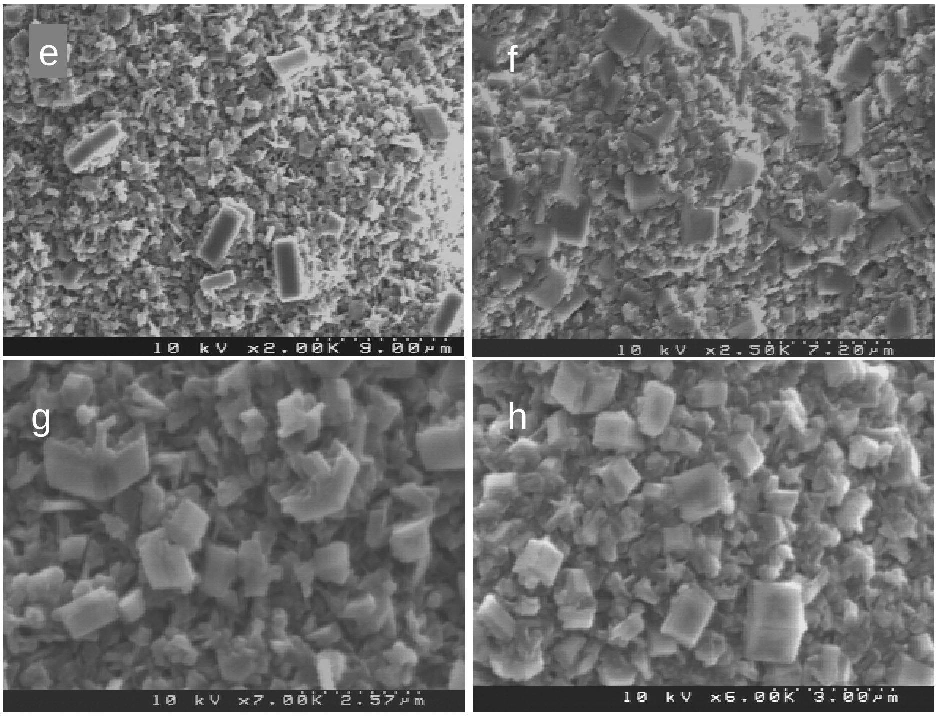

Figure 5.3: SEM micrograph from samples c5 (e,f) and c6 (g,h) prepared with a mixture of 0.5 and 1% CH_4, respectively.

When the methane concentration was increased from 1 to 3 and 5%, {111} faces appeared. Such is the case of sample c7 (Figure 5.4(i) and (j)) and sample c8 (Figure 5.4(k) and (m)). In both samples we can see crystals with a mixture of {100} and {111} faces. However, sample c8 has in general bigger crystals: see for example (j) and (m) that were taken from near to the edges. We could also find in sample c8 some single crystals (15 μm) with cubo-octahedral shape.

SEM results from samples tc5 and tc6 after the second and third depositions are shown in Figure 5.5. Sample tc5 has crystals in two different growing directions: [111] in the centre of the samples which gave {100} faces (micrograph (n)) and [100] close to the edges which gave {111} faces (micrograph (o)). Sample tc6 shows crystals with planes in the [100] directions at both centre and edges of the sample (micrographs (p) and (q), respectively).

As can be seen in Figure 5.6, sample tc7 presents crystals in the [100] direction over all the surface, both near to the edge (r) and in the centre (s). However the crystals in the edges are rectangular (around 12 x 6 μm) and have picture frame-like shape and the crystals in the centre are mainly square ($\sim$9 μm^2). Sample tc8 however has a cauliflower-like surface typical of nanocrystalline diamond.

The analysis of the cross section in samples tc5 to tc8 showed renucleation in the grown diamond films. As an example Figure 5.7 shows a micrograph from sample tc8. Table 5.2 contains the average diamond film growth rate for these samples.

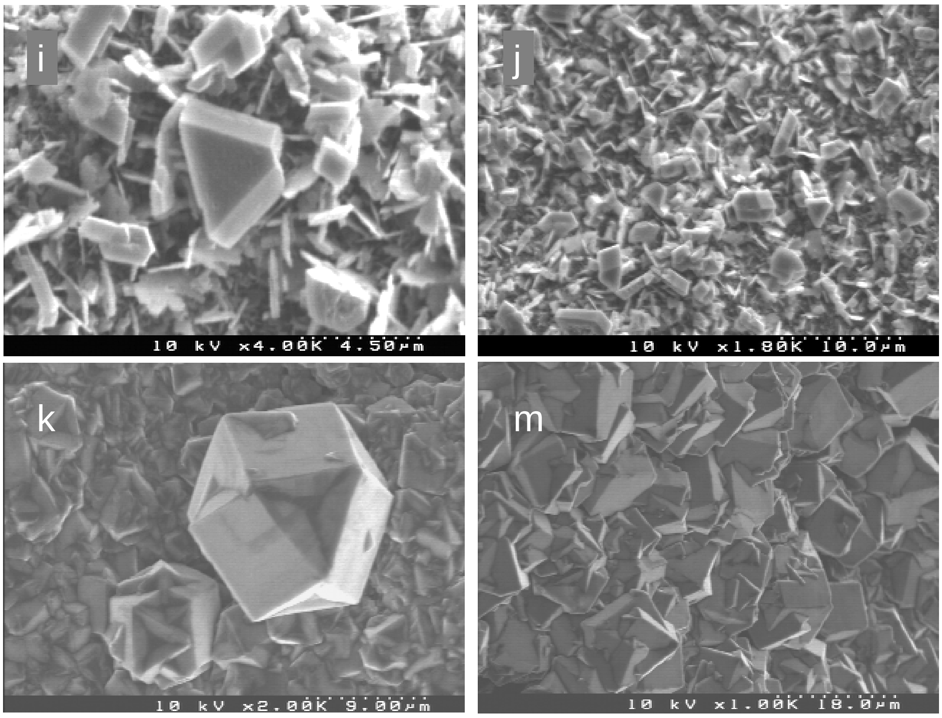

Figure 5.4: SEM micrograph from sample c7 (i,j) and c8 (k,m) prepared with a mixture of 3 and 5% CH_4, respectively.

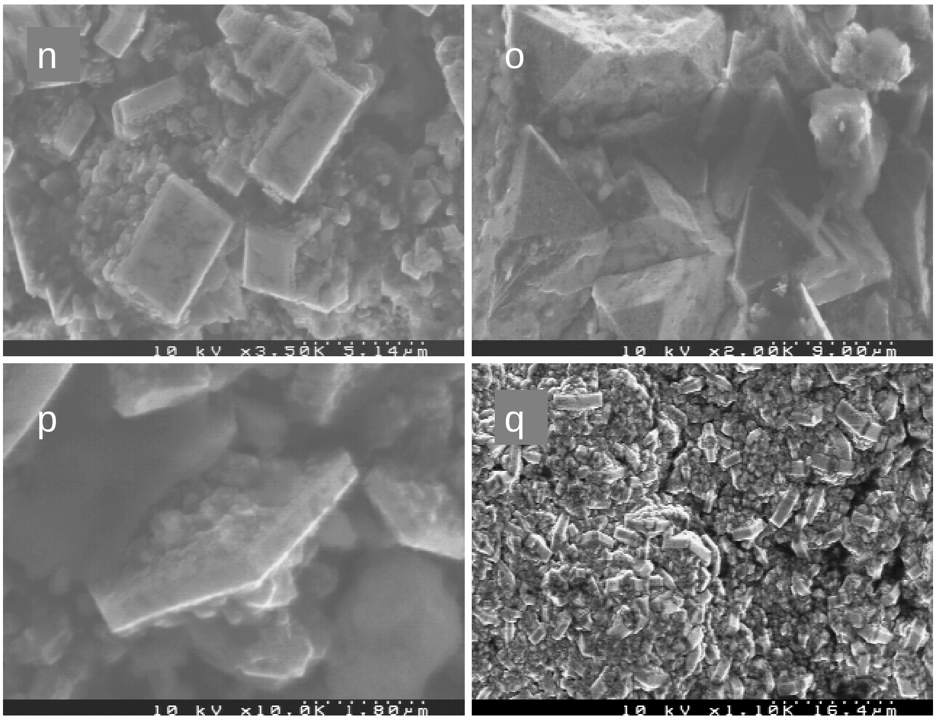

Figure 5.5: SEM micrograph from sample tc5 (n,o) and tc6 (p,q) which were deposited for further 8 hours with a mixture of 0.5 and 1% CH_4.

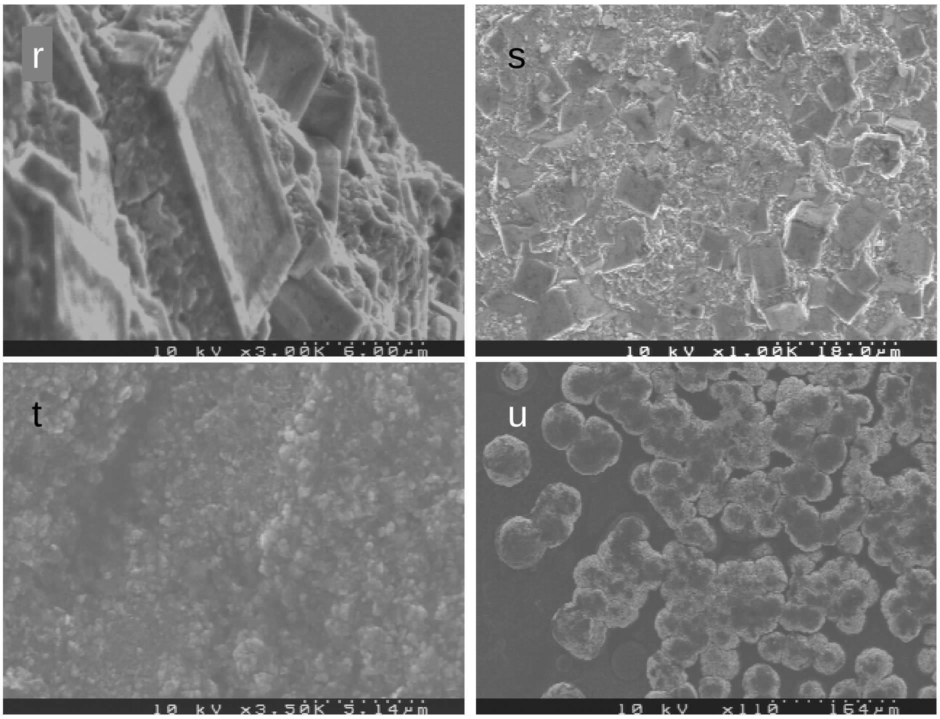

Figure 5.6: SEM micrograph from sample tc7 (r,s) and tc8 (t,u) after 10 hours deposition.

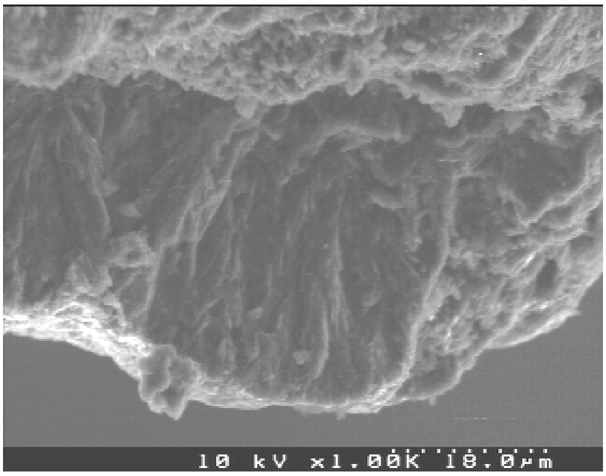

Figure 5.7: Cross section of sample tc8.

Table 5.2: Growth rates of samples deposited using mixtures of $CH_4/H_2/Ar$.

Sample	**Growth rate** (μm/hr)
tc5	2.4
tc6	2.4
tc7	4.8
tc8	3.3

5.3.2 Raman analysis

Figure 5.8 shows the Raman analyses for samples c3 to c8. The results for samples c1 and c2 are not presented here since no diamond was deposited on the substrates. The spectra from samples c3 and c4 only have contributions from graphite at 1350 and 1580 cm^{-1}, corresponding to D- and G-bands. The spectra from samples c5 to c8 clearly show diamond (1332 cm^{-1}), graphite and amorphous carbon bands. Samples c6 and c7 also show a peak at $\sim$ 1130 cm^{-1} corresponding to nanodiamond or transpolyacetylene [158] although the latter is not yet commonly accepted.

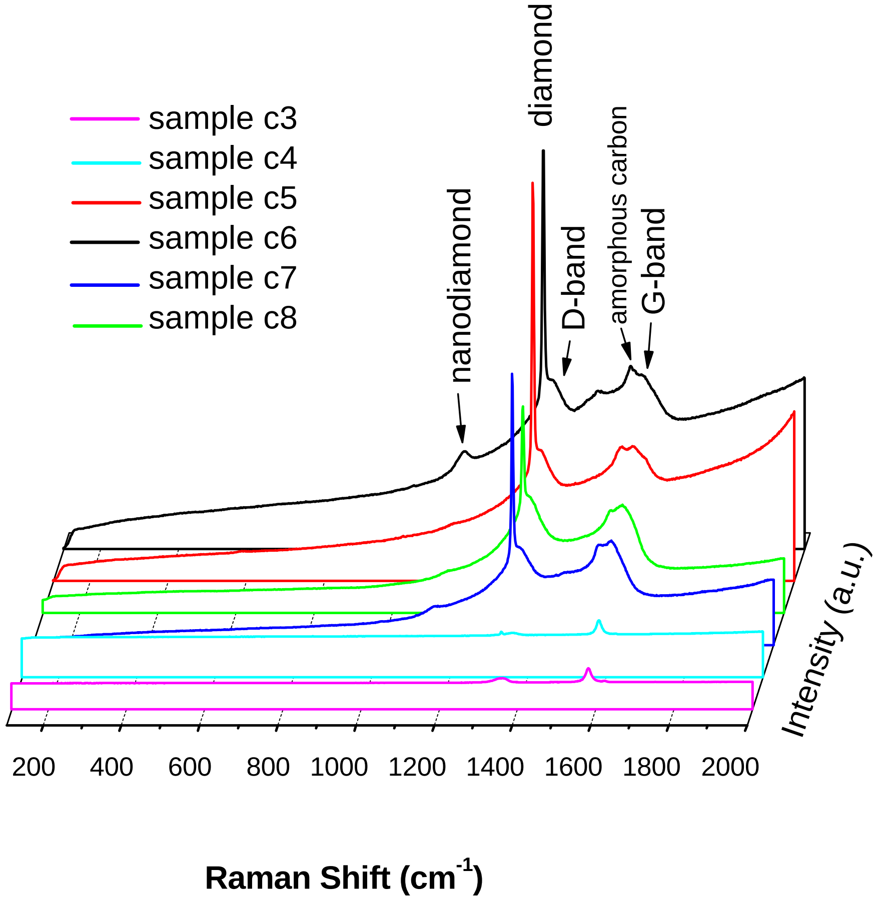

Figure 5.8: Raman spectra of all samples

Table 5.3 contains the results from the deconvolution of the Raman spectra of samples c5 to c8. The FWHM are in accordance with the reported 2-14 cm^{-1} for CVD diamond. The sp^3/sp^2 ratio is also shown in the table, however since the scattering efficiency of sp^2 bonded carbon greatly exceeds that of sp^3 bonded (crystalline graphite has a scattering efficiency $\sim$50 times greater than of single crystal diamond [176]) the sp^3/sp^2 ratio could be higher than that shown in the table.

Figure 5.9 contains the Raman analyses for samples tc5 to tc8. Again contributions from diamond, graphite, amorphous carbon and nanodiamond can be seen in the spectra. Table 5.4 has the results from deconvolution of Raman spectra for samples tc5 to tc8. We can see that the FWHM values of samples c5 and c6 decrease after the second and third depositions (samples tc5 and tc6), but in the case of samples c7 and c8 the FWHM value increases (samples tc7 and tc8). It is well known that the FWHM is related to the disorder in the sp^3 bonding environment [177] but it could also be related to the decrease in diamond grain size which is also reflected in the sp^3/sp^2 ratio (see sp^3/sp^2 value for sample tc8). Samples tc5, tc6 and tc7 show higher sp^3/sp^2 ratio than c5, c6 and c7 which could be due simply to the higher thickness of these samples which avoids acquiring data from the substrate. However, the sp^3/sp^2 ratio considerably decreases in sample tc8, and gives a value comparable with the nanodiamond films prepared in Chapter 4. We could also notice that there is a shift in the diamond peak position of samples tc5 to tc8 compared with samples c5 to c8, that can be related to stress effect.

Table 5.3: Parameters from deconvoluted Raman spectra for samples c5 to c8.

	Diamond (sp^3)		**Graphite (sp^2)**		
Sample	**Peak** (cm^{-1})	**FWHM** (cm^{-1})	**Peak** (cm^{-1})	**FWHM** (cm^{-1})	**sp^3/sp^2**
c5	1332.8 ±0.01	5.0 ±0.01	1592.0 ±0.8	63.6 ±2.8	0.82±0.1
c6	1332.9 ±0.01	5.5 ±0.02	1575.4 ±1.2	88.7 ±2.4	0.25±0.01
c7	1333.0 ±0.01	4.5 ±0.02	1587.4 ±0.4	60.4 ±1.2	0.35±0.02
c8	1332.6 ±0.01	5.6 ±0.01	1593.5 ±0.2	60.0 ±0.8	0.22±0.01

Table 5.4: Parameters from deconvoluted Raman spectra for samples tc5 to tc8.

	Diamond (sp^3)		**Graphite (sp^2)**		
Sample	**Peak** (cm^{-1})	**FWHM** (cm^{-1})	**Peak** (cm^{-1})	**FWHM** (cm^{-1})	**sp^3/sp^2**
tc5	1332.0 ±0.01	4.9 ±0.02	1593.9 ±0.4	44.0 ±1.2	1.02 ±0.05
tc6	1331.8 ±0.02	4.9 ±0.04	1590.4 ±0.3	47.1 ±1.0	0.26 ±0.01
tc7	1332.6 ±0.02	6.0 ±0.04	1589.5 ±0.6	63.6 ±1.9	0.25 ±0.02
tc8	1331.9 ±0.05	5.9 ±0.12	1586.1 ±0.4	57.5 ±1.2	0.07 ±0.01

5.3.3 Mass Spectroscopy

Figure 5.10 shows the mass spectra taken from the gas mixture before igniting the plasma. The difference in the signal of each species is clear when using different methane contents. However, the H_2 signal remains constant and the ratio of CH_3/CH_4 signals is 0.85 ±0.02 for all samples.

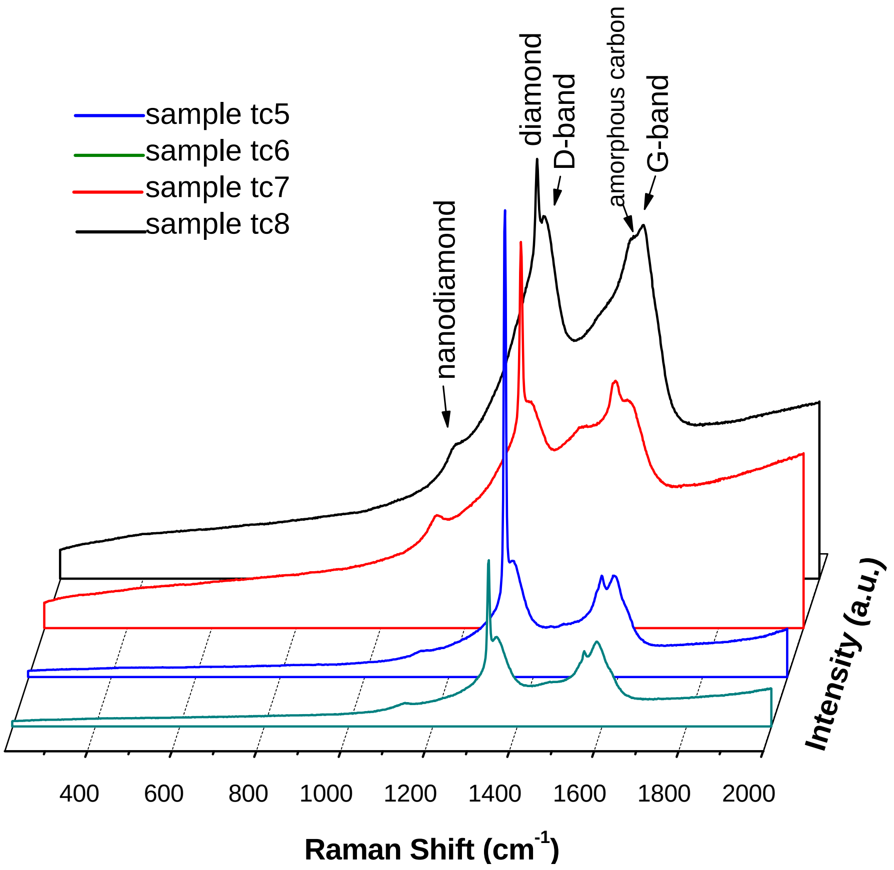

Figure 5.9: Raman of samples tc5 to tc8.

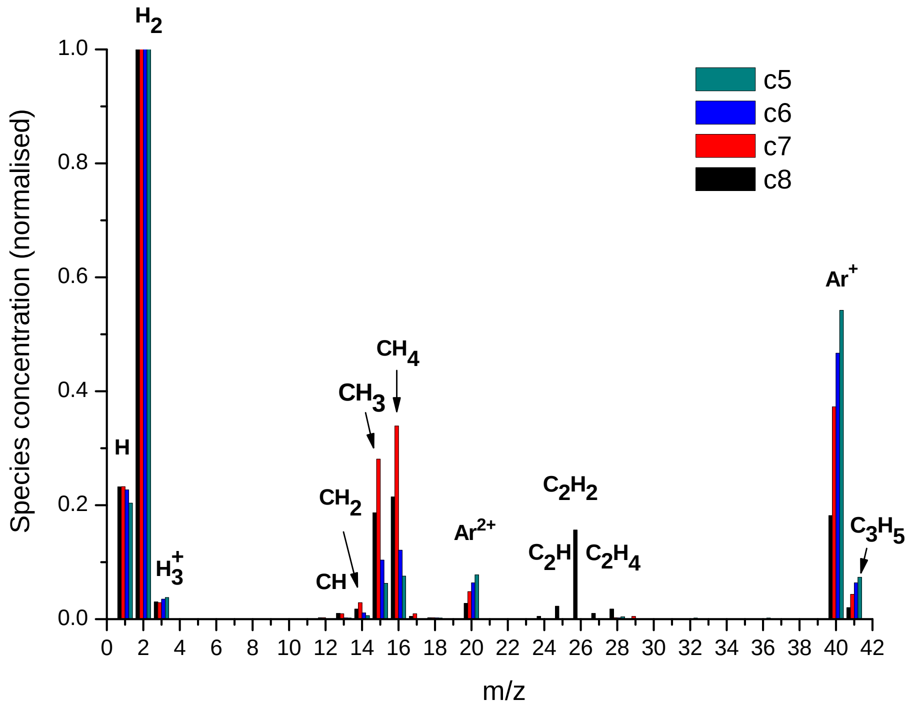

Figure 5.10: Mass spectra from samples c5 to c8 before ignition of the plasma.

Table 5.5 shows the mean values for the ratio of detected carbon species/methane. In general samples c5 and c6 present lower or zero values in most of the analyses. However the CH_3/CH_4 ratio is higher for these samples than for c7 and c8. It is also notable that sample c5 has higher mean value of CH_2/CH_4 ratio than the rest of the samples.

Table 5.5: Mean values for the ratio of *carbon species*/m, where *carbon species* = CH, CH_2, CH_3, C_2, C_2H, C_2H_2, C_2H_3 and C_2H_4 and m = methane, for sample c5 to c8.

Sample	CH/m	CH_2/m	CH_3/m	C_2/m	C_2H/m	C_2H_2/m	C_2H_3/m	C_2H_4/m
c5	0	0.12	0.94	0	0	0.01	0.01	0.02
c6	0	0.01	0.93	0	0	0.26	0.01	0.11
c7	0.03	0.06	0.92	0	0.09	0.82	0.09	0.18
c8	0.03	0.07	0.91	0.01	0.1	0.75	0.09	0.16

5.3.4 Optical Emission analysis

Figure 5.11 shows typical optical emission spectra from samples c3 to c8. The signals detected are mainly from the C_2 Swan band at 471, 516, 553, 557 and 562 nm; and the Balmer series at 656.6 and 485 nm from H_α and H_β. The band at 587 nm corresponds to H_2, 388 and 430 nm are from the CH species and 403 nm is a contribution from the C_3 species.

Figure 5.12 contains a graph with the CH/C_2 ratio vs time for samples c5 to c8. We can see that the CH/C_2 ratio has a similar value for all the samples at the beginning of the reaction. After 2 hours of deposition the ratio increases for samples c5 and c6 while it decreases for samples c7 and c8.

5.4 Discussion

The fact that no diamond growth was seen in samples c1 and c2 must be related to the interactions of argon and hydrogen with the substrate surface. The presence of argon avoids the formation of a hydrogen-rich layer in the substrate surface which is responsible for chemical sputtering: this has been explained in detail by Schwarz-Selinger et al. [203]. The few crystals seen in samples c3 and c4 must be formed during the first 30 min of deposition when the gas mixture had argon. It is possible that the crystals continued growing after changing the mixture to CH_4/H_2.

SEM micrographs from samples c5 to c8 after two hours of deposition (Figure 5.3 and 5.4) confirm the growth of uniform microcrystalline diamond films on graphite

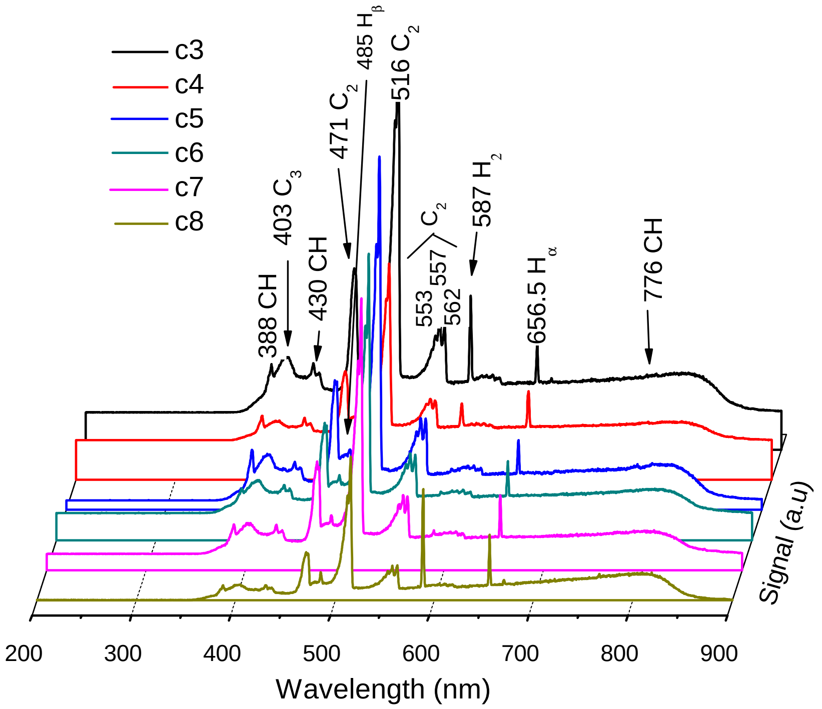

Figure 5.11: Typical optical emission spectra from samples c3 to c8, taken after 10 min of deposition.

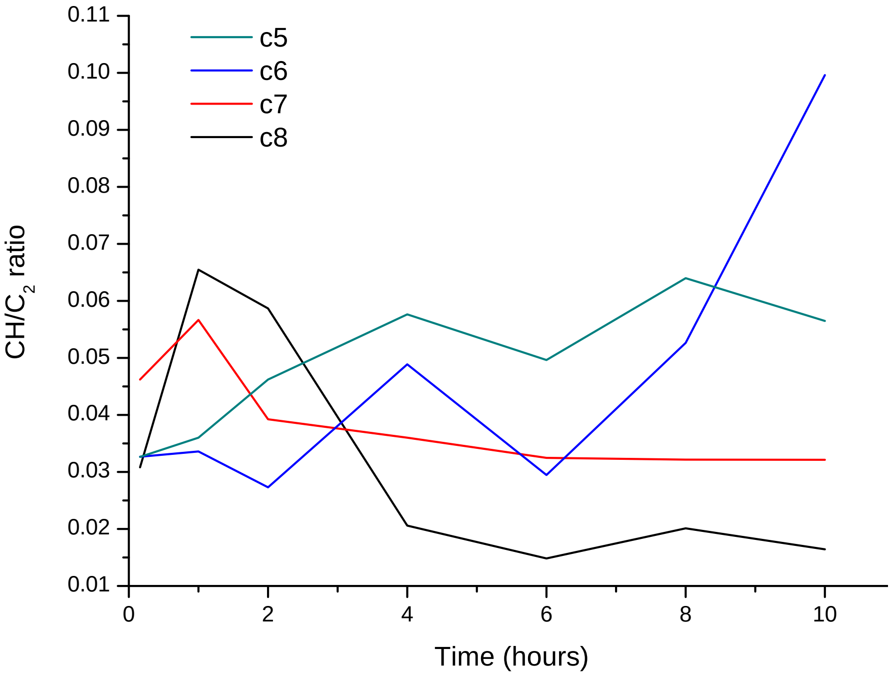

Figure 5.12: CH/C_2 ratio vs deposition time obtained by optical emission analysis.

in the presence of argon. The change in the morphology is clear for the different methane concentrations, however the common crystal orientations are [100] and [111] in all the samples. The growth direction for films presenting {100} faces is [111] and for films presenting {111} faces is [100]. That is, the slowest growth direction will determine the final crystal orientation. Cubo-octahedron crystals shown by sample c8 correspond to an alpha parameter of 1.5 (growth rate in the [100] direction (V[100]) over growth rate in the [111] direction (V[111]) is equal to 0.87) where the growth direction is [110].

The α parameter defined as:

$$\alpha = \sqrt{3}\frac{V_{[100]}}{V_{[111]}} \tag{5.1}$$

has the value 1.0 for cubic crystals and 2.85 for octahedral crystals. It depends on methane concentration [178] and increases when methane increases. Our results show that sample tc5 is the only one presenting {111} faces near to the edges of the substrate, contrary to what would be expected for the sample with the lowest methane concentration. This can be explained by two factors: 1) concentration gradient of the various species away from centre of plasma and 2) temperature gradient. It is known that temperature considerably affects diamond film morphology. Chu et al. [179] reported that under fixed methane content the growth rate ratio V[100]/V[111] increases when the temperature decreases. We know that there are concentration and temperature gradients across the substrate surface since we commonly see different textures between the centre and edges of the substrate.

Secondary nucleation effects were seen in all samples. However it was more obvious in sample tc8 that after 10 hours of deposition, it presented a cauliflower-like morphology typical of nanocrystalline diamond films. Vikharev et al. [180] reported a change in the morphology when changing the methane content in CH_4-H_2-Ar mixtures and a change in the crystal size (from microcrystalline to nanocrystalline) when increasing the argon content in the same CH_4-H_2-Ar mixtures.

The growth rate and the quality of diamond films are strongly affected by the methane concentration. Working with a hot filament CVD system, Inspektor et al. [41, 181] found that the maximum growth rate was achieved when the gas mixture contained 3% CH_4 and that it decreased when the CH_4 concentration was higher. Having this in mind it is not surprising that sample c7 has a higher growth rate than sample c8 (Table 5.2). Raman analysis of our samples showed that the quality of diamond films decreases as the methane concentration increases (see values sp^3/sp^2 in Tables 5.3, 5.4).

To make a correct interpretation of our mass spectroscopy results we have to assume the following considerations:

1) The resulting morphology of the films depends mainly on the reacting species and those depend on the gas mixture (methane and argon content) as has been previously discussed by Zhu et al.[182] and Wild et al. [183] among others.
2) The temperature and temperature gradient are the same for different substrates, so we can compare similar substrate locations (e.g. centre or edges) in the different samples.
3) The change in temperature due to the use of different gas mixtures has a minimal effect on the resulting texture.

If the above mentioned are true, we can relate the presence of specific species in the plasma with the resulting textures. It is widely accepted that for {100} surface the (2x1):1H reconstructed surface is the most stable. Furthermore, the growth mechanism for {100} surface must be that proposed by Garrison et al. [60] or a variation of this. The mechanism involves a methyl radical or one-carbon species (such as CH_3, CH_2 or C) as the growing species. In our experimental conditions when methane concentration is low the content of one carbon species is high: this should facilitate the mechanism proposed by Garrison and the formation of {100} faces.

The {111} surface is highly defective [184] and rough on an atomic scale [185]. The carbon addition may occur locally at sites with {100} or {110} character. This will explain the presence of both {100} and {111} faces in samples tc5 and c8.

C_2H_x species in the plasma phase during deposition of samples tc7 and tc8 must be related to the production of nanocrystalline diamond as has been stated in recent publications [58, 82]. These observed that in the presence of C_2H_x, C_3H_x and even C_4H_x species together with CH_x radicals, nanocrystalline diamond was formed. Our optical emission results agree with the mass spectroscopy analysis since there is a decrease of the CH/C_2 ratio at high methane concentration.

5.5 Conclusions

An important deduction is that argon is essential in the gas mixture for growing diamond on graphite. The morphology, the good quality and the crystal size of the films depend on the methane content used during deposition. When using less than 5% of methane in the gas mixture, {100} faces are predominant even after long periods of deposition. Using 5% of methane results in a film with cauliflower-like structure. The change in the morphology when depositing for longer periods of time is caused mainly by secondary nucleation. The analysis of the films' cross-sections showed renucleation during diamond growth. The growth rate also depends on the methane concentration, increasing until a certain point from where it decreases. The sp^3/sp^2

content which is an indicator of the quality of diamond films increased when the methane content decreased. Mass spectrometry analysis showed that 0.5% methane mixture had higher content of CH_3 and CH_2 species than mixtures containing 3 and 5% methane. Furthermore, mixtures with 3 and 5% of methane had higher content of two-carbon species. The presence of one-carbon species in the reaction mixture can be related to the resulting morphology considering the mechanism proposed by Garrison [60]. The presence of two-carbon species can be related to the production of nanocrystalline diamond as has been seen by Zhou et al. [82] and May et al. [58]. The optical emission results suggested the increasing of CH species when decreasing the methane content.

Chapter 6

Hydrogen plasma etching of thick diamond films

6.1 Introduction

One of the main concerns about the use of carbon based materials in plasma facing components is the erosion due to hydrogen bombardment. This not only shortens the life of the material but also contaminates the plasma and the chamber with hydrocarbons and carbon dust. Other disadvantages of graphite components under fusion conditions are tritium retention, degradation of vacuum sealing, electrical isolation and formation of mixed-materials whose behaviour is still unknown [186].

Since 1976 there have been studies about erosion of graphite and amorphous hydrogenated carbon using hydrogen [187, 188]. Today it is well known that the chemical erosion of graphite by hydrogen results from three processes: 1) the thermally activated hydrocarbon emission, Y_{therm}, due to the chemical reaction between carbon and hydrogen; 2) the physical sputtering under energetic ion bombardment, Y_{phys}, which depends on the ion energy; and 3) the surface process at low ion energies and low temperatures resulting from the kinetic ejection of surface hydrocarbon complexes, Y_{surf}.

This last process, kinetic emission of hydrocarbons, has been observed at ion energies below the threshold of normal physical sputtering and low substrate temperatures where no chemical erosion is expected. Roth and Garcia-Rosales [189] explained that this kind of erosion may be caused by the sputtering of weakly bound sp^3 CH_x groups at the surface. Later, Hopf et al. [190] proposed another mechanism where the incident ions break bulk carbon bonds that can be passivated by atomic hydrogen that penetrates into the film. The result is the formation of stable hydrocarbon molecules which can diffuse to the surface and desorb by a thermally activated process.

The erosion process has been summarised in the following equation where the total sputtering yield is given by:

$$Y_{tot} = Y_{phys} + Y_{therm}(1 + DY_{phys}) + Y_{surf} \tag{6.1}$$

Where Y_{phys} is the physical sputtering; Y_{therm} is the thermal erosion; Y_{surf} represents the kinetic surface emission of hydrocarbons and explains the large isotope effect going from deuterium to hydrogen; and D is a constant that depends on the mass of the hydrogen isotope used.

Hydrogenation and erosion of amorphous carbon are closely related, as is shown in figure 6.1 [189, 191].

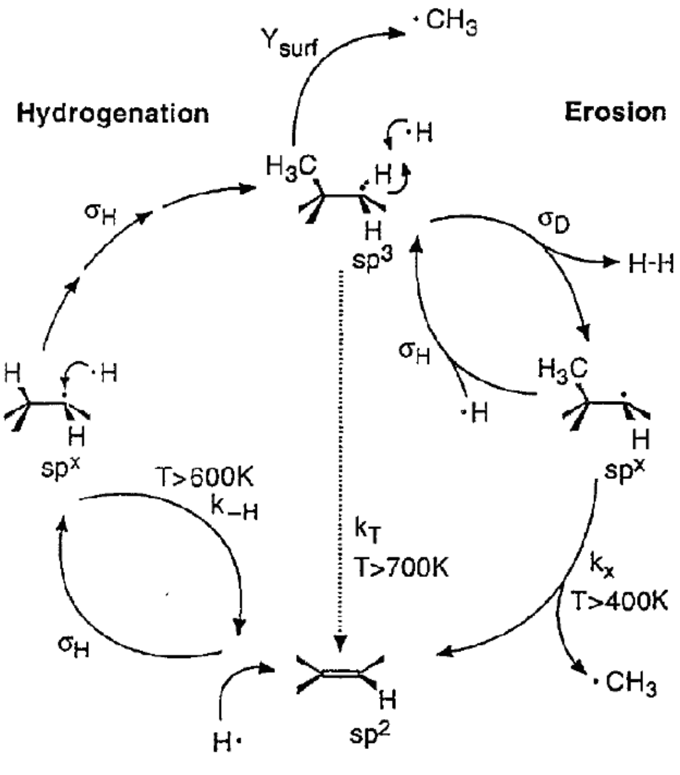

Figure 6.1: Schematic diagram of the reaction steps of the chemical erosion of a thin amorphous hydrogenated carbon layer (a-C:H) on platinum by atomic hydrogen [189].

In Figure 6.1 the hydrogenation process at temperatures below 600 K is proportional to a cross-section (σ_H) and it occurs when surface carbon atoms in sp^2 configuration are hydrogenised to sp^3 hydrocarbon complexes via an intermediate radical sp^x. Furthermore, atomic hydrogen can remove a hydrogen attached in the surface to produce a hydrogen molecule and leave a radical sp^x, with a cross section of (σ_D). σ_H is much larger than σ_D therefore the concentration of sp^3 is higher. At temperatures above 400 K the hydrocarbon complexes can desorb with a rate constant k_x and a double bond is produced leaving an sp^2 configuration. Subsequent hydrogen addition can produce the hydrogenated surface, on the other hand if the temperature is above 600 K, an sp^x radical can transform to an sp^2 configuration with a rate constant k$_H$. In the absence of hydrogen the erosion can only proceed above 700 K with a rate constant k$_T$.

The etching of amorphous hydrogenated carbon (a-C:H) with molecular hydrogen (H_2) has also been studied [192], revealing that the process is temperature dependent going through a maximum around 650-700 K and decreases again for higher temperatures. If H_2 is mixed with argon, a substantial chemical sputtering below 340 K can occur, which does not depend on temperature but on ion energy. Above 340 K the erosion rate depends again on temperature but it is higher than the erosion produced only with molecular hydrogen. Similar results of plasma erosion of graphite with mixtures of argon/atomic hydrogen were obtained by Takeguchi et al. [193].

Under exposure to hydrogen plasma, diamond converts to a structure very similar to a-C:H [194, 195] in which case the erosion would proceed under similar reactions shown in figure 6.1.

Diamond erosion has been widely studied as part of the CVD growing process in which both mechanisms are happening simultaneously. Butler and Woodin [196] reported a diamond growth model from gaseous species in which the surface carbon dangling bonds are stabilized by atomic hydrogen. The hydrogen may assist the incorporation of the hydrocarbon species which may form part of the diamond structure or may desorb by a thermal process producing defects.

Diamond surface studies [197, 198] showed that hydrogen plasma etching of [100] oriented facets produced flatter surfaces covered by monoatomic steps parallel to [110], which indicates dimer formation during etching [199]. This was confirmed by low energy electron diffraction, showing (2x1) reconstruction of the polished {100} faces [200, 201]. It was suggested that etching/regrowth processes may contribute to the observed morphologies generated by a hydrogen plasma treatment and that diffusion of hydrocarbon species on the surface plays a major role during diamond etching. The diffusion is maximized at substrate temperatures just slightly below the regime in which etching becomes significant [197, 198].

For diamond it has been seen that the maximum sputtering yield occurs in a temperature range 750-1120 K in contrast to $\sim$780 K for graphite. It has also been seen that diamond is etched from 75 to 7000 times more slowly than graphite by low energy H atoms [202].

Another important phenomenon occurring during the plasma-wall interactions in fusion conditions is the re-deposition of the etched carbon molecules. High energy ions such as helium and argon increase the sticking probability of CH_3 radicals on the surface [203], this has been calculated from the relationship between the increase in the growth rate and the presence of an ion flux. It was also seen that increasing the flux in plasma devices decreased the total erosion. The phenomenon has been attributed to either the increase of re-deposition with plasma density or the change of dissociation/excitation/transport properties of the hydrocarbons near the surface [204].

CVD diamond has also been irradiated with highly charged ions [205]. The results showed that the surface electrical properties depend on the absorbed species. In this way hydrogen terminated surfaces are highly conductive and oxygen terminated highly insulating. The irradiation with highly charged ions on gem diamond produced graphitic dots which increase proportional to the ion dose [205].

The erosion of diamond has not only fusion interest but it has also been used as a polishing technique. Controlled plasma experiments with hydrogen, hydrogen/nitrogen [206] and argon/oxygen [207] have decreased considerably the time to polish a diamond surface. Other interesting techniques such as dipping the film in $FeCl_3$ before plasma erosion have also been used [208].

This chapter is dedicated to the study of the hydrogen erosion of the prepared films. The results will give us an idea of how these films will behave under more extreme conditions. Today we know that nanocrystalline and polycrystalline diamond films can withstand fusion conditions as we have published in [209]. The in situ optical emission analysis together with the mass spectroscopy will also provide us with information about the erosion mechanism of our films.

6.2 Experimental

The samples used for these experiments are labelled tc5-tc8 from chapter 5. These samples were cut in half, cleaned with methanol and loaded into our 6 kW CVD system described in chapter 2. Two experiments were done under the same conditions. In the first run samples tc5 and tc6 were treated together having the cut edges touching each other in order to avoid etching of the graphite. The second run was for samples tc7 and tc8, and they were placed in the same way as previous samples. The resulting films are labelled etc5 to etc8. After loading the samples the chamber was evacuated to around 1 x 10^{-6} torr and then hydrogen was introduced to reach a pressure of 100 ±2 torr. The excitation power used during the experiment was 3 kW and the total exposure time was 30 min.

Sample characterisation used SEM, Raman Spectroscopy, Mass Spectroscopy and Optical Emission Spectroscopy with the experimental parameters described in Chapter 2. Mass Spectroscopy and Optical Emission results will be shown as qualitative analysis since comparable results for each sample were not obtained because two samples were etched at the same time.

6.3 Results

6.3.1 SEM analysis

Figure 6.2 shows SEM micrographs from samples tc5 (a,c) and etc5 (b,d). Before hydrogen plasma etching, sample tc5 presented squares and rectangular crystals with faces consisting of flat surfaces having large terraces, nano steps and pits over the whole area. This kind of surface has been seen in CVD diamond films grown homoepitaxially on [001] oriented substrates. After hydrogen plasma etching (b and d) many etch pits appeared on the surface. The etch pits had mainly a square shape. In micrograph (d) we can also see a series of steps with different shape, some of them have straight edges and some have zigzag edges. In the top left we can notice that the steps are arranged in a spiral.

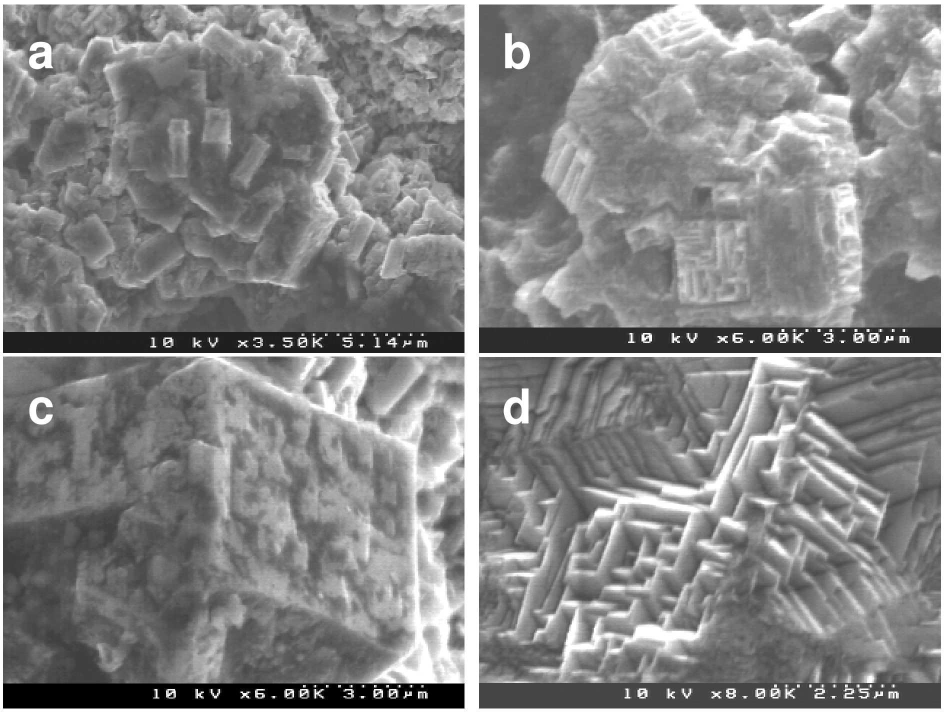

Figure 6.2: SEM micrographs from sample tc5 (a,c) and etc5 (b,d).

Figure 6.3 shows micrographs from samples tc6 (e,g) and etc6 (f,h). Sample tc6 consisted of different sized square crystals similar to sample tc5: after hydrogen etching square pits appeared in the big crystal faces. Some of the smaller crystals were etched away as seen in micrographs (g) and (h). For example, the small particles attached to the sides of the big central crystal disappeared in micrograph (h). Some other small crystals were very damaged but remained on the surface.

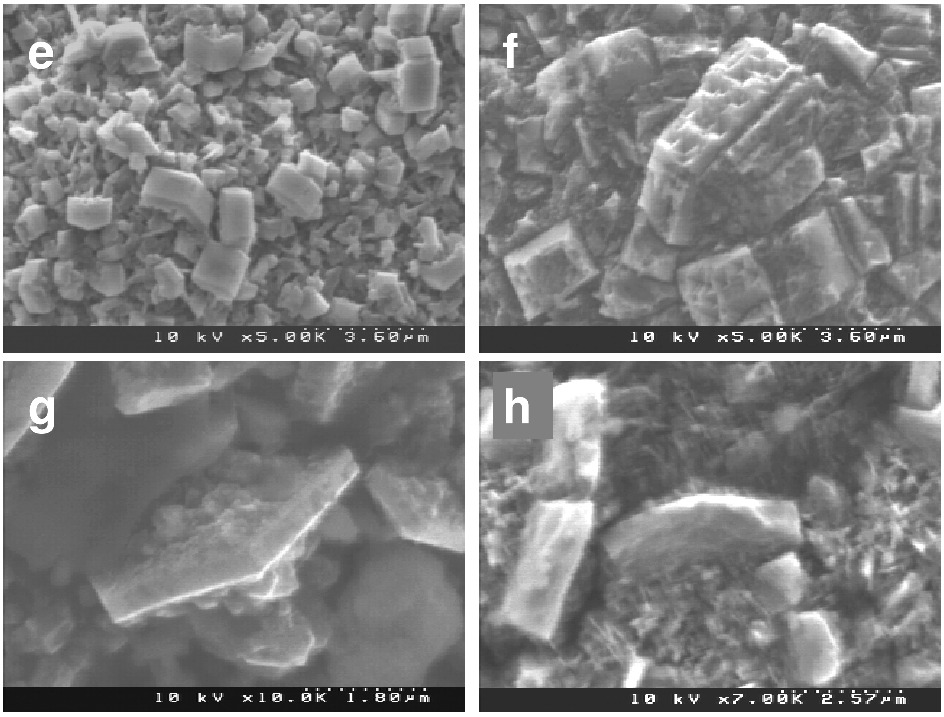

Figure 6.3: SEM micrograph from sample tc6 (e,g) and etc6 (f,h).

The surface of sample tc7 contained square and rectangular crystals, mainly in the [100] direction surrounded by smaller randomly oriented crystals (Figure 6.4(i)), after hydrogen etching these smaller crystals were strongly etched (see (j) and (k)) revealing the faces of the bigger particles. In the surface of the remaining crystals, square pits similar to the ones seen in samples etc5 and etc6 were developed.

Figure 6.5 shows micrographs from samples c8 (m), tc8(n) and etc8(o,p). The hydrogen plasma etched most of the smooth surface of sample tc8, leaving some of the cauliflower-like big particles very damaged. Those big particles were formed by secondary nucleation on crystals showing {100} faces (m).

Finally, Figure 6.6 shows micrographs from the cross-section of samples etc6 and etc7. The four samples etched with hydrogen presented a small gap between layers. These layers were the result of the three step growth process. Micrographs from samples etc6 and etc7 were chosen because the gaps are bigger in these samples than in the others and it is easier to see them. It is possible that the heat during hydrogen treatment altered the surface structure of the hydrogen rich layers between one deposit and the other producing the layer lifting.

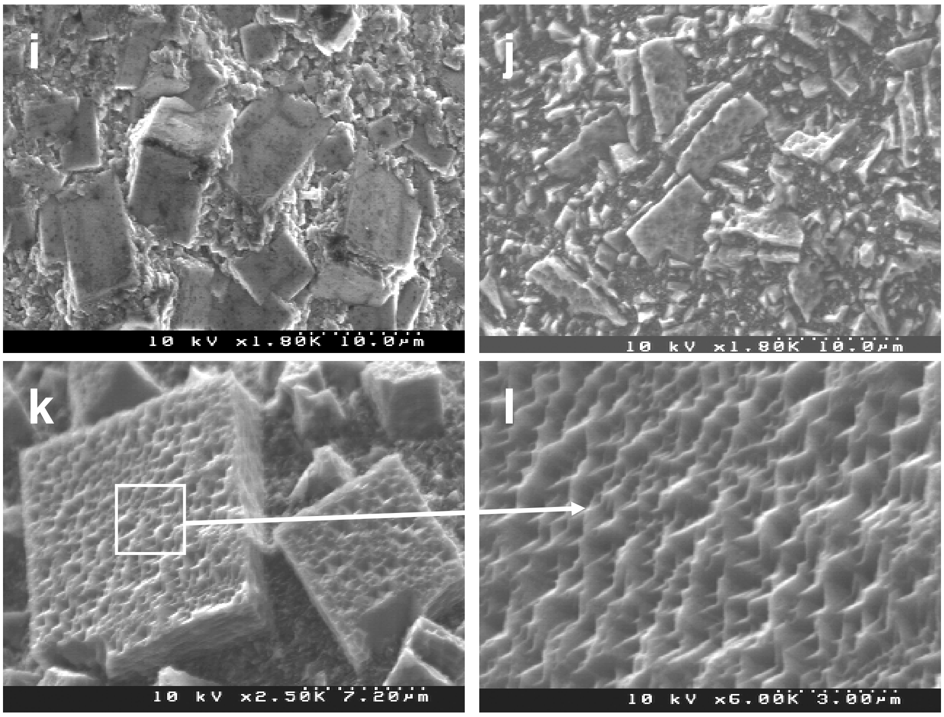

Figure 6.4: SEM micrograph from sample tc7 (i) and etc7 (j,k,l).

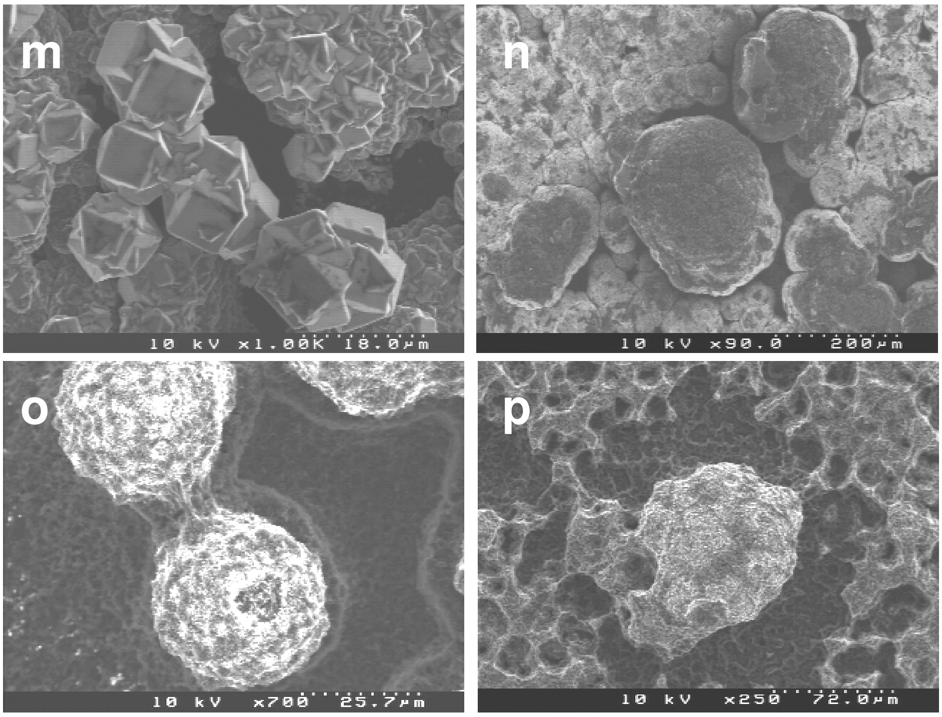

Figure 6.5: SEM micrograph from sample c8 (m), tc8 (n) and etc8 (o,p).

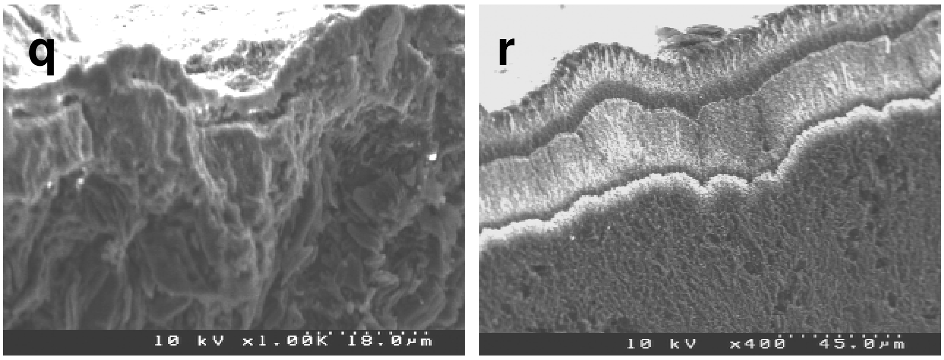

Figure 6.6: Cross section of sample etc6 (g) and etc7 (r).

6.3.2 Raman analysis

Figure 6.7 shows the Raman analyses for samples etc5 to etc8. The spectra for samples etc5 to etc7 show mainly the diamond peak at ∼1332 cm^{-1} and the D- and G-bands at ∼1350 and ∼1585 cm^{-1}. In the case of sample etc8 the diamond peak disappeared and only contributions from graphite can be seen. As a comparison Figure 6.8 shows the Raman spectra of samples tc5 to tc8. We can observe that the nanodiamond peak at 1130 cm^{-1} disappeared and D-band in samples etc5 and etc7 decreased considerably with respect to samples tc5 and tc7. Table 6.1 contains the results from deconvolution of each spectrum. We can appreciate that there is a small shift in the diamond peak position with respect to samples tc5 to tc8 (Table 5.4) and that the sp^3/sp^2 content increased dramatically in all the samples except sample etc8.

Table 6.1: Parameters from deconvoluted Raman spectra for samples etc5 to etc8.

	Diamond (sp^3)		**Graphite (sp^2)**		
Sample	**Peak** (cm^{-1})	**FWHM** (cm^{-1})	**Peak** (cm^{-1})	**FWHM** (cm^{-1})	**sp^3/sp^2**
etc5	1332.9 ±0.01	4.7 ±0.01	1591.2 ±0.4	66.3 ±0.8	1.27±0.01
etc6	1332.9 ±0.01	5.0 ±0.02	1586.2 ±0.2	30.5 ±0.4	1.22±0.01
etc7	1331.9 ±0.02	5.6 ±0.05	1586.5 ±2.1	46.9 ±4.5	3.47±0.31
etc8	—	—	1583.1 ±0.1	28.1 ±0.3	—

6.3.3 Optical Emission Spectroscopy analysis

Optical emission spectra contain a high noise/background ratio because the plasma was not intense enough, however bands from hydrogen can be distinguished. The emission lines from carbon species, specially from CH at 388 and 430 nm, are almost

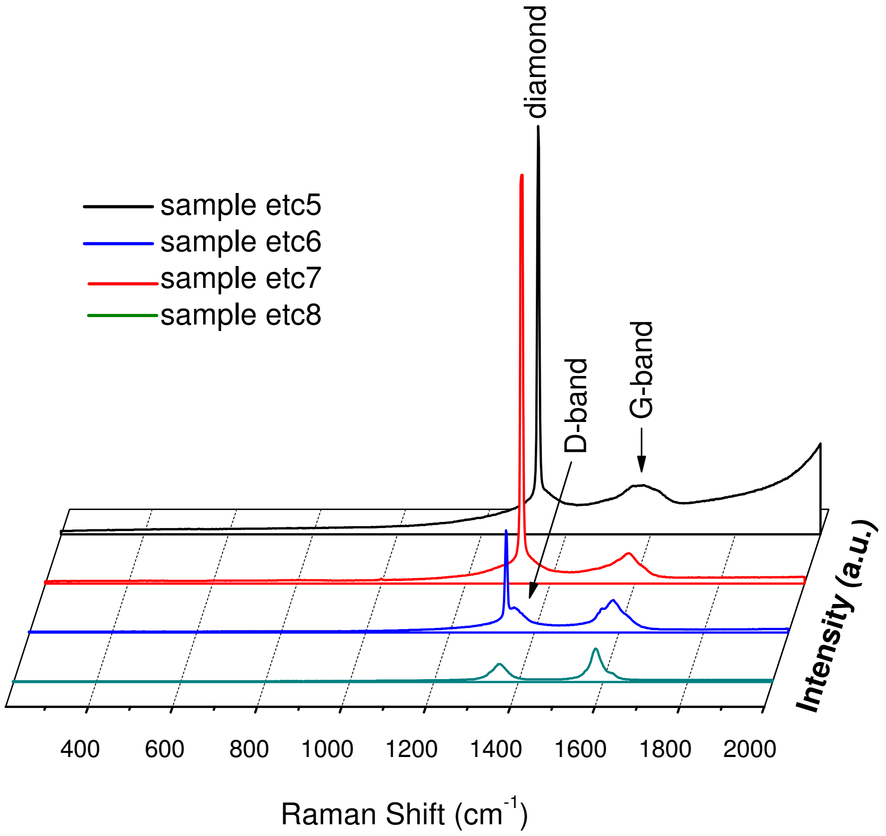

Figure 6.7: Raman spectra of samples after hydrogen plasma erosion.

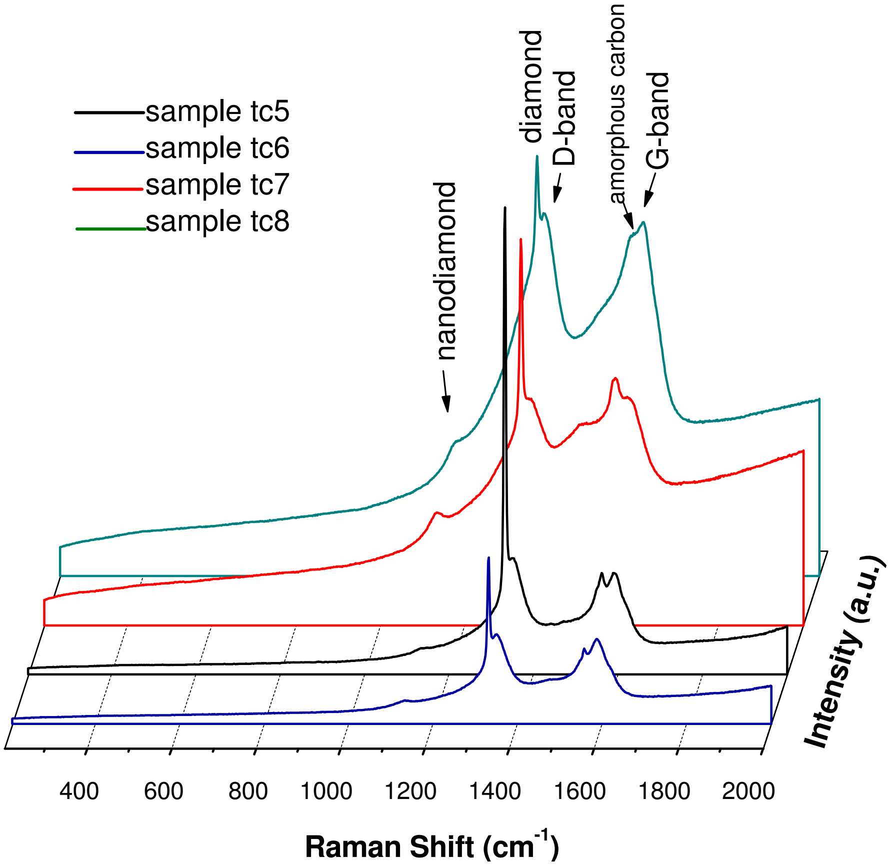

Figure 6.8: Raman of samples tc5 to tc8 before hydrogen plasma erosion.

perceptible the etching experiment for samples etc5 and etc6 (Figure 6.9), but they are higher in Figure 6.10 that corresponds to samples etc7 and etc8. This is not surprising since the content of non-diamond carbon (reflected in sp^3/sp^2 ratio in Table 5.4) was higher in these samples than for samples tc5 and tc6.

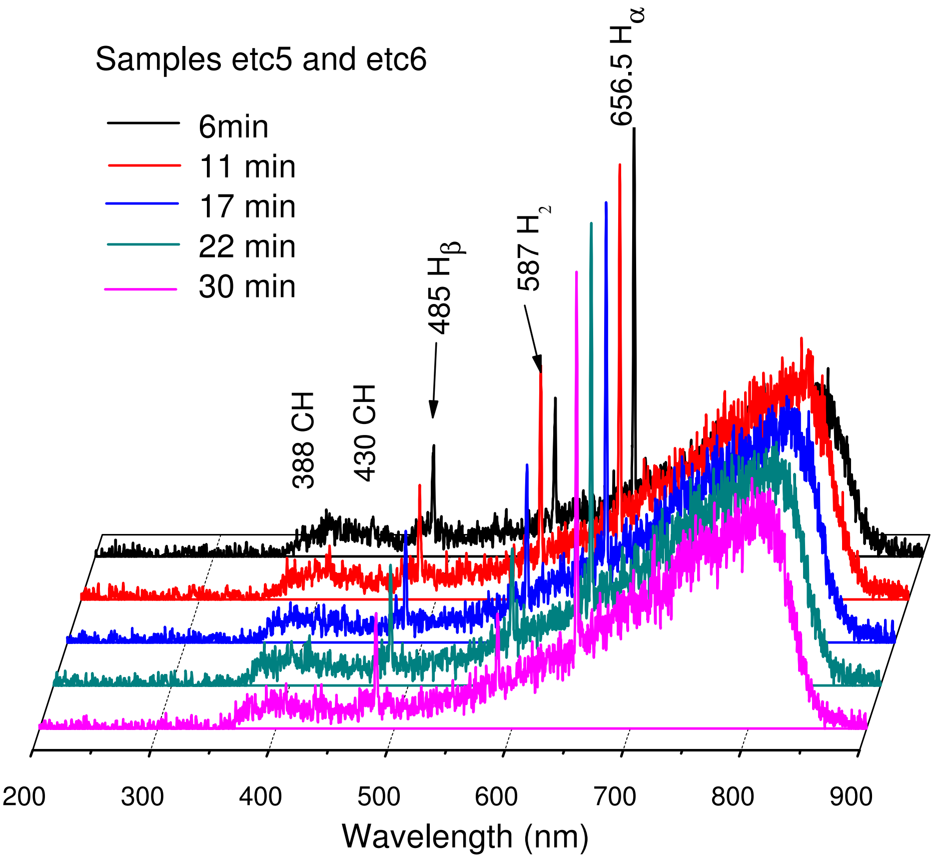

Figure 6.9: Optical Emission Spectra of hydrogen plasma erosion of samples etc5 and etc6.

6.3.4 Mass Spectroscopy analysis

Mass spectroscopy analysis during the erosion of the samples did not detect any important contrubution from carbon compounds, in fact the species detected during the experiments were the same observed before plasma ignition (Figure 6.11). The only change was seen in the CH_3OH signal that became smaller with time until it disappeared. Methanol is detected by the mass spectrometer because we used it to clean the chamber before the experiments.

6.4 Discussion

The presence of pits and steps on our etched samples is closely related with homoepitaxial [001] diamond growth-etching. Actually, there is still controversy if pits and

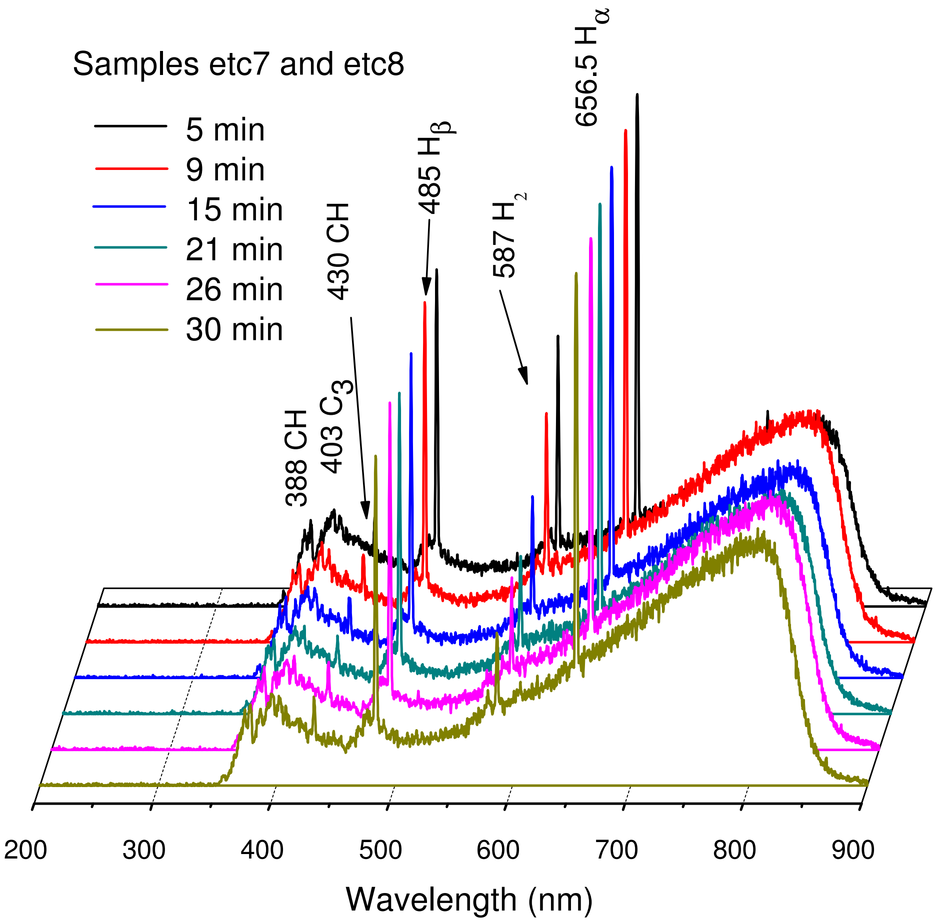

Figure 6.10: Optical Emission Spectra of hydrogen plasma erosion of samples etc7 and etc8.

steps in diamond films are produced during the growth of the film or they are produced by anisotropic etching.

The formation of steps during growth was first explained by Shiomi et al. [210]. They said that during the epitaxial growth of diamond on the {001} surface, 2x1 and 1x2 structures form, and the two domains build layer by layer (as is shown in Figure 6.12(a)). Furthermore, the growth in the presence of steps can be in two ways: 1) growth occurs only due to the step flow where the 1 x 2 domain steps have higher step-flow rate resulting in a single domain 2 x 1 surface; 2) Two-dimensional nucleation occurs on the terraces. Even if the single-domain surface has formed, another surface superstructure forms on the island (Figure 6.12(b)). The growth in model (1) happens when methane concentration in the gas mixture is low (around 2%) and the growth described by model (2) occurs when methane concentration is high (around 6%). Later, Hayashi et al. [198, 211] explained that in the step-flow growth that only occurs at low methane content, hydrocarbon precursors migrate on the terrace and are incorporated into the atomic steps before they can form a two-dimensional nucleus. They also said that surface migration is influenced by growth parameters such as CH_4 concentration, substrate temperature and microwave power

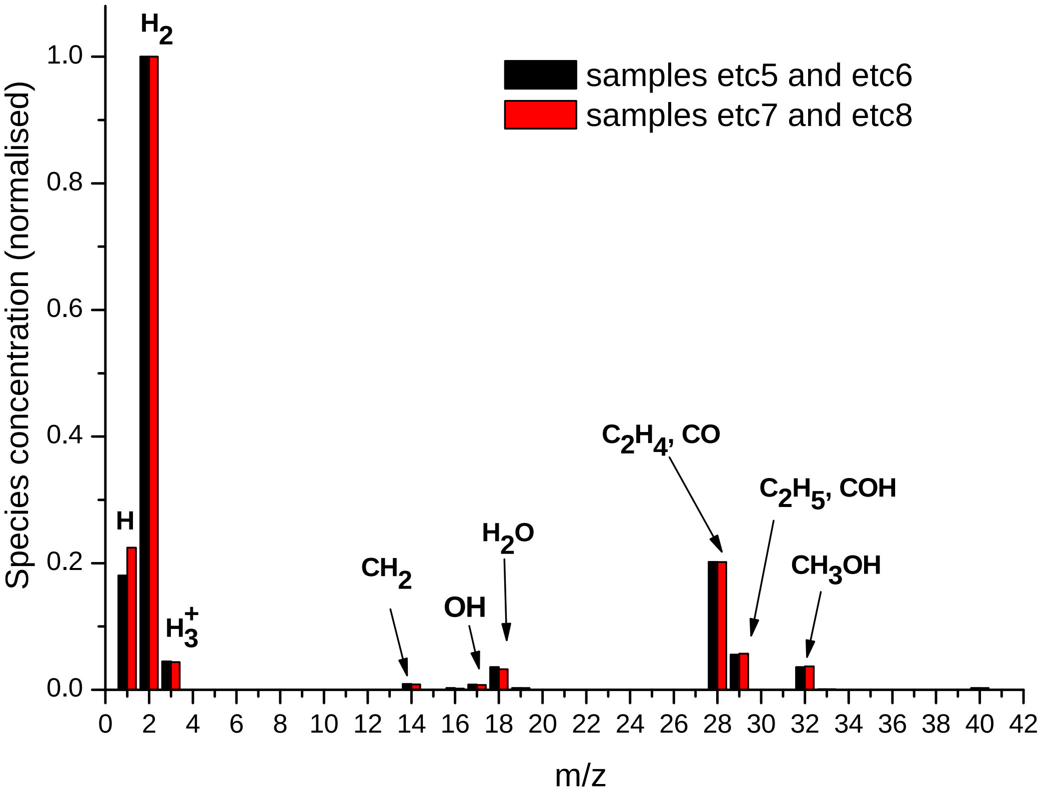

Figure 6.11: Mass spectra from the samples etc5-etc6 (black) and etc7-etc8 (red).

and that it is expected that atomic hydrogen may induce defects on the surface which can act as nucleation sites.

The formation of steps at the beginning of homoepitaxial diamond growth is due to off-angle substrates [211]. The presence of steps in our sample, in the case they are formed during growth, can be explained using the van der Drift model [212]. Nuclei form with random orientation and grow uniformly until they meet the growing surface of another crystal. The nuclei with the fastest growing crystallographic direction overgrow the nuclei with the slowest crystallographic directions producing a texture. The joints of two crystals in our samples make steps where the step flow diamond growth can proceed. The difference in step shape in sample etc5 has been explained by Lee and Badzian [213]. They said that the shape of macro steps depends on the nominal misorientation directions of substrates, as shown in Figure 6.13. When the substrate is tilted toward the [110] direction, macro steps are likely to have straight edges. On the substrate misoriented towards the [100] direction, macro steps have zigzag edges.

Van Enckevort et al. [214] proposed a model for pyramid-like hillock formation explaining that at least three different active step sources have been identified: 1) nucleation on dislocations leading to spiral growth, as has been seen in our sample etc5;

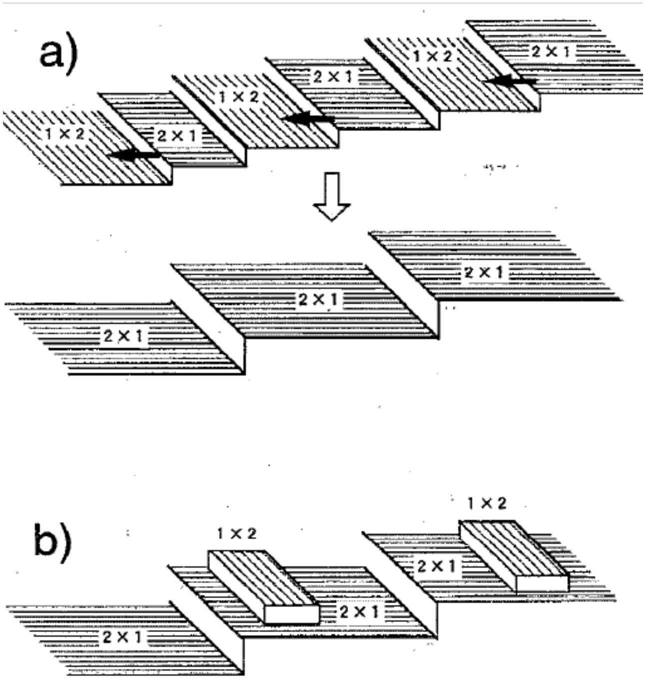

Figure 6.12: Schematic of epitaxial growth. (a) Formation of single-domain surface and (b) formation of double-domain surface due to two-dimensional nucleation [210].

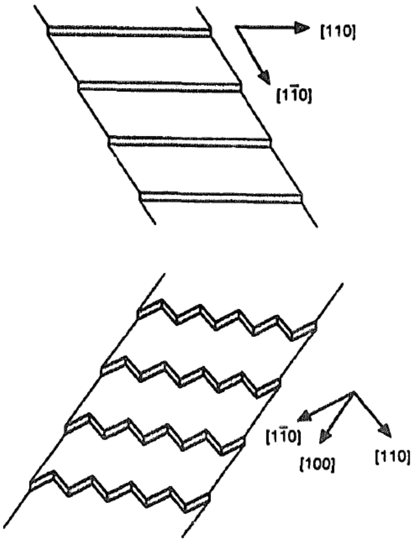

Figure 6.13: Configuration of macrosteps for the epitaxial growth on diamond (001) substrates misoriented toward (a)[1$\bar{1}$0] and (b)[100], Ref.[213].

2) contact nucleation on non-epitaxial diamond particles; and 3) contact nucleation on penetration twins. They also reported [215] that these step sources generated large hillocks on HFCVD grown diamond layers and macro-steps on flame-grown material.

Lee and Badzian [216] stated that during hydrogen plasma treatment of {100} diamond films there are two competing processes: a very efficient regression of pre-existing steps (step flow) and a step creation process which results in pits. Koslowski et al. [217] said that the mechanism could be preferential etching of local highly strained surface areas, leading to a co-operative strain relief, or anisotropic etching by the H-plasma, at extended defects like dislocations in the sample. Dislocations running preferentially along [110] are prominent candidates for causing etching patterns.

Our graphite substrates have a very rough surface, so we expect to obtain a diamond film with a high density of steps and defects, that will produce anisotropic hydrogen etching. It is difficult to say if the steps and hillocks are produced during the growth or during the etching of our samples, but the clear terrace and pits in sample tc7 may indicate that they are formed during the growth. The dependency of roughness of the surface and misoriented angles in the substrate has also been observed by Ri et al. [218].

Sample etc5 is the only one showing macro steps: we think that the low methane content during deposition favoured the step-flow growth mechanism instead of the production of new nuclei as in samples grown with higher methane content. The brick-wall pattern in this sample also suggests that the etching was predominantly by step-flow rather than by attacking the terrace as has been described by Hayashi et al. [211]. They also mentioned that there is propagation of steps during diamond etching.

The possible cause of the gaps between deposited layers could be a desorption of chemically bonded hydrogen trapped between layers: it has been reported that hydrogen desorption begins at 950 °C [219].

The fact that the sp^3/sp^2 content increased after etching suggests that the etching was faster in non-diamond carbon. Yamamoto et al. [220] reported improvements in the quality of diamond films after oxygen plasma etching. Furthermore, the shift in diamond peak position corroborates changes in the stress of films.

It is not surprising that during etching of samples etc5 and etc6 the carbon emission lines were very low, since the etching is happening mainly in non-diamond carbon and these sample have high sp^3/sp^2 content. However, the higher CH signal in samples etc7 and etc8 suggests that the etching in these samples was higher (both of them presented low sp^3/sp^2), but no quantitative conclusions can be drawn from these or mass spectroscopy analyses.

6.5 Conclusions

Thick diamond films were prepared using different methane concentrations in a mixture of CH_4-H_2-Ar and later treated in a hydrogen plasma etching environment using experimental conditions similar to the ones used during the growth of these films. After hydrogen etching the samples were analysed by SEM, finding that: the sample that was prepared using the lowest methane concentration 0.5%(etc5) presented steps and square pits; the sample prepared at 1% methane (etc6) showed only square pits in the surface of large crystals; the sample prepared using 3% methane (et7) also presented square pits in the faces of the large crystals and the small crystals were etched away; the sample prepared with the highest content of methane (etc8) and had a smooth cauliflower-like surface was badly damaged after hydrogen treatment, and no pits or steps developed in this sample. The patterns obtained after hydrogen etching in sample etc5 could be due to the development of pre-existing steps formed during the growth of the film. They also could be formed by preferential etching of non-diamond carbon and dislocations in the film. Anisotropic etching in our samples could be enhanced by stress in the films. The gap between multilayer deposits produced during hydrogen etching could be caused by desorption of the surface-bonded hydrogen due to the increase in the sample temperature. The quality of diamond films improved after hydrogen etching in samples etc5 to etc7, due to preferential etching of non-diamond carbon material but sample etc8 only showed Raman bands from graphite which can be attributed to the graphitisation of the surface.

Chapter 7

Study of other carbon structures: Carbon Fibres

7.1 Introduction

Carbon fibres (CFs) consist of platelets arranged parallel, perpendicular, or at an angle with respect to the fibre axis. They are usually refered to as tubular, platelet, herring-bone, stacked-cup and helical ribbon structures [221]. The arrangement of the graphene sheets in the carbon fibres makes them different to the carbon nanotubes which are composed of graphene sheets rolled into cylindrical form with the planes concentric with the fibre axis in an extended fullerene type arrangement. Figure 7.1 shows the different carbon fibre structures: (a) in the tubular structure the platelets are stacked in a direction parallel to the fibre axis and separated by a distance of 0.34 nm; (b) in the platelet structure the graphite platelets are stacked in a direction perpendicular to the fibre axis and are separated by a distance of 0.34 nm; (c) in the herring-bone structure the fibres consist of graphitic crystallites that are organised in conical structures, the angle of the cones is 45° and it is independent of the diameter of the fibres [222]; (d) the stacked-cup structure is made of stacked, truncated conical graphene layers (cups) along the fibre length and shows circular cross section in the transmission electron microscope which helps to distinguish it from the herring-bone structure [223]; (e) the helical-ribbon carbon nanofibres are structurally composed of a helical ribbon of graphene, spiraled about and angled to the fibre axis, much like the structure of an Archimedes screw with flats inclined to the axis. Helical-ribbon CFs commonly have outside diameters of $40-140$ nm with hollow cores of $20-60$ nm. Whereas the morphology of the discontinuous stacked-cup nanofibres only allows a discrete angular arrangement of the graphene sheets comprising the stack, the arrangement of a graphene layer forming a continuous helix may take any angle [224–226].

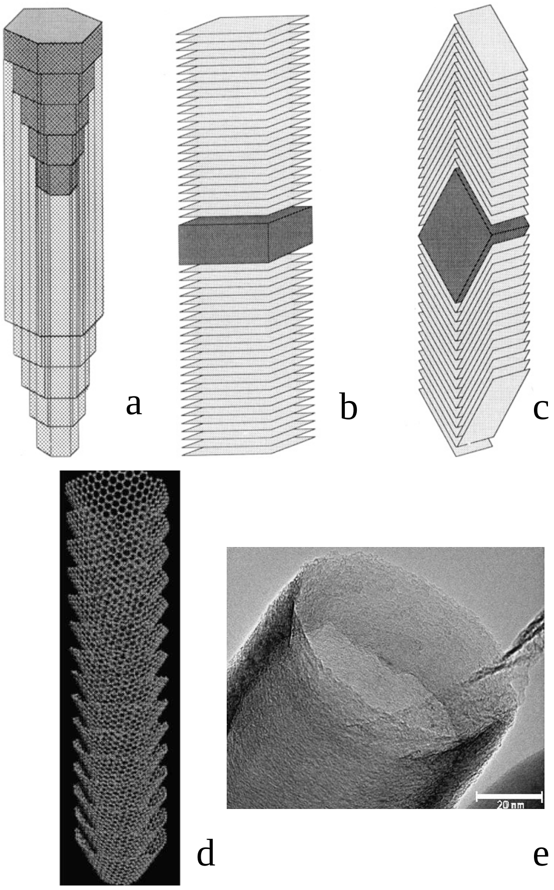

Figure 7.1: Different carbon fibres structures. (a)tubular, (b)platelet, (c)herring-bone, (d)stacked-cup, and (e)helical-ribbon structures [221, 223, 224].

Other kinds of carbon fibres have also been reported. They consist of a duplex structure of pyrolytic carbon shells embedded in a loosely-packed matrix, which is also amorphous. [227, 228]. These fibres have been mainly produced for catalysis applications.

Carbon fibres are usually synthesised by catalytic chemical vapour deposition (c-CVD) using catalyst particles such as Fe, Ni, Co, Cu or their alloys. The carbon source is commonly methane, benzene or acetylene and is mixed with hydrogen or carbon monoxide in a range of temperatures between 500 and 1200 °C [221, 229–233].

The metal catalyst plays an important role during the growth of carbon fibres. It determines the fibre structure, since the growth is parallel to the crystalline planes of the catalyst. This fact explains very well most of the CFs structures but in the case of stacked-cup and herring-bone structures, which are very similar one to each other, another explanation has been given by Kim et al. [223]. They say that stacked-cup CFs grow in molten-state metal particles while herring-bone CFs are obtained when the catalyst is in a solid state. Molten-state particles during the growth of filamentous carbon fibres have been also studied by Gadelle et al. [234] based on data from Benissad et al. [235] and Tibbets et al. [236]. Their calculations from the decomposition of methane on iron particles (6−25 nm) at 1020−1100 °C, showed that the finest iron particles (6 nm) are liquid at 1020 °C.

The catalyst size also affects the diameter of the fibre [237] although Louis et al. [238] recently reported the growing of carbon fibres with diameters of 30 nm using nickel particles of more than 100 nm.

Hydrogen is also important during the carbon fibres growth. It has been seen that it can accelerate the synthesis by decomposing the inactive metal carbides and graphitic deposits in the catalyst surface [239]. But it can also suppress the synthesis competing with the carbon species during the adsorption on the metal surface and reacting with carbon to form methane.

The presence of oxygen during the synthesis can decrease the diameter of the carbon fibres and suppress the deposition of amorphous carbon and fibre bundling [233].

The temperature affects the growth rate and the morphology of the fibres. At low temperature both straight and tight helical fibres appeared. When temperature is raised the nanofibres are mostly twisted. Amorphous filaments would be obtained at low temperature, whereas isometric shells would be obtained at high temperature [239].

It is believed that during carbon fibre growth, the hydrocarbon is adsorbed and decomposed on certain faces of the metal forming carbides, this process being followed by the diffusion of carbon atoms through the catalyst particle to precipitate at other faces in the form of a fibrous structure [221, 240]. The lengthening of the deposit produces a graphitic filament which continuously carries the catalytic particle at its end, giving rise to a hollow core. When the catalyst particle is completely covered by carbon, the fibre starts growing in diameter producing a carbon layer that is less graphitic than the filament [241–243]. It is well-established that carbon diffusion through the particle is the rate determining step in the growth process.

Among carbon fibre applications are: catalyst support materials [228, 238, 244–247], selective adsorption agents [248, 249], energy storage [250], composite materials [251], nanoelectric devices [252], field emission devices [253, 254], filter materials [255], aerosol filters [222, 256], lithium ion rechargeable batteries [257], as a substrate for diamond films [227, 258] and nanotubes [259, 260], and a recent application has been in the production of carbon nanofibre paper [261].

This chapter contains the results obtained when diamond films on graphite substrates are treated in hydrogen plasma etching conditions at high excitation power. The presence of a silicon piece during the experiments produces a catalytic reaction and carbon fibres grow on the surface of the diamond films. The fibres produced differ from one sample to the other and they vary in diameter, shape and length. To the

Table 7.1: Experimental conditions of the sample synthesis, letter “s” indicates the use of silicon piece masking part of the diamond film during the hydrogen treatment.

		1^{rst} Growth		**2nd Growth**			**H_2 Treatment**	
Sample	**Pretreatment**	**Power (kW)**	**Time (hrs)**	**Gases Mixture**	**Power (kW)**	**Time (hrs)**	**Power (kW)**	**Time (min)**
f1s	Scratched with diamond	3	2	—	—	—	4.2	15
f2*	Scratched with diamond	3	2	—	—	—	4.2	15
f3s	Scratched w/nanodiamond	1.2-1.8	2	$CH_4/H_2/Ar$	1.2-1.8	4	4.2	15
f4	Scratched w/nanodiamond	1.2-1.8	2	$CH_4/H_2/Ar$	1.2-1.8	2.5	4.2	15
f5s	Manually Scratched	1.2-1.8	4	CH_4/H_2	1.2	4	4.2	15
f6s	Scratched with diamond	1.5	2	—	—	—	—	—
f7	Scratched with diamond	1.5	2	—	—	—	—	—

best of the author’s knowledge the conditions that are used in this work to produce the fibres are different from those reported in the literature.

7.2 Experimental

The carbon fibres presented in this chapter were synthesised on nanocrystalline and polycrystalline diamond films. The films were grown under the conditions shown in Table 7.1. The substrates used were graphite except for sample f2* in which silicon was used instead. The graphite (or silicon) substrates were treated before deposition using the techniques described in Chapter 4 and listed in the Table 7.1. For the first deposition the gas mixture used was 5%CH_4, 15%H_2, 80%Ar for all the samples. The excitation power was varied in some experiments due to the instability of the plasma during deposition. A second deposition was made in some of the samples in order to increase the thickness of the film. A different gas mixture (5%CH_4 and 95%H_2) was used in sample f5s for the second deposition. When the films were fully characterised the samples were loaded for a hydrogen treatment, the samples with the “s” letter had a silicon wafer piece of 5x5 mm^2 located on one of the corners. The hydrogen treatment was carried out at 50 ±2 Torr of pressure using the same conditions (Table 7.1) for samples f1s to f5s. In the case of sample f6s the silicon piece was introduced with the pretreated graphite substrate and the deposition was carried out using the gas mixture $CH_4/H_2/Ar$. No hydrogen treatment was given to this sample. Sample f7 was treated in the same conditions as sample f6 but without the silicon wafer. The silicon pieces used in the experiments were cleaned with methanol in an ultrasonic bath for 15 min.

The XPS, SEM and Raman analysis were carried out using the experimental parameters mentioned in Chapter 2.

7.3 Results

7.3.1 SEM analysis

Figure 7.2 shows the SEM micrographs from the samples f1s to f4. 7.2(a) corresponds to sample f1s, the fibres grew on a microcrystalline diamond film whose crystal phases can still be seen in the micrograph. The carbon fibres growth was close to the silicon piece in localised areas. Figure 7.5 shows the two types of fibres that are found in this sample. In 7.5(m) are shown the straight and thin fibres of approximately 185 nm in diameter and 10 μm of length, and 7.5(n) shows the bent and thick fibres of $\sim$650 nm of diameter and less than 10 μm of length.

Figure 7.2(b) corresponds to sample f2* grown on a silicon substrate. The microcrystalline diamond film was eroded by the hydrogen plasma and no fibres grew on it.

Figure 7.2(c) corresponds to sample f3s. The fibres grown in this nanocrystalline diamond film have different diameters from 0.15 μm to 0.35 μm. The diameter of each fibre also changes along the structure being smaller towards the tip. As opposed to the fibres in sample f1s these do not have a preferential growth direction, their shape is curly and some of them present ramifications. Figure 7.2(d) shows the nanocrystalline film in sample f4. The surface has cracks as were also observed in sample f3s before hydrogen treatment. No fibres grew on sample f4.

Figure 7.3 shows SEM micrographs from sample f5s. As in previous samples the growth of the fibres was in the vicinity of the silicon piece and the rest of the surface was etched, as is shown in 7.3(h). Different types of fibres can be found in this sample: 7.3(e) short with round tips resembling nails; 7.3(f) thin and curly of approximately 0.15 μm diameter and octopus-like growth; 7.3(g) thick and short of $\sim$1.15 μm diameter and 6.35 μm length.

Figures 7.4(i) and (j) correspond to sample f6s. The fibre growth is perpendicular to the graphite and the shape is thin and curly. The higher magnification micrograph 7.4(j) shows that the fibre tips are round and larger than the rest of the fibre structures. Micrograph 7.4(k) corresponds to sample f7: the morphology of the diamond film is typical for the experimental conditions used.

Silicon masking pieces on the top of samples f1s, f3s and f5s were etched during hydrogen treatment as is shown in Figure 7.6(o). A silicon piece on top of sample f6s

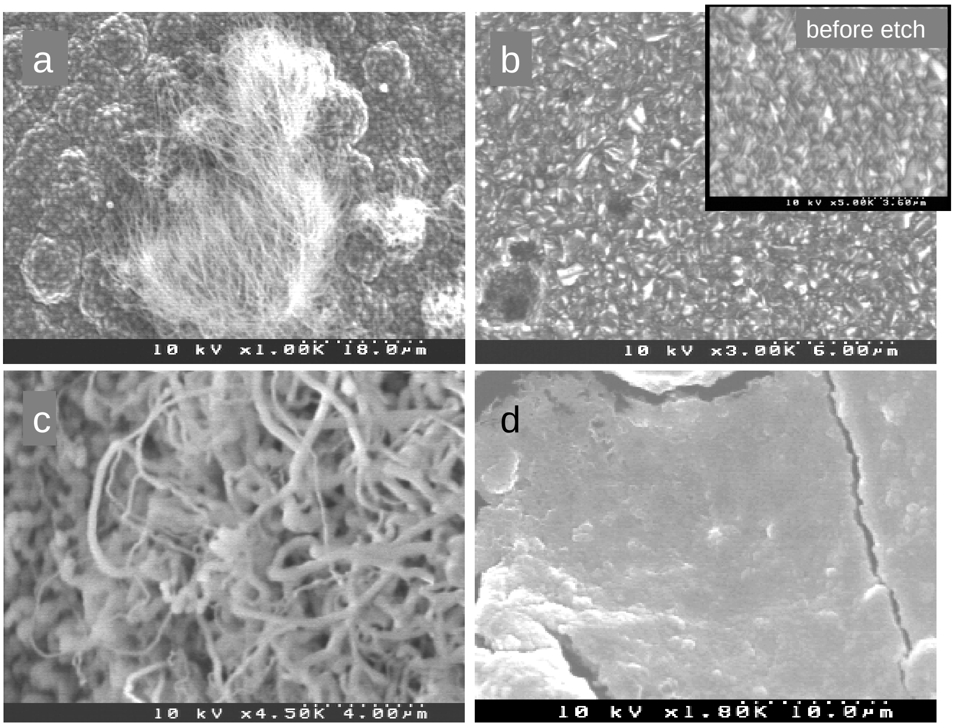

Figure 7.2: SEM micrographs from samples: (a)f1s, (b)f2*, (c)f3s, (d)f4. (a)microcrystalline film and (c)nanocrystalline film, show carbon fibres growth in the surface. Samples (b)f2* and (c)f4 were just etched.

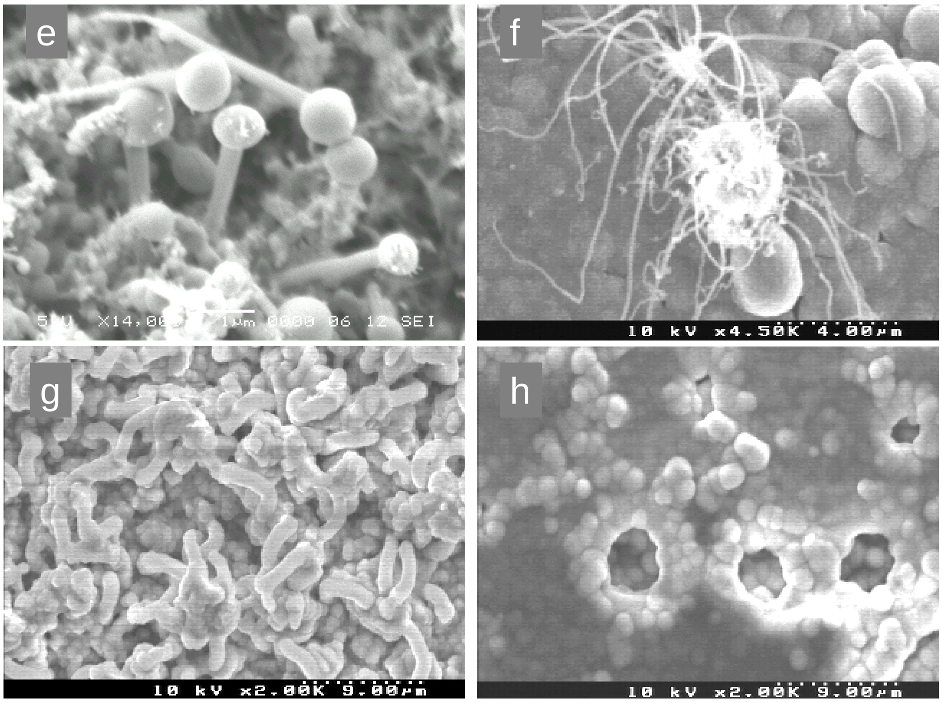

Figure 7.3: SEM micrographs from sample f5s: (e)fibres with rounded tips, (f)bent and thin fibres with octopus-like growth, (g)short and thick fibres, (h)etched surface.

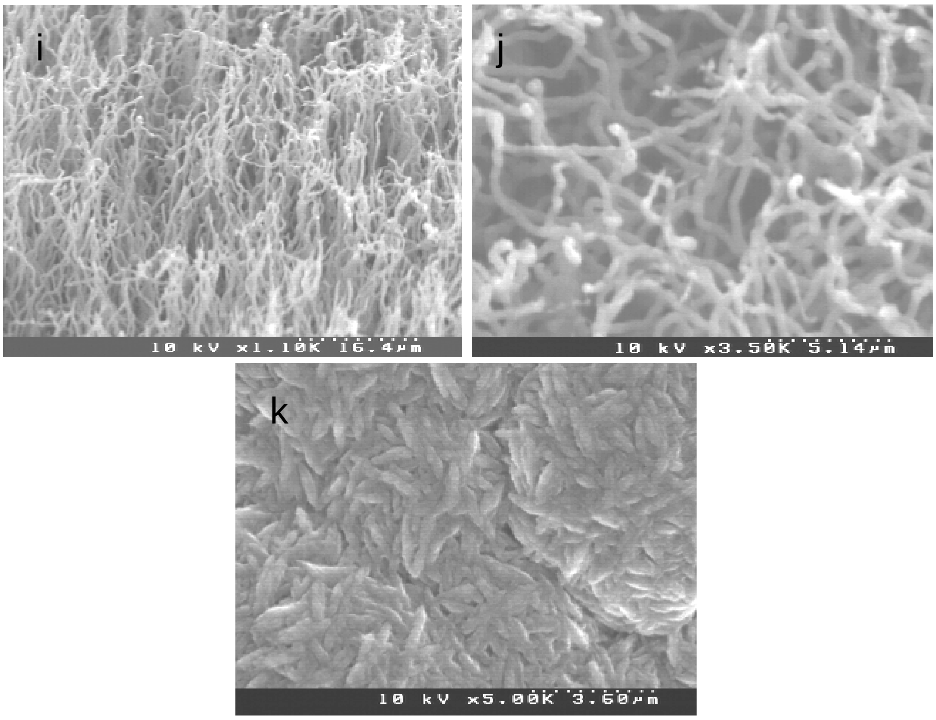

Figure 7.4: SEM micrographs from samples f6s and f7: (i)sample f6s with thin and curly fibres, (j)higher magnification of fibres in sample f6s, (k)sample f7 presenting a typical diamond film.

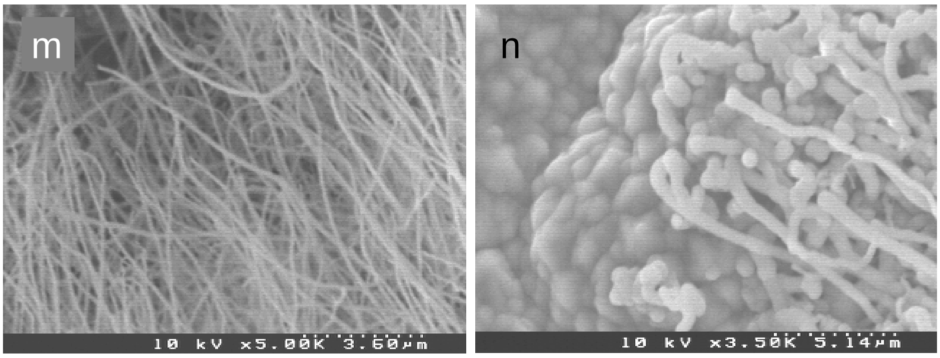

Figure 7.5: SEM micrographs from sample f1s: (m)straight and thin fibres and (n)bent and thick fibres.

presented small particles of ballas diamond (see Figure 7.6(p).

7.3.2 XPS analysis

Figure 7.7 shows the XPS analysis from all the samples. The spectra from samples f1s, f3s and f5s contain strong signals from oxygen (O1s), and weak from carbon (C1s) and silicon (Si2s and Si2p). The rest of the samples have mainly carbon contributions. The analysis of the peak areas in atomic percentage of all the samples is listed in Table 7.2. Sample f1s and f5s have the highest oxygen percentage followed by sample f3s.

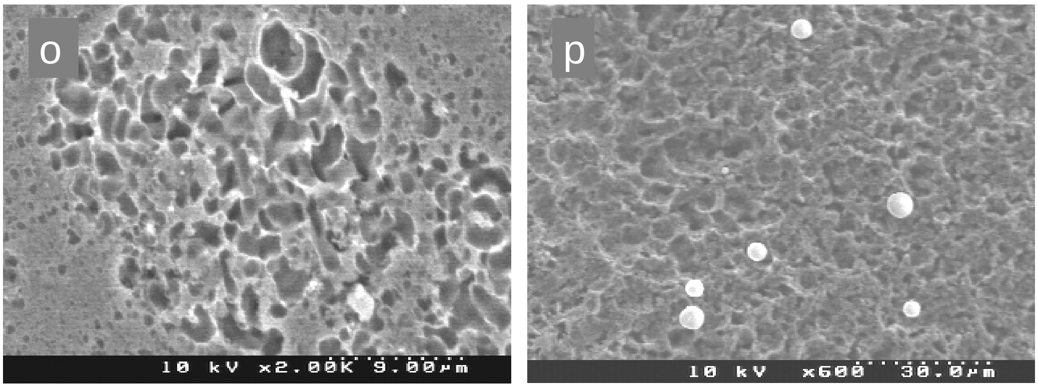

Figure 7.6: SEM micrographs from: (o) typical etched silicon masking piece on samples f1s, f3s and f5s and (p) silicon masking piece on sample f6s presenting ballas diamond.

The deconvolution of the C1s peak for samples f3s and f4 is shown in Figures 7.8 and 7.9, respectively. They present contributions from carbon sp^3, sp^2 and carbon bonded with oxygen to form alcohols or ethers and carboxylic acids or esters. Table 7.3 contains the results of analysis of all the samples in curve area percentage.

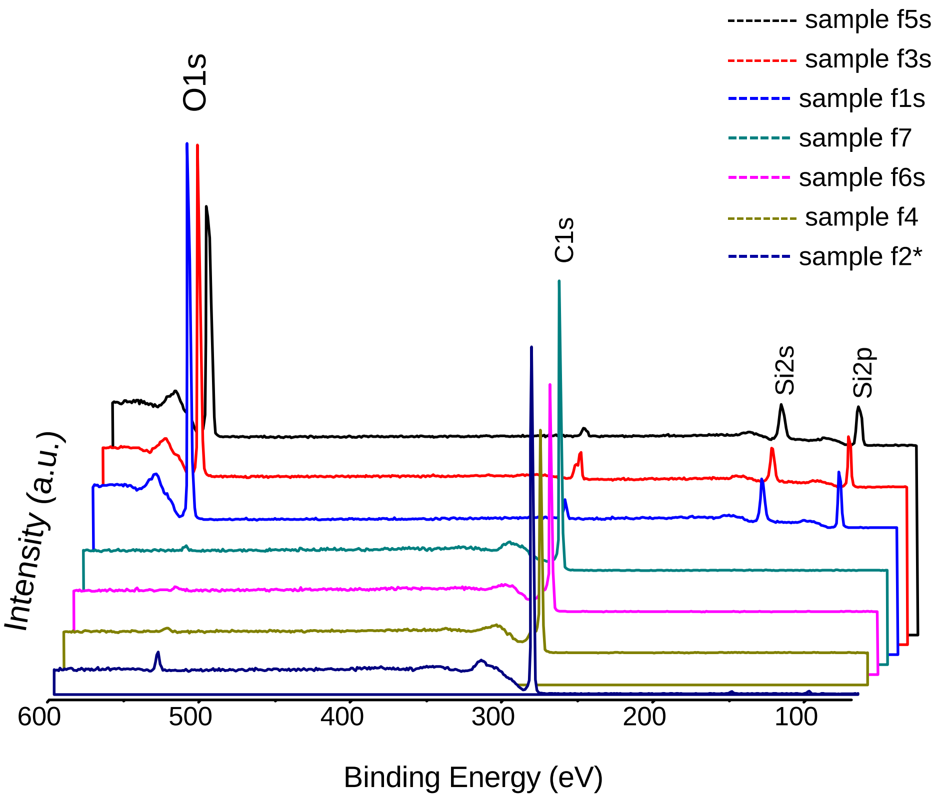

Figure 7.7: XPS analysis for all samples.

Table 7.2: XPS analysis of the sample surface in %atomic.

Sample	Carbon(1s) (%at)	Oxygen(1s) (%at)	Silicon(2p) (%at)
f1s	4.31	82.65	13.0
f2*	95.81	2.89	1.3
f3s	12.41	31.81	55.78
f4	96.38	3.62	—
f5s	11.49	75.75	12.76
f6s	98.87	1.31	—
f7	99.16	0.84	—

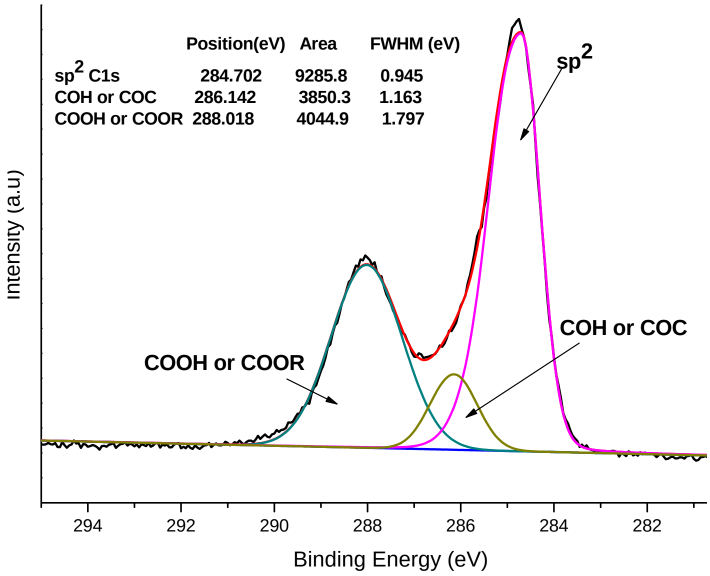

Figure 7.8: Deconvolution of C1s peak area from sample f3s.

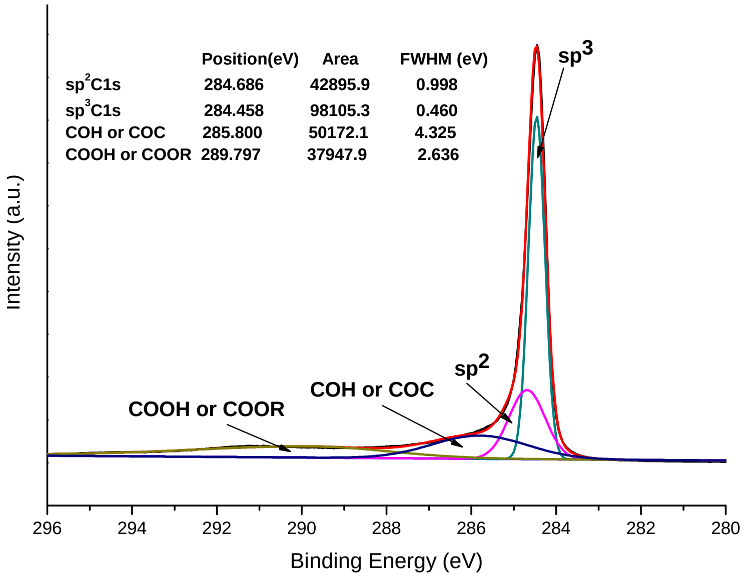

Figure 7.9: Deconvolution of C1s peak area from sample f4.

Table 7.3: Results from the deconvolution of C1s peak area for all samples.

Sample	sp^3 (%)	sp^2 (%)	Alcohol or ether(%)	Carboxylic acid or ester(%)	SiC (%)	Other (%)
f1s	—	—	—	98.99	—	1
f2*	94.02	5.98	—	—	—	—
f3s	—	62.1	8.16	29.78	—	—
f4	42.81	18.72	16.56	21.89	—	—
f5s	—	—	—	—	—	—
f6s	39.85	36.41	7.2	16.51	—	—
f7	63.04	19.61	11.58	4.72	1	—

7.3.3 Raman Spectroscopy analysis

Figure 7.10 contains the results from the Raman spectroscopy analysis for all the samples. The spectra present contributions from the broad D-band at ~1350 cm^{-1}, and the G-band at ~1550-1590 cm^{-1} due to graphite. Samples f1s to f5s also present the diamond peak at around 1332 cm^{-1}. The peak at 1154 cm^{-1} in sample f7 corresponds to nanodiamond or transpolyacetylene. Finally, the band at 2699 cm^{-1} is an overtone of the D band.

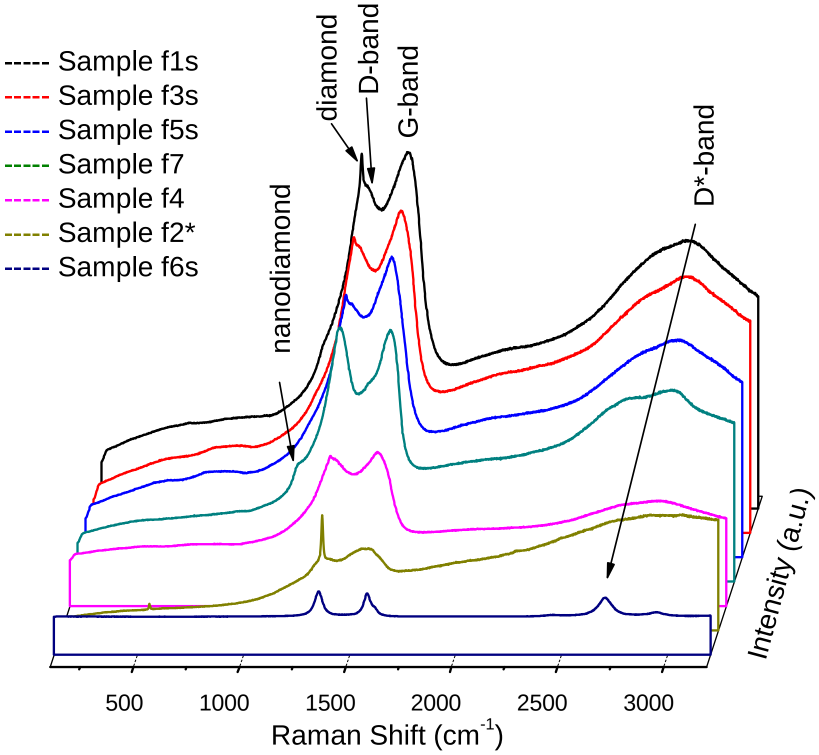

Figure 7.10: Raman spectra of all samples.

Figure 7.11 shows the deconvoluted spectrum of sample f3s, it is typical for the samples presenting the diamond peak. This is formed by five Gaussian curves from contributions corresponding to graphite, diamond and nanodiamond.

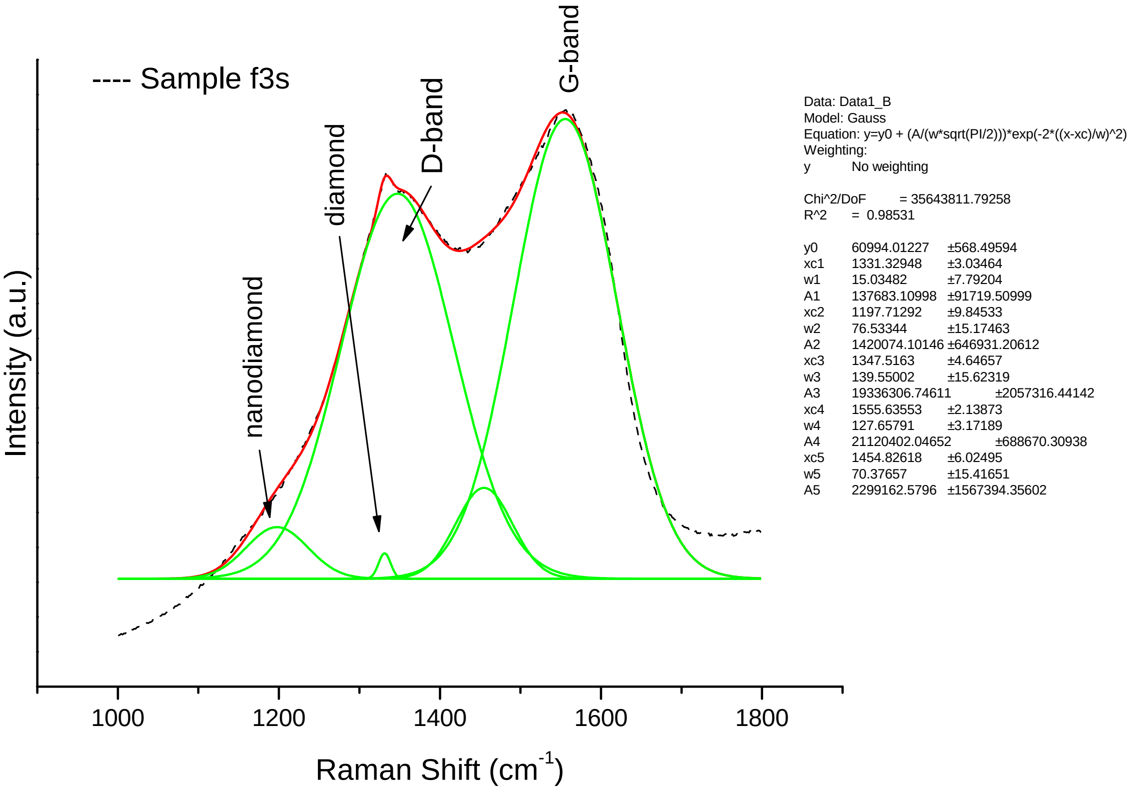

```
Data: Data1_B
Model: Gauss
Equation: y=y0 + (A/(w*sqrt(PI/2)))*exp(-2*((x-xc)/w)^2)
Weighting:
y       No weighting

Chi^2/DoF     = 35643811.79258
R^2     =  0.98531

y0      60994.01227     ±568.49594
xc1     1331.32948      ±3.03464
w1      15.03482        ±7.79204
A1      137683.10998    ±91719.50999
xc2     1197.71292      ±9.84533
w2      76.53344        ±15.17463
A2      1420074.10146 ±646931.20612
xc3     1347.5163       ±4.64657
w3      139.55002       ±15.62319
A3      19336306.74611          ±2057316.44142
xc4     1555.63553      ±2.13873
w4      127.65791       ±3.17189
A4      21120402.04652          ±688670.30938
xc5     1454.82618      ±6.02495
w5      70.37657        ±15.41651
A5      2299162.5796    ±1567394.35602
```

Figure 7.11: Deconvoluted Raman spectrum from sample f3s.

The results from the deconvolution of the Raman spectra are listed in Table 7.4. The data correspond to the D- and G-bands. Sample f6s presents considerably narrower full width at half maximum (FWHM) for both the D- and G- bands. For example FWHM D-peaks of the rest of the sample are in the range of 84-140 cm^{-1} and sample f6s is 40.2 cm^{-1} and the G-band peaks are in the range of 87-127 cm^{-1} for the rest of the samples and f6s is only 34.8 cm^{-1}. This can be due to the fact that most of the fibres are grown on diamond films and fibres in sample f6s grew directly on the graphite substrate. This suggest that D- and G-bands in most of the samples have contributions from sp^2 from nano and microcrystalline diamond films.

7.3.4 Optical Emission analysis

The results from the optical emission analysis during the hydrogen treatment for the samples f1s to f5s after 5 and 15 min of treatment is shown in Figures 7.12 and 7.13, respectively. The spectra of the samples show emission bands from the Balmer series at 656.5, 485 and 587 nm corresponding to H_α, H_β and H_γ. Sample f5s presents strong contributions from CH at 388, 418, 430 and 776 nm, at 5 and 15 min of treatment.

Table 7.4: Parameters from deconvoluted Raman spectra for the prepared samples.

	D-band		**G-band**	
Sample	**Peak** (cm^{-1})	**FWHM** (cm^{-1})	**Peak** (cm^{-1})	**FWHM** (cm^{-1})
f1s	1344 ±3	142 ±9	1553 ±2	121 ±3
f2*	1335 ±3	90 ±4	1560 ±8	109 ±7
f3s	1347 ±5	140 ±16	1556 ±2	128 ±3
f4	1352 ±2	146 ±9	1565 ±2	109 ±2
f5s	1346 ±5	140 ±16	1547 ±2	123 ±2
f6s	1354 ±1	40 ±1	1583 ±1	35 ±1
f7	1344 ±4	93 ±13	1581 ±4	88 ±4

The strong lines at 471 and 516 nm from C_2, usually present during diamond growth, are not seen in any of these samples.

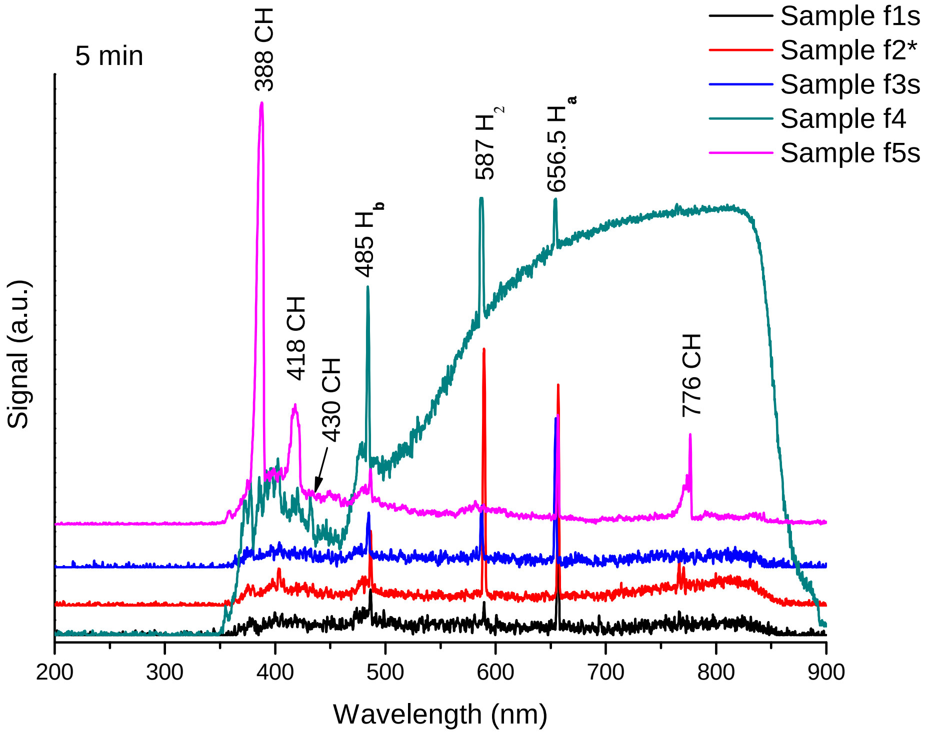

Figure 7.12: Optical emission spectra from samples f1s to f5s after 5 min hydrogen treatment.

Table 7.5 contains the intensities of the H_β and H_α lines and the ratios of the emission lines H_α/H_β for samples f1s to f5s after 5 and 15 min of deposition. It is interesting that H_α/H_β ratio of sample f4 is the lowest after 5 min of treatment and the highest after 15 min., but I do not know what could be the reason. The intensities were corrected for the detector sensitivity using the calibration constant obtained by equation

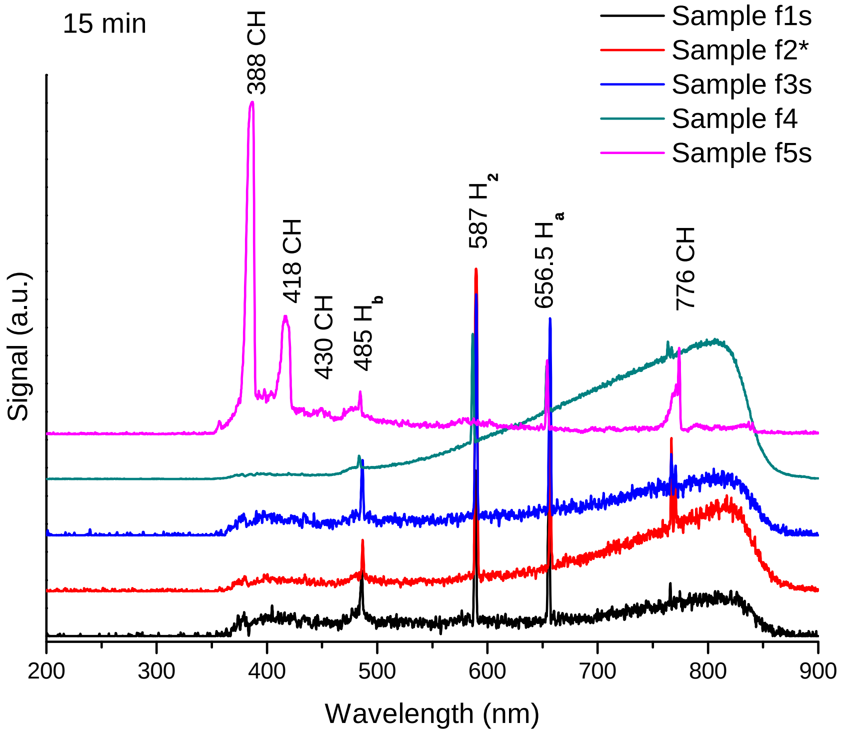

Figure 7.13: Optical emission spectra from samples f1s to f5s after 15 min hydrogen treatment.

(2.1) described in Chapter 2. Table 7.5 also contains the respective electron plasma temperatures obtained using equation (2.4).

Table 7.5: Parameters from corrected optical emission spectra for samples f1s to f5s.

	5 min				**15 min**			
Sample	$\mathbf{H}_\beta$	$\mathbf{H}_\alpha$	$\mathbf{H}_\alpha/\mathbf{H}_\beta$	$\mathbf{T}_e$ (Kelvin)	$\mathbf{H}_\beta$	$\mathbf{H}_\alpha$	$\mathbf{H}_\alpha/\mathbf{H}_\beta$	$\mathbf{T}_e$ (Kelvin)
f1s	2.9E10	1.85E12	64±11	2316±398	5.67E10	4.85E12	86±15	2128±366
f2*	5.0E10	4.78E12	96±16	2064±355	4.54E10	4.62E12	100±17	2030±349
f3s	3.27E10	3.13E12	96±16	2064±355	6.65E10	6.16E12	93±16	2081±358
f4	1.99E11	9.22E12	46±8	2564±440	1.81E10	3.06E12	169±29	1789±308
f5s	3.6E10	2.39E12	66±11	2288±393	3.38E10	2.01E12	60±10	2366±407

7.4 Discussion

There are several observations from the SEM micrographs that can give us some ideas of how the carbon fibres are growing. First of all, it is clear that the silicon piece used as a mask has a crucial role in the production of the fibres, since no fibres grew in the samples that did not have the silicon. The growth of the fibres is in specific areas, which is clear in picture 7.2(a), due to the transport by the plasma, of the small particles etched from the silicon wafer. Except for f6s, the prepared samples contain fibres that vary in thickness and length in different areas which can be due to the carbon content available near to the growing fibres. For example if the silicon particles etched from the wafer are deposited near to a film crack the carbon content in this area will be higher than where there is a continuous film. The high content of methane will also affect the size and thickness of the fibre as has been proposed by Bower et al.[262] in their nanotube growing model where the growth of the tubes stops when the metal particle is saturated by carbon species; from then the fibres begin to increase in diameter.

It is not clear that the morphology of the diamond film has any effect on the final morphology of the fibres. The fibre density in sample f6s is higher than in the other samples. This can be due to the higher erosion rate of the silicon piece caused by the presence of argon; the long fibres can be due to the higher carbon concentration and longer experiment duration. It is possible that the catalyst particles are located in the tips of these fibres and migrated towards the end of the fibre. It is also known [238] that octopus-like growth is due to the big catalyst particle size, where several fibres grow on the different catalyst faces.

The XPS analysis showed that some of the samples have the surface completely oxidised. The presence of peaks from alcohol or ether and specially carboxylic acid or ester at ∼288 eV, can be compared with carbon fibres that have been oxidised in strong acid mixtures [263].

Since no oxygen is added to the gas mixture it is probable that the samples had been oxidised when exposed to the air or during the treatment by the reaction with the oxygen bonded in the silicon piece, however if only the latter option were the case, the samples f4 and f7 would not have oxygen bonded in the surface. However the samples with fibres have a higher oxygen content, which could also be due to the higher surface area.

The Raman analyses of the samples have contributions that correspond to the reported Raman spectra for carbon fibres which exhibit two Raman-active modes. The E_{2g} mode at around 1350 cm^{-1} has been related to polycrystalline graphite and its intensity depends on the particle size [264]. The second mode is the A_{1g} at around 1580 cm^{-1} which has been identified with the doubly degenerated deformation mode of the hexagonal ring structure, observed in graphite single crystals. The intensities from diamond and nanodiamond suggest that each spectrum is a sum of contributions from the carbon fibres, the film and even from the graphite substrate below the diamond film, in which case it is difficult to obtain a conclusion from Raman spectroscopy analysis.

The Balmer band detected in optical emission analysis is expected since only hydrogen is used during the treatment. The presence of weak CH bands is also seen in most of the samples due to the surface erosion: the carbon etched from the surface will be the source for the fibre growth. In the case of sample f5s the CH peaks are much more intense than in the other samples which could be due to a higher surface erosion.

None of the optical emission spectra during the hydrogen treatment showed the prescence of the C_2 radical which has been reported by Mori et al.[233] to be responsible for the carbon fibre growth.

7.5 Conclusions

Carbon fibres were prepared by catalytic chemical vapour deposition reaction using only hydrogen plasma and diamond films as substrates. A silicon wafer piece was the catalyst during the reaction. These fibres were grown in conditions very different from those usually reported in the literature, specially the high power (4.2 kW) and the unconventional silicon catalyst. The fibres varied in size and shape being both thin and long ($\sim$185 nm diameter and 10 μm long) and thick and short (1.15μm diameter and 6.35 μm long). Some of the fibres have a bigger diameter in the tip probably due to the presence of the catalyst in this area. XPS analysis shows that the surfaces of some of the samples are oxidised and the carbon is bonded with oxygen to form alcohols or ethers and carboxylic acids or ester. Raman analysis showed contributions mainly from graphite but peaks from microcrystalline and nanocrystalline diamond from the diamond film also appeared. Optical emission analysis during hydrogen treatment showed the Balmer band in all the samples and weak bands from CH. The presence of strong CH bands in sample f5s can be due to a higher surface etching. The production of carbon fibres during hydrogen treatment gives us an idea of what could happen in plasma fusion conditions, especially the reaction of carbon with other materials in the chamber such as beryllium and tungsten.

Chapter 8

Conclusions and Future Work

The growth of good quality micro- and nano-crystalline diamond films on graphite is demonstrated for the first time in this work and the experimental parameters to produce these diamond films by microwave CVD have been established.

As a precursor to these syntheses, experiments carried out to remove non-diamond carbon in commercial detonation nanodiamond improved the quality of the powders, however the addition of other techniques such as ball milling and powerful sonication is advised for further purification. Moreover this material may be used to nucleate diamond growth on graphite if due regard is paid to its purity.

The experiments to enhance nucleation density during diamond deposition showed us that substrate pretreatment before growth plays a crucial role in the final morphology of the films and that most of the pretreatments used, including heating the sample in air and nitrogen, enhanced diamond nucleation density. In general hydrogen plasma etching is a good pretreatment for graphite substrates because it avoids the use of diamond seeds or other materials that can introduce impurities during pretreatment. If a microcrystalline diamond film on graphite is desired, the best pretreatment is to sonically scratch the substrate with diamond, heat in air for 2 days at 200 °C and use 3 or 3.6 kW excitation power during deposition. This results in high surface area covered and high diamond quality (sp^3/sp^2).

The excitation power used during deposition affects mainly the diamond crystallite size. Microcrystalline films were obtained when the excitation power was 3.0 and 3.6 kW and nanodiamond films were observed when 1.5 kW was used, independently of the pretreatment. However, the film morphology at higher powers is completely dependent on substrate pretreatment.

Concerning plasma composition we conclude that the use of argon is essential for growing diamond on graphite and the methane content affects the morphology, the sp^3/sp^2 content and the crystallite size of the films. When using less than 5% of methane in the gas mixture, {100} faces predominate even after long periods of deposition. Using 5% of methane results in a film with cauliflower-like structure. The change in the morphology when depositing for longer periods of time is caused mainly by secondary nucleation. Mass spectrometry analysis showed that the plasmas with 0.5% methane mixture had higher content of CH_3 and CH_2 species than mixtures containing 3 and 5 % methane. Furthermore, mixtures with 3 and 5% of methane had higher content of C_2H_x species. The presence of CH_x species in the reaction mixture is correlated with the resulting {100} faces. The presence of C_2H_x species is correlated with the production of nanocrystalline diamond. The optical emission results confirmed an increase of CH species when decreasing the methane content.

The patterns obtained after hydrogen etching of thick diamond films prepared at low methane concentration can be due to pre-existing steps formed during the growth of the film. They could also be formed by preferential etching of non-diamond carbon and dislocations in the film. Anisotropic etching in our samples could be enhanced by stress in the films. The gap between multilayer deposits produced during hydrogen etching could be caused by desorption of the surface-bonded hydrogen due to the increase in the sample temperature. The quality of diamond films improved after hydrogen etching in samples prepared with 0.5, 1 and 3% methane, due to the removal of non-diamond carbon material but a sample prepared with 5% methane showed Raman bands only from graphite, which can be due to graphitisation of the surface.

Finally, carbon fibres can be formed on diamond films in the presence of silicon by a catalytic reaction. These fibres were grown in very different conditions from those usually reported in the literature, especially the high power (4.2 kW). The fibres vary in size and shape being thin ($\sim$185 nm diameter and 10 μm long) and thick (1.15μm diameter and 6.35 μm long). These results make us think that in fusion plasma conditions the presence of tungsten, beryllium and other chamber materials could also react with diamond to form carbon compounds.

8.1 Future Work

Trials of our thick samples in real fusion conditions will give us a clear idea of how they behave in the presence of high fluxes of charged and neutral species and not only in hydrogen etching environments, and will provide us with the necessary information to meet the film requirements for this specific application.

Trials of the prepared diamond films under erosion conditions using hydrogen/argon mixtures will provide information about the physical erosion caused by argon ions.

Further deposition of diamond on the eroded thick samples could improve the quality of the resulting film surface since much of the non-diamond material has been removed. It would probably produce bigger crystals with [100] orientation, with low dislocation and defect density.

Further characterisation of our samples by TEM analysis will give us a better understanding of the growth mechanism of diamond films and carbon fibres by providing information of defects and dislocations in the films and by giving information about fibre structures and silicon catalyst location inside the fibres.

Deposition of electrically conductive boron-doped diamond films by microwave CVD and further hydrogen plasma etching under high microwave power and high pressure conditions.

Finally, a study of how diamond films react with other materials such as tungsten or beryllium under hydrogen plasma etching will give us an idea of what will happen during fusion experiments.

References

[1] J.C. Angus, A.H. Will, W.S. Stanko, *Growth of Diamond Seed Crystals by Vapor Deposition*, Journal of Applied Physics, **39**, 2915−2922 (1968)

[2] O.A. Shenderova, C.W. Padgett, Z. Hu, D.W. Brenner, *Diamond nanorods*, Journal of Vacuum Science and Technology B, **23**, 2457-2464 (2005)

[3] B.V. Spitsyn, B.V. Derjaguin, Author's certificate (patent application), 10 July, U.S.S.R Patent 339,134 (1956)

[4] W. Eversole, *Synthesis of diamond by deposition on seed crystals*, U.S. Patents 3,030,187 and 3,030,188 (1959)

[5] S. Matsumoto, Y. Sato, M. Kamo, N. Setaka, *Vapor deposition of diamond particles from methane*, Japanese Journal of Applied Physics, **21**, L183−L185 (1982)

[6] S. Matsumoto, *Chemical vapor of diamond in RF glow discharge*, Journal of Materials Science Letters, **4**, 600−602 (1985)

[7] M. Kamo, Y. Sato, S. Matsumoto, N. Setaka, *Diamond synthesis from gas phase in microwave plasma*, Journal of Crystal Growth, **62**, 642−644 (1983)

[8] J.M. Pineo, 1st Diamond Technology Initiative Workshop, MIT Lincoln Laboratories, Boston, 2 Feb., Paper 4 (1987)

[9] Y. Hirose, N. Kondo, Extended Abstracts, 35th Spring Meeting of the Japan Society of Applied Physics, 29 March, 434 (1988)

[10] D.V. Fedoscev, V.L. Bukhovets, I.G. Varshavskaya, *Transition of graphite into diamond in a solid phase under the atmospheric pressure*, Carbon, **21**, 237−241 (1983)

[11] J. Prins, H.L. Gaigher, *New diamond science and technology* (ed. RF. Messier, J.T. Glass, J.E. Butler and R. Roy) p.561. Pittsburgh: Materials Research Society (1991)

[12] P.K. Bachmann, W. Drawl, D. Knight, R. Weimer, R.F. Meddier, *Diamond and diamond-like materials* (ed. A. Badzian, M. Geis and G. Johnson), extended abstracts, EA-15, p.99 Pittsburgh: Materials Research Society (1991)

[13] P. Wood, T. Wydeven, O. Tsuji, *Preparation of polycrystalline diamond films in a parallel plate RF deposition*, in Science and Technology of New Diamond, (ed. S. Saito, O. Fukunaga, M. Yoshikawa), KTK Scientific Publishers/Terra Scientific Publishing Compay, p.167−170 (1990)

[14] D.E. Meyer, N.J. Ianno, J.A. Woollam, A.B. Swartzlander, A.J. Nelson, *Growth of diamond by RF plasma-assisted chemical vapor deposition*, Journal Material Research, **3**, 1397−1403 (1988)

[15] W.C. Roman, M.B. Colket, in Diamond and Diamond-like Films, (J.Dismukes, et al., eds.), Electrochemical Society Proceedings, Vol. PV89-12, p. 330, Pennington, NJ (1989)

[16] R.F. Davis, *Diamond Films and Coatings: Development, Properties, and Applications*, Noyes publication, New Jersey, U.S.A. 258−272 (1993)

[17] R. Meilunas, M.S. Wong, K.C. Sheng, R.P.H. Chang, *Early stages of plasma synthesis of diamond films*, Applied Physics Letters, **54**, 2204−2206 (1989)

[18] K. Kobashi, M.D. Nishimura, K. Kumagai, Y. Kawate, Proceedings 1st Electrochemical Society International Symposium on Diamond and Diamond-Like Coatings **89**, 296−305 (1989)

[19] C.E. Johnson, M.S. Hasting, W.A. Weimer, *Thermogravimetric analysis of the oxidation of CVD diamond films*, Journal of Materials Research, **5**, 2320−2325 (1990)

[20] T.P. Ong, R.P.H. Chang, *Low-temperature deposition of diamond films for optical coatings*, Applied Physics Letters, **55**, 2063−2065 (1989)

[21] Y. Mitsuda, Y. Kojima, T. Yoshida, K.J. Akashi, *The growth of diamonds in microwave plasma under low pressure*, Journal of Materials Science, **22**, 1557−1562 (1987)

[22] S. Yugo, A. Izumi, T. Kanai, T. Muto, T. Kimura, Proceedings of the 2nd International Conference on New Diamond Science and Technology, Pittsburg, PA, Materials Research Society, 385−390 (1991)

[23] B. Singh, O. Mesker, A.W. Levine, Y. Arie, *Growth of polycrystalline diamond particles and films by hot-filament chemical vapor deposition report* CN-5300, David Sarnoff Research Center, SRI International, Princeton, NJ (1988)

[24] P.A. Denning, D.A. Stevenson., Proceedings of the 2nd International Conference on New Diamond Science and Technology, Pittsburg, PA, Materials Research Society 403−408 (1991)

[25] P.K. Bachmann, R. Weimer, W. Drawl, Y. Liou, R. Messier, Diamond Technology Initiative Symposium, paper T20, SDEO/IST-ONR Crystal City, VA (July 12-14) (1988)

[26] J. Narayan, V.P. Godbole, C.W. White, *Laser Method for Synthesis and Processing of Continuous Diamond Films on Nondiamond Substrates*, Science, **252**, 416−418 (1991)

[27] P.E. Pehrsson, I. Hayward, A. Morrish, I. Singer, International Conference on Metallurgical Coatings and Thin Films, San Diego, CA (April 22) (1991)

[28] K.V. Ravi, C.A. Koch, H.S. Hu, A. Joshi, *The nucleation and morphology of diamond crystals and films synthesized by the combustion flame technique*, Journal of Materials Research, **5**, 2356−2366 (1990)

[29] T. Hartnett, R. Miller, D. Montanari, C. Willingham, R. Tustison, *Intermediate layers for the deposition of polycrystalline diamond films*, The Journal of Vacuum Science and Technology A, **8**, 2129−2136 (1990)

[30] D.E. Meyer, R.O. Dillon, J.A. Wollam, *Radio-frequency plasma chemical vapor deposition growth of diamond*, The Journal of Vacuum Science and Technology A, **7**, 2325−2327 (1989)

[31] K.V. Ravi, C.A. Koch, *Nucleation enhancement of diamond synthesized by combustion flame techniques*, Applied Physics Letters, **57**, 348−350 (1990)

[32] A. Sawabe, T. Inuzuka, *Growth of diamond thin films by electron-assisted chemical vapour deposition and their characterization*, Thin Solid Films, **137**, 89−99 (1986)

[33] S. Matsumoto, Y. Matsui, *Electron microscopic observation of diamond particles grown from the vapor phase*, Journal of Materials Science, **18**, 1785−1793 (1983)

[34] K. Kobashi, K. Nishimura, Y. Kawate, T. Horiuchi, *Synthesis of diamonds by use of microwave plasma chemical-vapor deposition. Morphology and growth of diamond films*, Physical Review B, **38**, 4067−4084 (1998)

[35] S. Yugo, T. Kimura, H. Kanai, *Science and Technology of New Diamond*, (S. Saito, O. Fukunaga and M. Yoshihara, eds., KTK Scientific Pub., Tokyo.) 119−128 (1990)

[36] F. Jansen, M.A. Machonkin, D.E. Kuhman, *The deposition of diamond films by filament techniques*, The Journal of Vacuum Science and Technology A, **8**, 3785−3790 (1990)

[37] C.R. Guarnieri, J.J. Cuomo, S. J. Whitehair, B.S. Berry, W.C. Pritchet, R.E. Acosta, A.D. Wilson, SPIE-Diamond Optics III, (A. Feldman and S. Holly, eds.) **1325**, 326−330 (1990)

[38] M.C. McMaster, W.L. Hsu, M.E. Coltrin, D.S. Dandy, *Experimental measurements and numerical simulations of the gas composition in a hot-filament-assisted diamond chemical-vapour-deposition reactor*, Diamond and Related Materials **4**, 1000−1008 (1995)

[39] D.G. Goodwin, G.G. Gavillet, *Numerical modelling of the filament-assisted diamond growth environment*, Journal of Applied Physics, **68**, 6393−6400 (1990)

[40] C.P. Chang, D.L. Flamm, D.L. Ibbotson, J.A. Mucha, *Diamond crystal growth by plasma chemical vapour deposition*, Journal of Applied Physics, **63**, 1744−1748 (1988)

[41] Y. Liou, A. Inspektor, R. Weimer, D. Knight, R. Messier, *The effect of oxygen in diamond deposition by microwave plasma enhanced chemical vapour deposition*, Journal of Materials Research, **5**, 2305−2312 (1990)

[42] H.C. Shih, C.P. Sung, W.L. Fan, W.T. Hsu, *Growth and morphological changes of chemically vapour deposited diamond in the presence of argon*, Thin Solid Films, **232**, 41−46 (1993)

[43] D. Zhou, T.G. McCauley, L.C. Qin, A.R. Krauss, D.M. Gruen, *Synthesis of nanocrystalline diamond thin films from an* $Ar - CH_4$ *microwave plasma*, Journal of Applied Physics, **83**, 540−543 (1998)

[44] Th.D. Makris, M. Falconieri, S. Gianoglio, L. Giorgi, R. Giorgi, N. Lisi, E. Salernitano, *Nanocrystalline diamond films by bias enhanced nucleation and argon assisted growth in a HFCVD system*, Advances in Science and Technology **48**, 44−49 (2006)

[45] Y. Tzeng, Y.K. Liu, *Diamond CVD by microwave plasmas in argon-diluted methane without or with 2% hydrogen additive*, Diamond and Related Materials **14**, 261−265 (2005)

[46] M. Tsuda, M. Nakajima, S. Oikawa, *Epitaxial growth mechanism of diamond crystal in* $CH_4 - H_2$ *plasma*, Journal of the American Chemical Society, **108**, 5780−5783 (1986)

[47] C.J. Chu, M.P. D'Evelyn, R.H. Hauge, J.L. Margrave, *Mechanism of diamond growth by chemical vapour-deposition on diamond (100), (111), and (110) surfaces: Carbon-13*, Journal of Applied Physics, **70**, 1695−1705 (1991)

[48] S.J. Harris, *Mechanism for diamond growth from methyl radicals*, Applied Physics Letters, **56**, 2298−2300 (1990)

[49] M. Frenklach, K.E. Spear, *Growth mechanism of vapour-deposited diamond*, Journal of Materials Research, **3**, 133−140 (1998)

[50] D.M. Gruen, C.D. Zuiker, A.R. Krauss, X. Pan, *Carbon dimer, C_2, as a growth species for diamond films from methane/hydrogen/argon microwave plasmas*, The Journal of Vacuum Science and Technology A, **13**, 1628−1632 (1995)

[51] P.C. Redfern, D.A. Horner, L.A. Curtiss, D.M. Green, *Theoretical studies of growth of diamond (110) from dicarbon*, The Journal of Physical Chemistry, **100**, 11654−11663 (1996)

[52] J.R. Rabeau, P. John, J.I.B. Wilson, *The role of C_2 in nanocrystalline diamond growth*, Journal of Applied Physics, **96**, 6724−6732 (2004)

[53] D.G. Goodwin, *Scaling laws for diamond chemical vapor deposition. I:Diamond surface chemistry*, Journal of Applied Physics, **74**, 6888−6894 (1993)

[54] D.G. Goodwin, J.E. Butler, in: M.A. Prelas, G. Popovici, L.K. Bigelow (Eds.), *Handbook of industrial diamond and diamond films*, Marcel Dekker, Inc. p.527 (1998).

[55] K.E. Spear, M.Frenklach, *High temperature chemistry of CVD (chemical vapor deposition) diamond growth*, Pure and Applied Chemistry, **66**, 1773−1782 (1994)

[56] E.A. Evans, J.C. Angus, *Microbalance studies of diamond nucleation and growth rates*, Diamond and Related Matererials, **5**, 200−205 (1996)

[57] P.W. May, J.N. Harvey, J.A. Smith, Y.A. Mankelevich, *Reevaluation of the mechanism for ultrananocrystalline diamond deposition from $Ar/CH_4/H_2$ gas mixtures*, Journal of Applied Physics, **99**, 104907−104911 (2006)

[58] P.W. May, J.A. Smith, Yu.A. Mankelevich, *Deposition of NCD films using hot filament CVD and $Ar/CH_4/H_2$ gas mixture*,Diamond Related Materials, **15**, 345−352 (2006)

[59] B. Sun, X. Zhang, Q. Zhang, Z. Lin, *Investigation of the growth mechanism of diamond (111) facets using high resolution electron energy loss spectroscopy*, Applied Physics Letters, **62**, 31−33 (1996)

[60] B.J. Garrison, E.J. Dawnkaski, D. Srivastava, D.W. Brenner, *Molecular dynamics simulations of dimer opening on a diamond (001)(2x1) surface*, Science, **255**, 835−838 (1992)

[61] E.J. Dawnkaski, D. Srivastava, B.J. Garrison, *Time-dependent Monte-Carlo simulations of radiacal densities and distributions on the diamond (001) (2x1)/H surface*, Chemical Physics Letters, **232**, 524−530 (1995)

[62] G. Davis, *Properties and growth of Diamond*, INSPEC, the Institution of Electrical Engineers, London, U.K. 68−69 (1993)

[63] W.S. Lee, Y.J. Baik, K.Y. Eun, D.Y. Yoon, *Metallographic etching of polycrystalline diamond films by reaction with metal*,Diamond and Related Materials, **4**, 989−995 (1995)

[64] S. Jin, W. Zhu, T. Siegrist, T.H. Tiefel, G.W. Kammlott, J.E. Graebner, M. McCormack, *Anisotropy in diamond etching with molten cerium*, Applied Physics Letters, **65**, 2675−2677 (1994)

[65] C. Uzan-Saguy, C. Cytermann, R. Brener, V. Richter, M. Shaanan, R. Kalish, *Damage threshold for ion-beam induced graphitization of diamond*, Applied Physics Letters, **67**, 1194−1196 (1995)

[66] K. Nishimara, K. Das, J.T. Glass, R.J. Nemanich, Proceedings of NATO Advanced Workshop on the Physics and Chemistry of Carbides, Nitrides and Borides, Manchester, UK Plenum, New York.

[67] J.B. Marsh, H.E. Farnsworth, *Low-energy electron diffraction studies of (100) and (111) surfaces of semiconducting diamond*, Surface Science, **1**, 3−21 (1964)

[68] Y.G. Gogotsi, A. Kailer, K.G. Nickel, *Pressure-induced phase transformations in diamond*, Journal of Applied Physics, **84**, 1299−1304 (1998)

[69] A. Pastol, Y. Catherine, *Optical emission spectroscopy for diagnostic and monitoring of CH_4 plasmas used for a-C:H deposition*, Journal of Physics D: Applied Physics, **23**, 799−805 (1990)

[70] A.N. Goyette, J.E. Lawler, L.W. Anderson, D.M. Gruen, T.G. McCauley, D. Zhou, A.R. Krauss, $\mathrm{C_2}$ *Swan band emission intensity as a function of* $\mathrm{C_2}$ *density*, Plasma Sources Science and Technology, **7**, 149−153 (1998)

[71] D. Zhou, D.M. Gruen, L.C. Qin, T.G. McCauley, A.R. Krauss, *Control of diamond film microstructure by Ar additions to* $\mathrm{CH_4/H_2}$ *microwave plasmas*, Journal of Applied Physics, **84**, 1981−1989 (1998)

[72] D.M. Gruen, S. Liu, A.R. Krauss, J. Luo, X. Pan, *Fullerenes as precursors for diamond film growth without hydrogen or oxygen additions*, Applied Physics Letters, **64**, 1502−1504 (1994)

[73] J. Griffin, P.C. Ray,*Role of inert gas in the low-temperature nano-diamond chemical vapour deposition process*, Nanotechnology, **17**, 1225−1229 (2006)

[74] G. Balestrino, M. Marinelli, E. Milani, A. Paoletti, I. Pinter, A. Tebano, P. Paroli, *Growth of diamond films: General correlation between film morphology and plasma emission spectra*, Applied Physics Letters, **62**, 879−881 (1993)

[75] M.A. Elliott, P.W. May, J. Petherbridge, S.M. Leeds, M.N.R. Ashfold, W.N. Wang, *Optical emission spectroscopic studies of microwave enhanced diamond CVD using* CH_4/CO_2 *plasmas*, Diamond and Related Materials, **9**, 311−316 (2000)

[76] Z.Y. Zhou, G.C. Chen, B. Li, S.J. Askari, W.Z. Tang, C.M. Li, J.H. Song, Y.M. Tong, F.X. Lu, *Application of optical emission spectra in controlling dominant crystalline surface of diamond films deposited by DC arc plasma jet CVD*, Surface and Coatings Technology **201**, 4987−4990 (2007)

[77] T.P. Mollart, K.L. Lewis,*Optical-quality diamond growth from* CO_2*-containing gas chemistries*, Diamond and Related Materials, **8**, 236241 (1999)

[78] J. Petherbridge, P.W. May, S.R.J. Pearce, K.N. Rosser, M.N.R. Ashfold, *Molecular beam mass spectrometry investigations of low temperature diamond growth using* CO_2/CH_4 *plasmas*, Diamond and Related Materials, **10**, 393−398 (2000)

[79] S. M. Leeds, *Characterisation of the gas-phase enviroment in a microwave plasma enhanced diamond chemical vapour deposition reactor using molecular beam mass spectroscopy*, Ph.D. Thesis, University of Bristol (1999)

[80] H. Sternschulte, T. Bauer, M. Schreck, B. Stritzker, *Comparison of MWPCVD diamond growth at low and high process gas pressures*, Diamond and Related Materials, **15**, 542−547 (2006)

[81] S.J. Harris, A.M. Weiner, T.A. Perry, *Measurement of stable species present during filament-assisted diamond growth*, Applied Physics Letters, **53** 1605−1607 (1988)

[82] H. Zhou, J. Watanabe, M. Miyake, A. Ogino, M. Nagatsu, R. Zhan, *Optical and mass spectroscopy measurements of* $Ar/CH_4/H_2$ *microwave plasma for nano-crystalline diamond film deposition*, Diamond and Related Materials **16**, 675−678 (2007)

[83] H. Sternschulte, M. Schreck, B. Stritzker, *In situ characterisation of CVD diamond growth under* H_2S *addition by optical emission spectroscopy, mass spectroscopy and laser reflection interferometry*, Diamond and Related Materials, **11**, 296−300 (2002)

[84] N.G. Ferreira, E.J. Corat, V.J. Trava-Airoldi, N.F. Leite, *OES study of the plasma during CVD diamond growth using* $CCl_4/H_2/O_2$ *mixtures*, Diamond and Related Materials, **9**, 368−372 (2000)

[85] R. Robertson, J.J. Fox, *Infra-red spectrum of diamond by Infra-red Spectrometer and Raman Methods*, Nature, **125**, 704−704 (1930)

[86] P. John, D.K. Milne, I.C Drummond, M.G. Jubber, I.I.B.Wilson, J.A. Savage, *IR attenuated total reflectance studies of d.c. biased growth of diamond films*, Diamond and Related Materials, **3**, 486-491 (1994)

[87] K.M. McNamara, B.E. Williams, K.K. Gleason, B.E. Scruggs, *Identification of defects and impurities in chemical-vapor-deposited diamond through infrared spectroscopy*, Journal of Applied Physics, **76**, 2466−2472(1994)

[88] C.A. Klein, T.M. Hartnett, C.J. Robinson, *Critical-point phonon frequencies of diamond*, Physical Review B, **45**, 12854−12863 (1992)

[89] K.M. McNamara, B.E.Scruggs, K.K.Gleason, *The effect of impurities on the IR absorption of chemically vapour deposited diamond*, Thin solid films, **253**, 157−161 (1994)

[90] C.J. Tang, A.J. Neves, M.C. Carmo, *On the two-phonon absorption of CVD diamond films*, Diamond and Related Materials, **14**, 1943−1949 (2005)

[91] E. Titus, D.S. Misra, A.K. Sikder, P.D. Tyagi, M.K. Singh, A. Misra, N. Ali, G. Cabral, V.F. Neto, J. Gracio, *Quantitative analysis of hydrogen in chemical vapour deposited diamond films*, Diamond and Related Materials, **14**, 476−481 (2005)

[92] E. Titus, N. Ali, G. Cabral, J.C. Madaleno, V.F. Neto, J. Gracio, P. Ramesh Babu, A.K. Sikder, T.I. Okpalugo, D.S. Misra, *Nitrogen and hydrogen related infrared absorption in CVD diamond films*, Thin Solid Films, **515**, 201−206 (2006)

[93] C.D. Clark, S.T. Davey, *One-phonon infrared absorption in diamond*, Journal of Physics C: Solid State Physics, **17**, 1127−1140 (1984)

[94] C. Ramaswamy, *Raman effect in diamond*, Nature, **125**, 704−704 (1930)

[95] D.S. Knight, R. Weimer, L. Pilione, W.B. White, *Surface-enhanced Raman spectroscopy of chemical vapour deposited diamond films*, Applied Physics Letters, **56**, 1320−1322 (1990)

[96] D.S. Knight, W.B. White, *Characterization of diamond films by Raman spectroscopy*, Journal of Materials Research, **4**, 385−393 (1989)

[97] L. Bergman, R.J. Nemanich, *Raman spectroscopy for characterization of hard, wide-bandgap semiconductors: Diamond, GaN, GaAlN, AlN, BN*, Annual Review of Materials Science, **26**, 551−579 (1996)

[98] P. John, D.K. Milne, W.C. Vijayarajah, M.G. Jubber, J.I.B. Wilson, *The growth of (100) orientated diamond films*, Diamond and Related Materials, **3**, 388−392 (1994)

[99] S. Reich, C. Thomsen, *Raman spectroscopy of graphite*, Philosophical Transactions of the Royal Society London A, **362**, 2271−2288 (2004)

[100] R.J. Nemanich, S. A. Solin, *First- and second-order Raman scattering from finite-size crystals of graphite*, Physics Review B, **20**, 392−401 (1979)

[101] P.G.N. Nayar, *Temperature variation of the Raman frequency of diamond*, Proceedings of the Indian Academy of Science, Section A, **13**, 284−290 (1941)

[102] M.J. Chiang, M.H. Hon, *X-ray photoelectron spectroscopy investigation of substrate surface pretreatments for diamond nucleation by microwave plasma chemical vapour deposition*, Journal of Crystal Growth, **211**, 211−215 (2000)

[103] M.M. Waite, S.I. Shah, *X-Ray photoelectron spectroscopy of initial stages of nucleation and growth of diamond thin films during plasma assisted chemical vapour deposition*, Applied Physics Letters, **60**, 2344−2346 (1992)

[104] A. Cook, A.G. Fitzgerald, B.E. Storey, J.I.B. Wilson, P. John, M.G. Jubber, D. Milne, I. Drummond, J.A. Savage, S. Haq, *A microbeam analytical characterization of diamond films*, Diamond and Related Materials, **1**, 478−485 (1992)

[105] C.N. Belton, S.J. Harris, S.J. Schmieg, A.M. Weiner, T.A. Perry, *In situ characterization of diamond nucleation and growth*, Applied Physics Letters, **54**, 416-417 (1989)

[106] F.R. McFeely, A.P. Kowalczyk, L. Ley, R.G. Cavell, R.A. Pollak, D.A. Shirley, *X-ray photoemission studies of diamond, graphite, and glassy carbon valence bands*, Physical Review B, **9**, 5268−5278 (1974)

[107] D.V. Isakov, V.I. Petrov, M.V. Chukichev, P. John, N. Polwart, J. Wilson, Y.Y. Liu, D.S.H. Chan, J.C.H. Phang, *Cathodoluminescence of diamond films grown by microwave plasma chemical deposition*, 3rd International Conference on Advanced Materials Processing (ICAMP-3), Melbourn, Nov-Dec (2004)

[108] D. Pickrell, W. Zhu, A.R. Badzian, R. Messier, R.E. Newnham, *Near-interface characterization of diamond films on silica and silicon*, Journal of Materials Research, *6*, 1264−1277 (1991)

[109] A.G. Fitzgerald, Y. Fan, C. Kisielowski, P. John, C.E. Troupe, J.I.B. Wilson, *High resolution TEM observation of CVD diamond Films*, Proceedings from the electron microscopy and analysis group conference, Dundee 39−42 (2001)

[110] G.H.M. Ma, Y.H. Lee, J.T. Glass, *Electron microscopic characterization of diamond films grown on Si by bias-controlled chemical vapor deposition*, Journal of Materials Research, **5**, 2367−2377 (1990)

[111] J.L. Kaae, P.K. Gantzel, J. Chin, W.P. West, *Microstructures of diamond formed by plasma-assisted chemical vapour deposition*, Journal of Materials Research, **5**, 1480−1489 (1990)

[112] D. Meakin, J. Stoemenos, P. Miliorato, N.A. Economou, *Structural studies of low-temperature low-pressure chemical deposited polycrystalline silicon*, Journal of Applied Physics, **61**, 5031−5037 (1987)

[113] V.V. Danilenko, *On the history of the discovery of nanodiamond synthesis*, Physics of the Solid State, **44**, 595−599 (2004)

[114] E. Ôsawa, in: D. Gruen, A.Y. Vul', O. Shenderova (Eds.), *Synthesis, Properties and Applications of Ultrananocrystalline Diamond*, Proceedings of the NATO Advanced Research Workshop on Ultrananocrystalline Diamond, June 7-10, 2004, St. Petersburg, Russia, NATO Science Series, Series II: Mathematics, Physics and Chemistry, vol. 192, Springer, Dordrecht, 2005, p. 231, (2004)

[115] O.A. Williams, M. Nesladek,M. Daenen, S. Michaelson, A. Hoffman, E. Ôsawa, K. Haenen, R.B. Jackman, *Growth, electronic properties and applications of nanodiamond*, Diamond and Related Materials, **17**, 1080−1088 (2008)

[116] N.V. Sirotinkin, A.P. Voznyakovskii, N.A. Ershova, *Model of formation of three-dimensional polyurethane films modified by detonation nanodiamond*, Physics Solid State, **46**, 746−747 (2004)

[117] J.L. Davidson, D.T. Bradshaw, U.S. Patent 6858157B2 (2005)

[118] V.E. Red'kin, *Lubricants with ultradisperse diamond-graphite powder*, Chemistry and Technology of Fuels and Oils, **40**, 164−170 (2004)

[119] V.Y. Dolmatov, *Detonation synthesis ultradispersed diamonds: properties and applications*, Russian Chemical Reviews, **70**, 607−626 (2001)

[120] S.J. Yu, M.W. Kang, H.C. Chang, M.K. Chen, C.Y. Yu, *Bright fluorescent nanodiamonds: No photobleaching and low cytotoxicity*, Journal of the American Chemical Society, **127**, 17604−17605 (2005)

[121] E. Ôsawa, *Recent progress and perspectives in single-digit nanodiamond*, Diamond and Related Materials, **16**, 2018−2022 (2007)

[122] T.M. Gubarevich, R.R. Sataev, V.Y. Dolmatov, *Chemical purification of ultradisperse diamonds*, 5th All-Union Meeting on Detonation, Krasnoyarsk USSR, Aug 5-15, p. 135−139 (1991)

[123] A.S. Chiganov, *Selective inhibition of the oxidation of nanodiamonds for their cleaning*, Physics Solid State **46**, 620−621 (2004)

[124] L. Li, J.L. Davidson, C.M. Lukehart, *Surface functionalization of nanodiamond particles via atom transfer radical polymerization*, Carbon, **44**, 2308−2315 (2006)

[125] S. Osswald, G. Yushin, V. Mochalin, S.O. Kucheyev, Y. Gogotsi, *Control of* sp^2/sp^3 *Carbon Ratio and Surface Chemistry of Nanodiamond Powders by Selective Oxidation in Air*, Journal of the American Chemical Society, **128**, 11635−11642 (2006)

[126] A.E. Aleksenskii, M.V. Baidakova, A.Y. Vul, V.I. Siklitskii, *Fullerenes and atomic clusters*, Physics Solid State **41**, 668−671 (1999)

[127] A. Krüger, F. Kataoka, M. Ozawa, T. Fujino, Y. Suzuki, A.E. Aleksenskii, A.Y. Vul', E. Ôsawa, *Unusually tight aggregation in detonation nanodiamond: Identification and disintegration*, Carbon, **43** 1722−1730 (2005)

[128] M. Ozawa, M. Inaguma, M. Takahashi, F. Kataoka, A. Krüger, E. Ôsawa, *Preparation and Behavior of Brownish, Clear Nanodiamond Colloids*, Advanced Materials **19**, 1201−1206 (2007)

[129] S. Ji, T. Jiang, K. Xu, S. Li, *FTIR study of the adsorption of water on ultradispersed diamond powder surface*, Applied Surface Science, **133**, 231−238 (1998)

[130] T. Jiang, K. Xu, *FTIR Study of ultradispersed diamond powder synthesized by explosive detonation*, Carbon, **33**, 1663−1671 (1995)

[131] L. La Torre Riveros, D.A. Tryk, C.R. Cabrera, *Chemical purification and characterization of diamond nanoparticles for electrophoretically coated electrodes*, Reviews on Advanced Materials Science, **10**, 256−260 (2005)

[132] N.B. Colthup, L.H. Daly, S.E. Wiberley, *Introduction to infrared and Raman spectroscopy*, Academic Press Inc. (1964)

[133] E. Mironova, A. Koretza, E. Petrovc, *Detonation synthesis ultradispersed diamond structural properties investigation by infrared absorption*, Diamond and Related Materials, **11**, 872−876 (2002)

[134] I. Larionova, V. Kuznetsov, A. Frolov, O. Shenderova, S. Moseenkov, I. Mazov, *Properties of individual fractions of detonation nanodiamond*, Diamond and Related Materials, **15**, 1804−1808 (2006)

[135] K. Xu, Q. Xue, *Deaggregation of ultradispersed diamond from explosive detonation by a graphitizationoxidation method and by hydroiodic acid treatment*, Diamond and Related Materials, **16**, 277−282 (2007)

[136] A.M. Schrand, L. Dai, J.J. Schlager, S.M. Hussain, E. Ôsawa, *Differential biocompatibility of carbon nanotubes and nanodiamonds*, Diamond and Related Materials, **16**, 2118−2123 (2007)

[137] O.A. Williams, O. Douheret, M. Daenen, K. Haenen, E. Ôsawa, M. Takahashi, *Enhanced diamond nucleation on monodispersed nanocrystalline diamond*, Chemical Physics Letters, **445**, 255−258 (2007)

[138] D.N. Belton, S. Schmeig, *States of surface carbon during diamond growth on Pt*, Surface Science, **233**, 131−140 (1990)

[139] W.R.L. Lambrecht, C.H. Lee, B. Segall, J.C. Angus, Z. Li, M. Sunkara, *Diamond nucleation by hydrogenation of the edges of graphitic precursors*, Nature, **364** 607−610 (1993)

[140] S.P. Mehandru, A.B. Anderson, J.C. Angus, *Hydrogenation of the (1010) graphite edge. Structural considerations from band calculations*, The Journal of Physical Chemistry, **96**, 10978−10982 (1992)

[141] Z. Li, L. Wang, T. Suzuki, A. Argoitia, P. Pirouz, J.C. Angus, *Orientation relationship between chemical vapour deposited diamond and graphite substrates*, Journal of Applied Physics, **73**, 711−715 (1993)

[142] N.I. Kurihara, K. Hirabayashi, K. Suzuki, M. Ichihara, A. Takeuchi, *Epitaxial growth of graphite layer on 111 surface of vapor-deposited diamond*, Journal of Applied Physics, **69**, 6360−6363 (1991)

[143] T. Suzuki, M. Yagi, K. Shibuki, M. Hasemi, *Oriented diamond on graphite flakes*, Applied Physics Letters, **65**, 540−542 (1994)

[144] J.J. Dubray, C.G. Pantano, W.A. Yarbrough, *Graphite as a substrate for diamond growth,* Journal of Applied Physics **72**, 3136−3142 (1992)

[145] M.B. Moran, K.A. Klemm, L.F. Johnson, *Diamond film deposition on graphite*, US Patent 5654044 (1997)

[146] Z. Feng, K. Komvopoulos, I.G. Brown, D.B. Bogy, *Effect of graphitic carbon films on diamond nucleation by microwave-plasma-enhanced chemical-vapor deposition*, Journal of Applied Physics, **74**, 2841−2849 (1993)

[147] R. Beckmann, B. Sobisch, W. Kulisch, *Gas phase investigations during diamond deposition with HFCVD and MW-PECVD*, Proceedings of the 3rd International Symposium on Diamond Materials, Electrochemical Society Proceedings, ECS, Pennington, NJ, 1026−1031 (1993)

[148] T. Frauenheim, G. Jungnickel, P. Sitch, M. Kaukonen, F. Weich, J. Widany, D. Porezag, *A molecular dynamics study of N-incorporation into carbon systems: doping, diamond growth and nitride formation*, Diamond and Related Materials, **7**, 348−355 (1998)

[149] F.K. de Theije, J.J. Scermer, W.J.P. van Enckevort, *Effects of nitrogen impurities on the CVD growth of diamond: step bunching in theory and experiment*, Diamond and Related Materials, **9**, 1439−1449 (2000)

[150] N. Shang, P. Papakonstantinou, P. Wang, A. Zakharov, U. Palnitkar, I. Lin, M. Chu, A. Stamboulis, *Self-assembled growth, microstructure and field-emission high-performance of ultrathin diamond nanorods*, ACS Nano, **3**, 1032−1038 (2009)

[151] P.E. Pehrsson, F.G. Celii, J.E. Butler, *Chemical mechanisms of diamond CVD*, in Diamond Films and Coatings, development, properties, and applications, R.R. Davis (ed.), Noyes Publications, 68−146 (1993)

[152] A.F. Azevedo, J.T. Matxuxhima, F.C. Vicentin, M.R. Baldan, N.G. Ferreira, *Surface characterization of NCD films as a function of* sp^2/sp^3 *carbon and oxygen content*, Applied Surface Science, (in press) (2009)

[153] L.C. Nistor, J. Van Landuyt, V.G. Ralchenko, E.D. Obraztsova, A.A. Smolin, *Nanocrystalline diamond films transmission electron microscopy and Raman spectroscopy characterization*, Diamond and Related Materials, **6**, 159−168 (1997)

[154] Y.K. Liu, Y. Tzeng, P.L. Tso, I.N. Lin, *Nanocrystalline diamond films deposited by microwave plasma CVD in mixtures of argon and methane with and without hydrogen additive*, Proceedings of the seventh Applied Diamond Conference, Third Frontier Carbon Technology Joint Conference, M. Murakawa, M. Miyoshi, Y. Koga, L. Schafer, Y. Tzeng (Ed.) 547−552 (2003)

[155] M. Miyake, A. Ogino, M. Nagatsu, *Characteristics of nano-crystalline diamond films prepared in* $Ar/H_2/CH_4$ *microwave plasma*, Thin Solid Films, **515**, 4258−4261 (2007)

[156] W.A. Yarbrough, R. Messier, *Current issues and problems in the chemical vapor deposition of diamond*, Science,**247**, 688−696 (1990)

[157] R.J. Nemanich, J.T. Glass, G. Lucovsky, R.E. Shroder, *Raman scattering characterization of carbon bonding in diamond and diamondlike thin films*, Journal of Vacuum Science and Technology A, **6**, 1783−1787 (1988)

[158] A.C. Ferrari, J. Robertson, *Raman spectroscopy of amorphous, nanostructured, diamond-like carbon, and nanodiamond*, Philosophical Transactions of the Royal Society London A, **362**, 2477−2512 (2004)

[159] T. Xu, S. Yang, J. Lu, Q. Xue, J. Li, W. Guo, Y. Sun, *Characterization of nanocrystalline diamond films implanted with nitrogen ions*, Diamond and Related Materials, **10**, 1441−1447 (2001)

[160] J.I.B. Wilson, J.S. Walton, G. Beamson, *Analysis of chemical vapour deposited diamond films by X-ray photoelectron spectroscopy*, Journal of Electron Spectroscopy and Related Phenomena, **121**, 183−201 (2001)

[161] C. Popov, W. Kulisch, S. Boycheva, K. Yamamoto, G. Ceccone, Y. Koga, *Structural investigation of nanocrystalline diamond/amorphous carbon composite films*, Diamond and Related Materials, **13**, 2071−2075 (2004)

[162] National Institute of Standards and Technology Atomic Spectra Database, http://physics.nist.gov/PhysRefData/ASD/index.html, (2009)

[163] S.K. Sharma, H.K. Mao, P.M. Bell, J.Z. Xu, *Measurement of stress in diamond anvils with micro-Raman spectroscopy*, Journal of Raman Spectroscopy, **16**, 350−352 (1985)

[164] J.K. Shin, C.S. Lee, K.R. Lee, K.Y. Eun, *Effect of residual stress on the Raman-spectrum analysis of tetrahedral amorphous carbon films*, Applied Physics Letters, **78**, 631−633 (2001)

[165] A.F. Azevedo, S.C. Ramos, M.R. Baldan, N.G. Ferreira, *Graphitization effects of CH_4 addition on NCD growth by first and second order Raman spectra and by X-ray diffraction measurements*, Diamond and Related Materials, **17**, 1337−1142 (2008)

[166] A. Heiman, E. Lakin, E. Zolotoyabko, A. Hoffman, *Microstructure and stress in nano-crystalline diamond films deposited by DC glow discharge CVD*, Diamond and Related Materials **11**, 601−607 (2002)

[167] P. John, J.R. Rabeau, J.I.B. Wilson, *The cavity ring-down spectroscopy of C_2 in a microwave plasma*, Diamond and Related Materials, **11**, 608−611 (2002)

[168] P.K. Bachmann, D. Leers, H. Lydtina, *Towards a general concept of diamond chemical vapour deposition*, Diamond and Related Materials, **1**, 1−12 (1991)

[169] P.K. Bachmann, H.J. Hagemann, H. Lade, D. Leers, F. Picht, D.U. Wiechert, H. Wilson, *Diamond chemical vapor deposition: gas compositions and film properties*, in Diamond, SiC, and Nitride wide Band Gap Semiconductors, edited by C.H. Carter, G. Gidenblatt, S. Nakamura, R.J. Nemanich Materials Research Society symposium proceedings, Materials Research Society, Pittsburgh, PA, **339**, 267−277 (1994)

[170] D. Zhou, T.G. McCauley, L.C. Qin, A.R. Krauss, D.M. Gruen, *Synthesis of nanocrystalline diamond thin films from an Ar−CH4 microwave plasma*, Journal of Applied Physics **83**, 540−543 (1998)

[171] Q. Chen, D.M. Gruen, A.R. Krauss, T.D. Corrigan, M. Witek, G.M. Swain, *The structure and electrochemical behavior of nitrogen-containing nanocrystalline diamond films deposited from $CH_4/N_2/Ar$ mixtures*, Journal of The Electrochemical Society, **148**, E44−E51 (2001)

[172] D.N. Belton, S.J. Schmieg, *Effects of oxygen on diamond growth using platinum substrates*, Journal of Applied Physics **69**, 3032−3036 (1991)

[173] K. Kobashi, K. Nishimura, Y. Kawate, T. Horiuchi, *Synthesis of diamonds by use of microwave plasma chemical-vapour deposition: Morphology and growth of diamond films*, Physical Review B, **38**, 4067−4084 (1988)

[174] K. Kobashi, K. Nishimura, Y. Kawate, T. Horiuchi, *Morphology and growth of diamond films*, The Journal of Vacuum Science and Technology A, **6**, 1816−1817 (1988)

[175] O. Brinza, J. Achard, F. Silva, X. Bonnin, P. Barroy, K. De Corte, A. Gicquel, *Dependence of CVD diamond growth rate on substrate orientation as a function of process parameters in the high mocrowave power density regime*, Physica Statu solidi (a), **205**, 2114−2120 (2008)

[176] D.S. Knight, W.B. White, *Characterization of diamond films by Raman spectroscopy*, Journal of Materials Research, **4**, 385−393 (1985)

[177] D.M. McNamara, K.K. Gleason, J. Butler, D.J. Vestyck, *Evaluation of diamond films by NMR and Raman spectroscopy*, Diamond and Related Materials, **19**, 1145−1155 (1992)

[178] B.V. Spitsyn, L.L. Bouilov, B.V. Derjagin, *Vapor growth of diamond on diamond and other surfaces*, Journal of Crystal Growth, **52**, 219−226 (1981)

[179] C.J. Chu, R.H. Hauge, J.L. Margrave, M.P. D'Evelyn, *Growth kinetics of (100), (110) and (111) homoepitaxial diamond films*, Applied Physics Letters, **61**, 1393−1395 (1992)

[180] A.L. Vikharev, A.M. Gorbachev, A.V. Kozlov, D.B. Radishev, A.B. Muchnikov, *Microcrystalline diamond growth in presence of argon in millimeter-wave plasma-assisted CVD reactor*, Diamond and Related Materials, **17**, 1055−1061 (2008)

[181] A. Inspektor, T. McKenna, Y. Liou, L. Bourget, K.E. Spear, R. Messier, *Plasma Chemistry in Diamond Deposition*, Proceedings of the First International Symposium of Diamond and Diamond-Like Films, Electrochemical Society, 342−345 (1989)

[182] W. Zhu, A.R. Badzian, R. Messier, *Morphological Phenomena of CVD Diamond (Part I)*, Proceedings of SPIE on Diamond Optics III, **1325**, 187−201 (1990)

[183] C. Wild, N. Herres, R. Locher, W. Mulller-Sebert, P. Koidal, *Control of twin formation: a prerequisite for the growth of thick oriented diamond films* in S. Satio, N. Fujimori, O. Fukuna, M. Kamo, K. Kobashi, M. Yoshikawa (eds) Advances in New Diamond Science and Technology, MYO, Tokyo, 149−152 (1994)

[184] Z.L. Wang, J. Bentley, R.E. Clausing, L. Heatherly, L.L. Horton, *Direct correlation of microtwin distribution with growth face morphology of CVD diamond films by a novel TEM technique*, Journal of Materials Research, **9**, 1552−1565 (1994)

[185] L.F. Sutcu, C.J. Chu, M.S. Thompson, R.H. Hauge, J.L. Margrave, M.P. D'Evelyn, *Atomic force microscopy of (100), (110), (111) homoepitaxial diamond films*, Journal of Applied Physics, **71**, 5930−5940 (1992)

[186] A.M. Stoneham, J.R. Matthews, I.J. Ford, *Innovative materials for fusion power plant structures: separating functions*, Journal of Physics: Condensed Matter, **16** S2597−S2621 (2004)

[187] S.K. Erents, C.M. Braganza, G.M. McCracken, *Methane formation during the interaction of energetic protons and deuterons with carbon*, Journal of Nuclear Materials, **63**, 399−404 (1976)

[188] J. Roth, J. Bohdansky, W. Poschenrieder, M.K. Sinha, *Physical and chemical sputtering of graphite and SiC by hydrogen and helium in the energy range of 600 to 7500 eV*, Journal of Nuclear Materials, **63**, 222−229 (1976)

[189] J. Roth, C. Garcia-Rosales, *Analytic description of the chemical erosion of graphite by hydrogen ions*, Nuclear Fusion, **36**, 1647−1659 (1996)

[190] C. Hopf, A. von Keudell, W. Jacob, *Chemical sputtering of hydrocarbon films*, Journal of Applied Physics, **94**, 2373−2380 (2003)

[191] J. Küppers, *The hydrogen surface chemistry of carbon as a plasma facing material*, Surface Science Reports, **22**, 249−321 (1995)

[192] M. Schlüter, C. Hopf, T. Schwarz-Selinger, W. Jacob, *Temperature dependence of the chemical sputtering of amorphous hydrogenated carbon films by hydrogen*, Journal of Nuclear Materials, **376**, 33−37 (2008)

[193] Y. Takeguchi, M. Kyo, Y. Uesugi, Y. Tanaka, S. Masuzaki, *Study of carbon dust formation and their structure using inductively coupled plasmas under high atomic hydrogen irradiation*, Journal of Nuclear Materials, **390391**, 188−191 (2009)

[194] Y. Yamazaki, K. Ishikawa, N. Mizuochi, S. Yamasaki, *Structural change in diamond by hydrogen plasma treatment at room temperature*, Diamond and Related Materials **14**, 1939−1942 (2005)

[195] S. Porro, G. De Temmerman, P. John, S. Lisgo, I. Villalpando, J.I.B. Wilson, *Effects in CVD diamond exposed to fusion plasmas*, Physics Status Solidi (a), **206**, 2028-2032 (2009)

[196] J.E. Butler, R.L. Woodin, *Thin film diamond growth mechanisms (and comment)*, Philosophical Transactions of the Royal Society London A, **342**, 209−224 (1993)

[197] R.E. Rawles, S.F. Komarov, R. Gat, W.G. Morris, J.B. Hudson, M.P. D'Evelyn, *Mechanism of surface smoothing of diamond by hydrogen plasma*, Diamond and Related Materials, **6**, 791−795 (1997)

[198] K. Hayashi, S. Yamanaka, H. Okushi, K. Kajimura, *Stepped growth and etching of (001) diamond*, Diamond and Related Materials, **5**, 1002−1005 (1996)

[199] L.J. Giling, W.J.P. Van Enckevort, *On the influence of surface reconstruction on crystal growth processes*, Surface Science, **161**, 567−583 (1985)

[200] C.L. Cheng, H.C. Chang, J.C. Lin, K.J. Song, J.K. Wang, *Direct observation of hydrogen etching anisotropy on diamond single crystal surface*, Physical Review Lettters, **78**, 3713−3716 (1997)

[201] B.D. Thoms, M.S. Owens, J.E. Butler, C. Spiro, *Production and characterization of smooth, hydrogen-terminated diamond C(100)*, Applied Physics Letters, **65**, 2957−2959 (1994)

[202] C.M. Donnelly, R.W. McCullough, J. Geddes, *Etching of graphite and diamond by thermal energy hydrogen atoms*, Diamond and Related Materials, **6**, 787−790 (1997)

[203] T. Schwarz-Selinger, M. Meier, C. Hopf, A. von Keudell, W. Jacob, *Can plasma experiments unravel microscopic surface processes in thin film growth and erosion? Implications of particlebeam experiments on the understanding of a-C:H growth*, Vacuum, **71**, 361−376 (2003)

[204] D.G. Whyte, G.R. Tynana, R.P. Doernera, J.N. Brooks, *Investigation of carbon chemical erosion with increasing plasma flux and density*, Nuclear Fusion, **41**, 47−62 (2001)

[205] J.P. Briand, A. Anders, O. Monteiro, R. Phaneuf, Z. Xie, J. Achard, M. Benhachoum, S. Terracol, *Surface transformation of graphite or diamond following Highly Charged Ion irradiation*, Nuclear Instruments and Methods in Physics Research B, **267**, 678−682 (2009)

[206] M. Schlüter, C. Hopf, W. Jacob, *Chemical sputtering of carbon by combined exposure to nitrogen ions and atomic hydrogen*, New Journal of Physics, **10**, 053037 (2008)

[207] C. Hopf, M. Schl"uter, T. Schwarz-Selinger, U von Toussaint, W. Jaco, *Chemical sputtering of carbon films by simultaneous irradiation with argon ions and molecular oxygen*, New Journal of Physics **10**, 093022 (2008)

[208] W.D. Man, J.H. Wang, C.X. Wang, S.G. Wang, L.W. Xiong, *Planarizing CVD diamond films by using hydrogen plasma etching enhanced carbon diffusion process*, Diamond and Related Materials, **16**, 1455−1458 (2007)

[209] S. Porro, G. De Temmerman, S. Lisgo, P. John, I. Villalpando, J.W. Zimmer, B. Johnson, J.I.B. Wilson, *Nanocrystalline diamond coating of fusion plasma facing components*, Diamond and Related Materials, **18**, 740−744 (2009)

[210] H. Shiomi, K. Tanabe, Y. Nishibayashi, N. Fujimori, *Epitaxial growth of high quality diamond film by the microwave plasma-assisted chemical vapor-deposition method*, Japanise Journal of Applied Physics, **29**, 34−40 (1990)

[211] K. Hayashi, S. Yamanaka, H. Okushi, K. Kajimura, *Homoepitaxial diamond films with large terraces*, Applied Physics Letters, **68**, 1220−1222 (1996)

[212] A. van der Drift, *Evolutionary selection, a principle governing growth orientation in vapour-deposited layers*, Philips Research Reports, **22**, 267−288 (1967)

[213] N. Lee, A. Badzian, *A study on surface morphologies of (001) homoepitaxial diamond films*, Diamond and Related Materials, **6**, 130−145 (1997)

[214] W.J.P. van Enckevort, G. Janssen, W. Vollenberg, J.J. Schermer, L.J. Gilling, M. Seal, *CVD diamond growth mechanisms as identified by surface topography*, Diamond and Related Materials, **2**, 997−1033 (1993)

[215] W.J.P. van Enckevort, G. Janssen, J.J. Schermer, L.J. Giling, *Step-related growth phenomena on exact and misoriented {001} surfaces of CVD-grown single-crystal diamonds*, Diamond and Related Materials, **4**, 250−255 (1995)

[216] N. Lee, A. Badzian, *Effect of misorientation angles on the surface morphologies of (001) homoepitaxial diamond thin films*, Applied Physics Letters, **66**, 2203−2205 (1995)

[217] B. Koslowski, S. Sotrobel, M.J. Wenig, R. Martschat, P. Ziemann, *On the roughness of hydrogen-plasma treated diamond (100) surfaces*, Diamond and Related Materials, **7**, 322−326 (1998)

[218] S.G. Ri, H. Watanabe, M. Ogura, D. Takeuchi, S. Yamasaki, H. Okushi, *Hydrogen plasma etching mechanism on (001) diamond*, Journal of Crystal Growth, **293**, 311−317 (2006)

[219] C.A. Zorman, G.T. Mearini, R.W. Hoffman, *An in situ heating study of hydrogen-containing adsorbates on polycrystalline diamond surfaces using elastic recoil detection*, Diamond and Related Materials, **9**, 1518−1523 (2000)

[220] M. Yamamoto, T. Teraji, T. Ito, *Improvement in the crystalline quality of homoepitaxial diamond films by oxygen plasma etching of mirror-polished diamond substrates*, Journal of Crystal Growth, **285**, 130−136 (2005)

[221] N.M. Rodriguez, A. Chambers, R. Terry, K. Baker, *Catalytic Engineering of Carbon Nanostructures*, Langmuir, **11**, 3862−3866 (1995)

[222] C. van Gulijk, K.M. de Lathouder, R. Haswell, *Characterizing herring bone structures in carbon nanofibers using selected area electron diffraction and dark field transmission electron microscopy*, Carbon, **44**, 2950−2956 (2006)

[223] Y.A. Kim, T. Hayashi, S. Naokawa, T. Yanagisawa, M. Endo, *Comparative study of herringbone and stacked-cup carbon nanofibers*, Carbon, **43**, 3005−3008 (2005)

[224] J. Vera-Agullo, H. Varela-Rizo, J.A. Conesa, C. Almansa, C. Merino, I. Martin-Gullon, *Evidence for growth mechanism and helixspiral cone structure of stacked-cup carbon nanofibers*, Carbon, **45**, 2751−2758 (2007)

[225] B. Eksioglu, A. Nadarajah, *Structural analysis of conical carbon nanofibers*, Carbon, **44**, 360−373 (2006)

[226] M. Weisenberger, I. Martin-Gullon, J. Vera-Agullo, H. Varela-Rizo, C. Merino, R. Andrews, D. Qian, T. Rantell, *The effect of graphitization temperature on the structure of helical-ribbon carbon nanofibers*, Carbon, **47**, 2211−2218 (2009)

[227] E.C. Almeida, A.V. Diniz, V.J. Trava-Airoldi, N.G. Ferreira, *Electrochemical characterization of doped diamond-coated carbon fibers at different boron concentrations*, Thin Solid Films, **485**, 241−246 (2005)

[228] W. Xia, J.H. Bitter, D. Su, J. Qian, M. Muhler, *Iron impregnation on the amorphous shell of vapor grown carbon fibers and the catalytic growth of secondary nanofibers*, Diamond and Related Materials, **18**, 13−19 (2009)

[229] R.T.K. Baker, *Catalytic growth of carbon filaments*, Carbon, **27**, 315−323 (1989)

[230] M. Endo, K. Takeuchi, S. Igarashi, K. Kobori, M. Shiraishi, H.W. Kroto, *The production and structure of pyrolytic carbon nanotubes (PCNTs)*, Journal of Physics and Chemistry of Solids, **54**, 1841−1848 (1993)

[231] A. Chambers, C. Park, R. Terry, K. Baker, N.M. Rodriguez, *Hydrogen Storage in Graphite Nanofibers*, The Journal of Physical Chemistry B, **102**, 4253−4256 (1998)

[232] A. Oberlin, M. Endo, T. Koyama, *Filamentous growth of carbon through benzene decomposition*, Journal of Crystel Growth, **32**, 335−349 (1976)

[233] S. Mori, M. Suzuki, *Effect of oxygen and hydrogen addition on the low-temperature synthesis of carbon nanofibers using a low-temperature CO/Ar DC plasma*, Diamond and Related Materials, **17**, 999−1002 (2008)

[234] P. Gadelle, in Carbon Fibers Filaments and Composites (J. L. Figueiredo, C. A. Bernardo, and R. T. K. Baker, Eds.), Kluwer Academic, Dordrecht/Norwell, MA, p. 95, 1990.

[235] F. Benissad, P. Gadelle, M. Coulon, L. Bonnetain, *Formation de fibres de carbone a partir du mehane: I Croissance catalytique et epaississement pyrolytique*, Carbon, **26**, 61−69 (1988)

[236] G.G. Tibbets, M.G. Devour, E.J. Rodda, *An adsorption-diffusion isotherm and its application to the growth of carbon filaments on iron catalyst particles*, Carbon, **25**, 367−375 (1987)

[237] S.S. Tzeng, K.H. Hung, T.H. Ko, *Growth of carbon nanofibers on activated carbon fiber fabrics*, Carbon, **44**, 859−865 (2006)

[238] B. Louis, R. Vieira, A. Carvalho, J. Amadou, M.J. Ledoux, C. Pham-Huu, *Carbon nanofibers grown over graphite supported Ni catalyst: relationship between octopus-like growth mechanism and macro-shaping*, Topics in Catalysis, **45**, 75−80 (2007)

[239] W.X. Lu, Z.J. Sui, J.H. Zhou, P. Li, D. Chen, X.G. Zhou, *Kinetically controlled synthesis of carbon nanofibers with different morphologies by catalytic CO disproportionation over iron catalyst*, Chemical Engineering Science, **65**, 193−200(2010)

[240] M.A. Ermakova, D.Y. Ermakov, A.L. Chuvilin, G.G. Kuvshinov, *Decomposition of methane over iron catalysts at the range of moderate temperatures: the influence of structure of the catalytic systems and the reaction conditions on the yield of carbon and morphology of carbon filaments*, Journal of Catalysis, **201**, 183−197 (2001)

[241] G.G. Tibbetts, G.L. Doll, D.W. Gorkiewicz, J.J. Moleski, T.A. Perry, C.J. Dasch, M.J. Balogh, *Physical properties of vapor-grown carbon fibers*, Carbon, **31**, 1039−1047 (1993)

[242] Y.Y. Fan, F. Li, H.M. Cheng, G. Su, Y.D. Yu, Z.H. Shen, *Preparation, morphology, and microstructure of diameter-controllable vapor-grown carbon nanofibers*, Journal of Materials Research, **13**, 2342−2346 (1998)

[243] J.I. Paredes, A. Martinez-Alonso, J.M.D. Tascon, *Surface characterization of submicron vapor grown carbon fibers by scanning tunneling microscopy*, Carbon, **39**, 1575−1587 (2001)

[244] J.H. Bitter, M.K. van der Lee, A.G.T. Slotboom, A.J. van Dillen, K.P. de Jong, *Synthesis of highly loaded highly dispersed nickel on carbon nanofibers by homogeneous deposition−precipitation*, Catalysis Letters, **12**, 139−142 (2003)

[245] H.C. Foley, *Carbogenic molecular sieves: synthesis, properties and applications*, Microporous Materials, **4**, 407−433 (1995)

[246] F. Rodriguez-Reinoso, *The role of carbon materials in heterogeneous catalysis*, Carbon, **36**, 159−175 (1998)

[247] C.A. Bessel, K. Laubernds, N.M. Rodriguez, R. Terry, K. Baker, *Graphite Nanofibers as an Electrode for Fuel Cell Applications*, The Journal of Physical Chemistry B, **105**, 1115−1118 (2001)

[248] G.A. Kovalenko, E.V. Kuznetsova, Y.I. Mogilnykh, I.S. Andreeva, D.G. Kuvshinov, N.A. Rudina, *Catalytic filamentous carbons for immobilization of biologically active substances and non-growing bacterial cells*, Carbon, **39**, 1033−1043(2001)

[249] H. Suda, K. Haraya, *Gas permeation through micropores of carbon molecular sieve membranes derived from kapton polyimide*, The Journal of Physical Chemistry B, **101**, 3988−3994 (1997)

[250] B.T. Hang, M. Eashira, I. Watanabe, S. Okada, J.I. Yamaki, S.H. Yoon, I. Mochida, *The effect of carbon species on the properties of Fe/C composite for metalair battery anode*, Journal of Power Sources, **143**, 256−264 (2005)

[251] G.G. Tibbetts, M.L. Lake, K.L. Strong, B.P. Rice, *A review of the fabrication and properties of vapor-grown carbon nanofiber/polymer composites*, Composites Science and Technology, **67**, 1709−1718 (2007)

[252] S. Flandrois, B. Simon, *Carbon materials for lithium-ion rechargeable batteries*, Carbon, **37**, 165−180 (1999)

[253] E. Ochoa-Fernandez, D. Chen, Z. Yu, B. Totdal, M. Ronning, A. Holmen, *Effect of carbon nanofibers-induced microstrain on the catalytic activity of Ni crystals*, Surface Science, **554**, L107−L112(2004)

[254] E. Boellaard, P.K. de Bokx, A.J.H.M. Kock, J.W. Geus, *The formation of filamentous carbon on iron and nickel catalysts*, Journal of Catalysis, **96**, 481−490 (1985)

[255] K. Heinemann, H. Poppa, *Selected-zone dark field electron microscopy*, Applied Physics Letters, **20**, 122−125 (1972)

[256] W.C. Hinds, Aerosol technology, New York, John Wiley and Sons, 182−205 (1999)

[257] S.R. Mukai, T. Masuda, T. Harada, K. Hashimoto, *Rapid production of silicon-containing vapor grown carbon fibers using the liquid pulse injection technique*, Carbon, **38**, 1801−1805(2000)

[258] E.C. Almeida, M.R. Baldan, J.M. Rosolen, N.G. Ferreira, *Impedance characteristics of the diamond/carbon fiber electrodes for electrical double-layer capacitor*, Diamond and Related Materials, **17**, 1529−1533 (2008)

[259] R.B. Mathur, S. Chatterjee, B.P. Singh, *Growth of carbon nanotubes on carbon fibre substrates to produce hybrid/phenolic composites with improved mechanical properties*, Composites Science and Technology, **68**, 1608−1615 (2008)

[260] Y. Hayashi, K. Suzuki, B. Jang, T. Tokunaga, H. Matsumoto, M. Tanemura, A. Tanioka, G.A.J. Amaratunga, *Synthesis and characterization of carbon nanotube grown on flexible and conducting carbon fiber sheet for field emitter*, Diamond and Related Materials, **18**, 341−344 (2009)

[261] Z. Zhao, J. Gou, A. Khan, *Processing and structure of carbon nanofiber paper*, Journal of Nanomaterials, **2009**, Article ID 325769, 7 pages (2009)

[262] C. Bower, O. Zhou, W. Zhu. D.J. Werder, S. Jin, *Nucleation and growth of carbon nanotubes by microwave plasma chemical vapor deposition*, Applied Physics Letters, **77**, 2767−2769 (2000)

[263] S.D. Gardner, C.S.K. Singamsetty, G.L. Booth, G.R. He, *Surface characterization of carbon fibers using angle-resolved XPS and ISS*, Carbon, **33**, 587−595 (1995)

[264] S.N. Chaudhuri, R.A. Chaudhuri, R.E. Benner, M.S. Penugonda, *Raman spectroscopy for characterization of interfacial debonds between carbon fibers and polymer matrices*, Composite Structures, **76**, 375−387 (2006)

[265] L. Hui-Feng, S. Dimitrijev, D. Sweatman, H.B. Harrison, P. Tanner, *Distribution and chemical bonding of N at NO nitrided SiC/SiO_2 interface*, Proceedings of Conference on Optoelectronic and Microelectronic Materials Devices, 164−166 (1998)

[266] National Institute of Standards and Technology X-ray Photoelectron Spectroscopy Database, http://srdata.nist.gov/xps/, (2009)